Spring 1-1-2013

Influence of Long Duration Ground Shaking on Collapse of Reinforced Concrete Structures

Meera Raghunandan
University of Colorado at Boulder, meera.r.nandan@gmail.com

INFLUENCE OF LONG DURATION GROUND SHAKING ON COLLAPSE OF REINFORCED CONCRETE STRUCTURES

by

MEERA RAGHUNANDAN

B.Tech, National Institute of Technology, Calicut, India, 2006

M.S., University of Colorado at Boulder, 2012

A thesis submitted to the

Faculty of the Graduate School of the

University of Colorado in partial fulfillment

of the requirement for the degree of

Doctor of Philosophy

Department of Civil, Environmental and Architectural Engineering

2013

This thesis entitled:
Influence of Long Duration Ground Shaking on Collapse of Reinforced Concrete Structures
written by Meera Raghunandan
has been approved for the Department of Civil, Environmental and Architectural Engineering

Abbie Liel (Committee Chair)

Ross Corotis

Shideh Dashti

Date

The final copy of this thesis has been examined by the signatories, and we
Find that both the content and the form meet acceptable presentation standards
Of scholarly work in the above mentioned discipline.

Raghunandan, Meera (Ph.D., Civil Engineering)

Influence of Long Duration Ground Shaking on Collapse of Reinforced Concrete Structures

Thesis directed by Assistant Professor Abbie Liel

This thesis aims to assess the influence of long duration shaking during earthquakes on structural collapse. It is well accepted that ground motion intensity and its frequency content affects structural seismic response; however, the influence of duration of ground shaking on structural damage remains a topic of debate. According to past research, duration of ground motion is found to influence structural damage when damage measures based on cumulative energy are used, and when the damage measures are based on maximum response, duration is generally found to be insignificant.

In the first part of the thesis, building models are subjected to ground motions with varying duration in order to investigate the influence of duration on the intensity of ground motion at which collapse occurs. Results indicate that the ground motion characteristics of duration and structural characteristics of fundamental period and ductility capacity are significant predictors of structural collapse capacity. Long duration records are associated with larger number of cycles of loading and impart more energy to the structure. As a result, the probability of collapse for a structure is found to be higher on being subjected to long duration ground motion having same intensity as a short duration ground motions. Therefore, the study shows that it is important to consider the expected duration of ground motions at the site for seismic design of structures in addition to ground motion's intensity and frequency, which are already explicitly accounted for in building codes.

In the second part of the thesis, the collapse capacity of structures is assessed for seismic events in which the structure is subjected to long duration shaking: (1) subduction earthquakes and (2) mainshock-aftershock earthquake sequences. Ground motions from subduction zone earthquakes are characterized by long duration of shaking and a have distinct frequency content. The study of subduction earthquakes focuses on the imminent danger of large magnitude subduction earthquake in the Cascadia subduction zone, which lies off the coast of the Pacific Northwest region of the U.S In order to assess the influence of subduction ground motions on collapse of reinforced concrete buildings, nonlinear dynamic analysis utilizing crustal and subduction ground motions is carried out on a portfolio of buildings in the cities of Seattle and Portland. The results indicate significantly higher collapse risk of buildings on being subjected to long duration subduction earthquake shaking as compared to crustal earthquakes. This higher risk affects all structures analyses, although the impacts are more significant for more ductile structures.

Structures that are exposed to mainshock-aftershock sequences also experience longer duration shaking as compared to an individual mainshock event. It is important to understand the aftershock fragility of the buildings because of the possibility of further damage in aftershock for a building already damaged in mainshock. This thesis assessed the aftershock damage and collapse risk of mainshock damaged modern reinforced concrete buildings in California. The study shows that low to moderate levels of mainshock damage do not significantly alter a building's capacity to withstand subsequent shaking, but that more substantial damage during mainshock can significantly reduce its collapse resistance during aftershock. The findings also suggest that residual interstory and roof drifts are strong predictors of reduced ability to

withstand subsequent shaking and should remain a substantial part of post-earthquake visual safety assessments, like those described in ATC-20.

ACKNOWLEDGMENTS

There are several people I would like to thank for helping me through my Ph.D. and making it possible for me to defend my thesis successfully. I have really enjoyed this incredible journey over the last four and half years doing research, learning new things and meeting new people.

First and foremost, I would like to thank my Ph.D. adviser, Professor Abbie Liel, for providing me with an opportunity to work with her during my graduate studies at University of Colorado, Boulder. I couldn't have asked for a better mentor and guide for my Ph.D and I really appreciate all the support, guidance and motivation that she has provided me through my academic career.

I would like to thank my Ph.D. dissertation committee members, Professor Ross Corotis, Professor Shideh Dashti, Professor Keith Porter and Nicolas Luco for always supporting my research work and providing me with great feedback from time to time, helping me improve the quality of my work immensely.

I also had an opportunity to work with researchers outside University of Colorado Boulder and their insights and assistance during the course of my Ph.D. has helped me greatly. For my building aftershock vulnerability study, Hyeuk Ryu from Geoscience Australia provided me with his codes for SDOF models and discussed his methodology in detail with me. This helped me greatly in developing my codes for my MDOF models and implementing them on Janus supercomputer. I also got great feedback regarding my building models and analysis results from S.R. Uma at GNS Science for the aftershock vulnerability assessment project. I

would like to thank Stephen Harmsen from USGS for providing me with deaggregated hazard curves for crustal and subduction earthquakes for sites in Pacific Northwest. He graciously generated these curves specifically for my research work because they were not readily available at USGS website and I really appreciate his time and effort. I would like to thank Majid Baradaran Shoraka from University of British Columbia for sharing his code for triggering collapse and discussing the implementation and convergence issues of shear and axial models.

The aftershock vulnerability analysis utilized the Janus supercomputer, which is supported by the National Science Foundation (award number CNS-0821794), the University of Colorado Boulder, the University of Colorado Denver, and the National Center for Atmospheric Research. The Janus supercomputer is operated by the University of Colorado Boulder. The computationally intensive mainshock aftershock analyses would not have been possible without *OpenSeesMP* getting installed on Janus Supercomputer at University of Colorado Boulder. I would like to thank Frank McKenna, Tim and Monte for all their assistance in getting the software installed. I would also like to thank Department of Civil Environmental and Architectural Engineering for allowing me to use department allocation of research computation time on the supercomputer.

Graduate school and Ph.D. research became more fun because of my amazing officemates and friends Holly Bonstrom , Siamak Sattar , Jared Debock , Lan Nguyen, Karim Farokhnia, Cody Harrington, Sarah Welsh-Huggins, Yolanda Lin and Derek Kozak. In addition to all the fun, I really appreciate all the code debugging, practice presentation and research feedback sessions I had with each of you.

I want to thank all my incredible friends back in India and ones here in US (especially Anitha and Vineetha) who have stuck by me through thick and thin. Also, this graduate school experience would have been impossible without the support of my amazing parents Raghunandan and Latha back in India and my incredible sister Maya. Last but not least, I want to extend a big thanks to my fiancé and best friend Jay for always being there and always supporting me.

CONTENTS

TABLES

FIGURES

CHAPTER 1 INTRODUCTION

Earthquake ground motions can be characterized by their amplitude (or intensity), frequency content and duration. Although the influence duration of ground motion on seismically induced soil damage such as liquefaction and slope stabilities is widely accepted, the structural engineering community still has contradicting views on the role of ground motion duration in influencing seismically induced structural damage. Different studies conducted on this topic have employed different definitions of duration, building models, analysis procedures and measures for structural damage, leading to the variety of views on the topic. In general, it is found that studies that use cumulative damage based measures find duration to influence the structural response, while studies that measure damage using maximum structural response find no correlation between response and ground motion duration (Hancock and Bommer 2006). Currently, ground motion duration is not explicitly considered in current seismic design procedures (ASCE 2010). However, since buildings at sites exposed to larger magnitude events, may experience longer duration ground shaking, it has been argued that duration is implicitly accounted for in higher intensities for design earthquake at those sites.

The main objective of this thesis to understand the influence of long duration ground shaking on structural collapse. Long duration shaking can occur at sites far from epicenter for large magnitude crustal earthquakes, or in regions expecting subduction earthquakes, or sites where multiple sequences can occur within a short period of time (*e.g.* mainshock-aftershock sequences). To evaluate the influence of long duration ground motions on structural collapse, the influence of duration on earthquake-induced collapse is evaluated and the study is taken further by assessing structural damage and collapse risk under other seismic events in nature where long

duration shaking occurs: (1) subduction earthquakes and (2) earthquake sequences including mainshock-aftershock sequences.

This Ph.D. dissertation is divided into 4 chapters, wherein Chapter 1 provides a brief introduction to the thesis and Chapters 2, 3 and 4 cover the damage assessment of reinforced concrete buildings on being subjected to long duration ground shaking, including subduction earthquakes and mainshock aftershock sequences. Chapter 2 is already a journal paper published in *Structural Safety*; Chapters 3 and 4 are also written as stand-alone papers for publication. There may be some redundant information among different chapters due to this format. All of the studies focus on RC buildings because they are a prevalent form of construction in high seismic regions of US.

Chapter 2 describes a study carried out to quantify the influence of duration of ground motion on structural collapse capacity. A set of 17 RC frame buildings was subjected to ground motions of varying duration. Results show the collapse capacity of the structure decreases as the duration of ground motion increases. A Generalized Linear Model is fitted to the collapse capacity data, which predicts collapse capacity as a function of ground motion duration and structure's fundamental period and its ductility. The results from the study indicate that there is a higher risk associated with collapse of structures on being subjected to longer duration ground motion as compared to a counterpart shorter duration ground motion having the same intensity. The contents of Chapter 2 have been published in *Structural Safety* by Raghunandan and Liel (2013).

Chapter 3 assesses the collapse risk of structures in the Pacific Northwest region of the U.S. due to Cascadia subduction zone. The increased seismic hazard due to Cascadia subduction

zone was discovered only in 1980s, and was incorporated in building codes in 1994. Most of the current collapse assessment studies are carried out for crustal ground motions and the performance of structures under subduction ground motions having longer duration and distinct frequency content is not as well quantified. In this study a portfolio of 36 buildings of varying heights from 4 different design periods (1967 UBC, 1973 UBC, 1994 UBC and 2012 IBC) are subjected to sets of *Crustal* and *Subduction* ground motions to assess the collapse fragilities of buildings in the cities of Seattle and Portland. The results indicate that the building median collapse capacity is significantly reduced on being subjected to *Subduction* ground motions as compared to *Crustal* ground motions. The seismic collapse risk of the buildings is also evaluated by convolving the subduction and crustal building fragility curves with respective seismic hazard curves at sites in Seattle and Portland. These computations show the high contribution from subduction hazard to the total collapse risk of buildings. Through comparison with buildings designed for Los Angeles, the study also finds that the fragility of buildings to shaking from subduction events amplifies the risk of building collapse in the Pacific Northwest. This further reinforces the need to consider separate building fragility and seismic hazard curves for subduction and crustal ground motions in seismic risk assessment of buildings located at sites exposed to subduction earthquake hazard.

Chapter 4 quantifies the collapse fragility of buildings that are damaged in mainshock. The post-earthquake/aftershock building collapse fragilities are computed for a set of four modern California reinforced concrete frame buildings. The buildings are subjected to mainshock-aftershock sequences consisting of two ground motions. The post-earthquake building structural damage and collapse capacity is assessed based on the capacity of the mainshock damaged building to respond to the aftershock motion. A key variable is the level of

damage the building experienced during the mainshock. This study also quantifies the effectiveness of different physical damage indicators (*e.g.* interstory drift, roof drift) of mainshock damage in assessing post-earthquake safety. The results indicate that residual interstory drift along with residual roof drift are the best indicators of visual damage that are observed in post-earthquake building tagging evaluation (ATC-20).

The completion of this study serves to quantify the influence of duration of ground motion on structural collapse, which has not been previously studied. The evaluation of structural damage and collapse risk due to long duration ground shaking in a performance-based earthquake engineering framework can aid in improving building codes and post-earthquake inspections regimes by avoiding structural collapse which threatens life safety.

CHAPTER 2 EFFECT OF GROUND MOTION DURATION ON EARTHQUAKE-INDUCED STRUCTURAL COLLAPSE

2.1 Introduction

Earthquakes that have occurred in recent years, including those in Tohoku, Japan (M_w 9.0, 2011), Maule, Chile (M_w 8.8, 2010), and Sumatra, Indonesia (M_w 9.1, 2004), continue to remind us that very long duration ground shaking may occur at some sites(USGS 2012a). In the Tohoku earthquake, sites across Japan experienced ground motions lasting for 40s to 270s (Luca *et al.* 2011), compared to, for example, ground motion durations on the order of 6s to 30s experienced in the Loma Prieta earthquake (M_w 6.93, 1989) (PEER 2012). Although the effect of shaking duration on structural damage is not always clear, reconnaissance teams investigating damage in past events have repeatedly attributed damage in some events and at some sites to long duration shaking, and the associated high number of load reversal cycles. Ground motions generated from large magnitude events, such as the recent earthquakes listed above, and recorded at sites situated some distance away from the epicenter, are particularly likely to be of long duration. The buildings constructed at these sites should therefore be capable of withstanding the expected long durations in addition to the expected ground motion intensities. Present building codes and analysis procedures are based on the probabilistic site-specific design spectra that do not directly consider duration (ASCE 2010).

It is well-known that ground motion duration and the number of cycles have an important influence on some types of earthquake damage, such as inducing liquefaction and slope instability(Bray 2007; Green and Terri 2005). Yet, there remains disagreement in the research community on the effect of ground motion duration on structural response (Hancock and Bommer 2006). For example, experimental studies of reinforced concrete and steel elements or frames have typically concluded that duration or number of cycles of loading is positively

correlated to structural damage. The damage observed in connections of steel moment resisting frames in the Northridge and Kobe earthquakes was attributed to low cycle fatigue (*i.e.* many cycles). In addition, analytical studies adopting cumulative damage measures, like plastic strain, have generally found duration to be important in quantifying structural damage. However, analytical studies using maximum drift or displacement as a measure of damage in the structure contradict these findings, and generally have found no correlation between ground motion duration and increasing damage. Even in these types of studies, though, research employing structures with degrading characteristics and allowing for destabilizing effects of gravity loads shows that longer duration ground motions may in fact increase maximum structural responses. In summary, the relationship observed between ground motion duration and structural response is heavily dependent on the definition of ground motion duration and structural response parameter used and whether significantly nonlinear behavior and destabilization effects are considered (Hancock and Bommer 2006).

This paper explores the influence of ground motion duration on structural collapse risk, which is a critical metric of life safety. Structural collapse occurs due to a combination of large amplitude demands (which past research suggests is not strongly duration dependent) and damage accumulated over multiple cycles during the earthquake (which past research indicates is significantly duration dependent). Previous studies have shown how ground motion intensity and frequency content affect structural collapse risk and failure mechanisms (Baker and Allin Cornell 2005; Haselton *et al.* 2011; Ibarra *et al.* 2005; Zareian and Krawinkler 2007). However, the influence of duration, or the number of cycles imposed on the structure, is not well understood. One possible hypothesis is that long duration motions impose larger energy demands on the structure and therefore may cause collapse at lower ground motion intensities. This hypothesis is

supported by work by Ruiz-Garcia (2010) and Iervolino *et al.* (2006), which suggests that duration may be more important for collapse than other, more linear limit states, but it has not been directly explored. To further complicate matters, the ground motion duration itself is related to earthquake features like magnitude, distance to site, and fault type (Bommer *et al.* 2009), so it is difficult to decouple the effects of duration from other earthquake and ground motion characteristics. Understanding the effect of ground motion duration on structural collapse risk and failure mechanisms will bring us one step closer to preventing future earthquake-induced collapses.

This study quantifies the influence of ground motion duration on the predicted collapse response of concrete frame structures. Incremental dynamic analysis is carried out on a set of 17 archetypical reinforced concrete buildings representative of modern and older construction in high seismic regions of the U.S. Each of the analytical building models is subjected to a database of 76 ground motion time histories with varying duration. The simulations use nonlinear multiple-degree-of-freedom models, which are capable of capturing strength and stiffness deterioration, along with destabilizing effects of gravity loads. The collapse capacity of each structure is quantified by the median ground motion intensity causing collapse, measured in terms of inelastic spectral displacement. Once these results are obtained, the inelastic spectral displacement at collapse for all the buildings is studied as a function of duration, and the structure's fundamental (first-mode) period and ductility capacity using general linear modeling (GLM) regression techniques. In doing so, we expand on previous research by quantifying the correlation between duration and structural collapse resistance, which is a combined mechanism of different damage and response measures that have been studied independently before, utilizing nonlinear analysis models representing realistic building designs.

2.2 Ground Motion Duration

A ground motion time history or accelerogram, recorded from a particular earthquake at a particular site, can be characterized by a number of parameters including amplitude, frequency content, energy, and duration of shaking. There are many definitions for ground motion duration available in literature (Bommer and Martínez-Pereira 1999). Bracketed duration considers the amplitude of the ground motion to measure the duration and is defined as the length of the time between which the absolute accelerogram exceeds some threshold acceleration (*e.g.* 0.1g) for the first and last time. The significant duration, on the other hand, is defined based on the energy of the ground motion record. Several measures serve as proxies for the total energy of the accelerogram, including the integral of the square of the acceleration history over time *a(t)*, which is known as the Arias intensity (*AI*) and is calculated as

$$AI = \frac{\pi}{2g}\int_0^{T_r} a^2(t)\,dt \tag{2.2.1}$$

where T_r is the total recorded time of the accelerogram and g is the acceleration due to gravity. Among the different definitions of significant duration present in the literature, the 5-95% significant duration (Trifunac and Brady 1975) is employed here, as it has been used and recommended by a number of other studies (Foschaar *et al.* 2012; Hancock and Bommer 2006). The 5-95% significant duration, denoted *5-95%* D_s, is calculated as the interval between the times at which 5% and 95% of the Arias Intensity of the ground motion have been recorded, representing the duration of time over which 90% of the energy is accumulated. Although the total length of the accelerogram may vary depending on the recording device, the *5-95%* D_s quantifies the length of the strongest part of the ground motion time history, *i.e.* that part of the motion which may damage a structure. This duration definition is also independent of the scaling

of the record, as the rate of accumulation stays the same, and also does not vary with ground motion frequency content. Figure 2.1(a) shows two recorded ground motions having the same peak ground accelerations (*PGA*), but different durations. The Arias Intensity plot (Figure 2.1 (b)) shows that the energy accumulates over more time for the longer duration ground motion as compared to the shorter duration ground motion. The time histories in Figure 2.1 (a) also illustrate the greater number of load reversal cycles for the longer duration record.

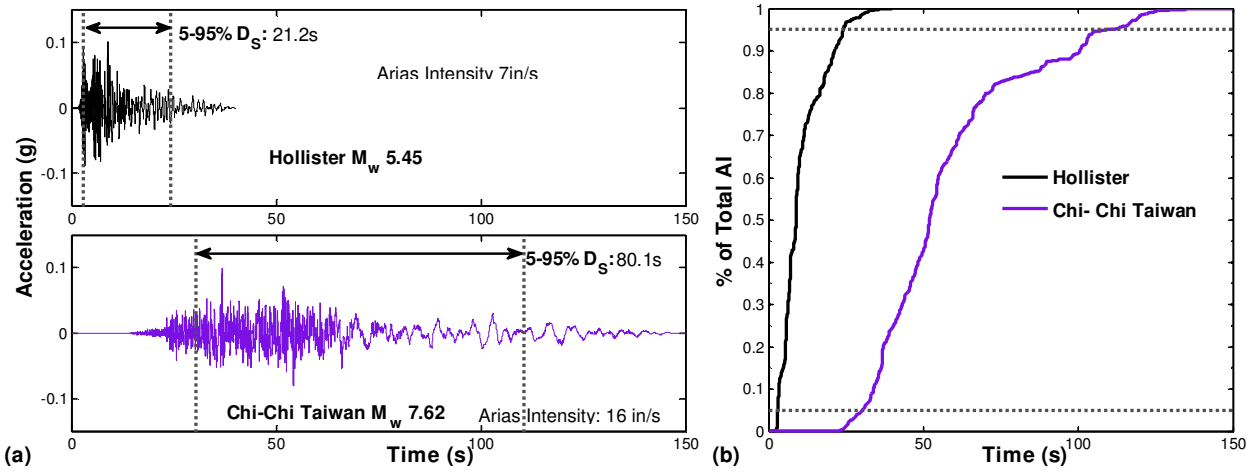

Figure 2.1 (a) Ground acceleration time histories and (b) Arias intensity for Hollister (NGA Sequence Number: NGA0498) and Chi-Chi Taiwan (NGA1181) ground motion recordings with the same peak ground acceleration (*PGA*), but different durations.

2.3 Ground Motion Database

To consider a broad range of ground motion duration values, 76 ground motion records with *5-95% D_s* varying between 1.1s to 271.3s are used in the dynamic analysis. The distribution of duration values in the record set is illustrated in Figure 2.2(a). Details of the records are provided in Appendix 2.A. These ground motion records are obtained from the Pacific Earthquake Engineering Research Center (PEER) Next Generation Attenuation database (PEER 2012), the COSMOS virtual data center (COSMOS 2011), and the USGS National Strong-Motion Project (USGS 2012b). The records are from 24 different earthquakes with M_w 4.8 and above, with the maximum number of the records from a single event being limited to eight. Due

to lack of availability of recordings for large long duration ground motions, particularly those from potentially large magnitude subduction events, this study also uses eight simulated records from Yang (2009), in addition to the 68 strong motion recordings. Among short duration records, of which there are many ground motion recordings available, records with the largest *PGAs* were selected. To avoid any near site effects or effects of rupture directivity, only ground motions without large pulses in the velocity time history are used in dynamic analysis (Baker 2007). The record selection process did not consider spectral shape, but this is not expected to have a critical influence on the fragility predictions, due to the use of an inelastic ground motion intensity measure (described later in Section 2.5).

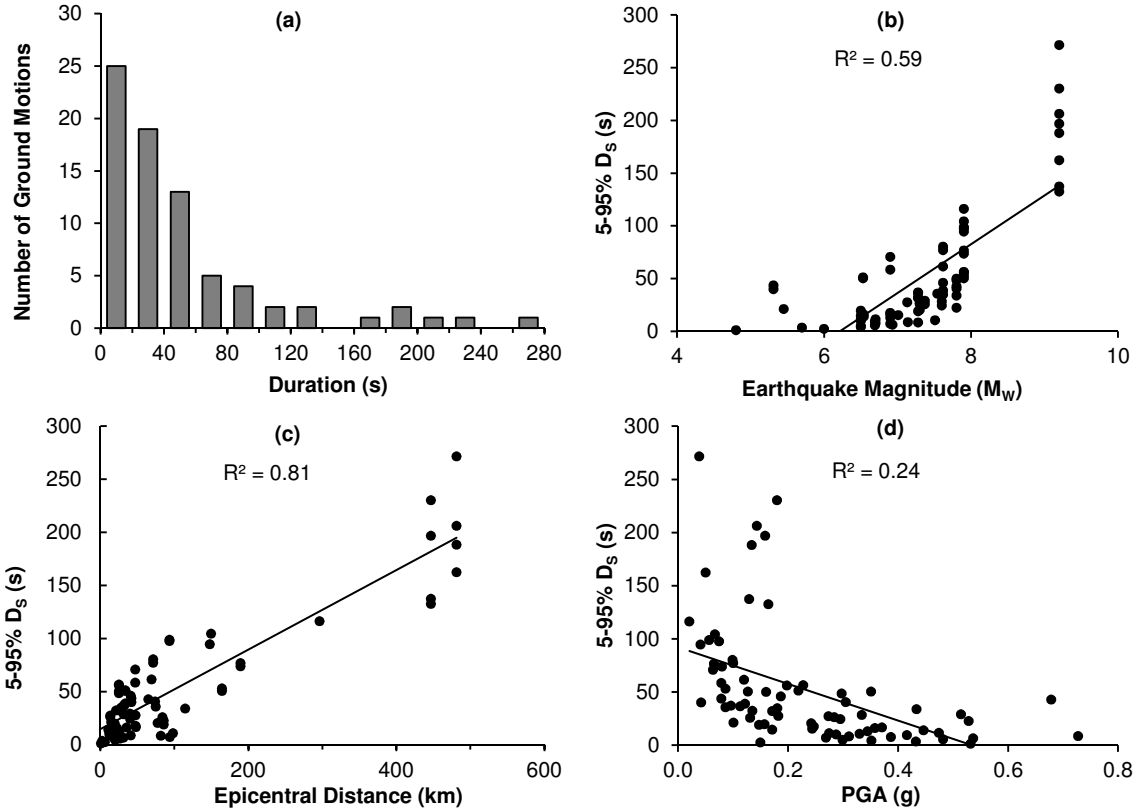

Figure 2.2 Distribution of ground motions in database according to (a) duration, (b) moment magnitude (M_w), (c) epicentral distance and (d) *PGA*.

The significant duration of a ground motion at a site depends on various factors, such as earthquake moment magnitude, distance to the fault rupture, depth to the top of rupture, soil type and the type of earthquake (Bommer *et al.* 2009). Seismological theory and models predict that duration of shaking at the source increases with an increase in seismic moment or earthquake magnitude (Kramer 1996). As the magnitude of the earthquake increases, so does the length and area of the fault rupture, which increases the time taken for the strain energy to release, resulting in longer strong motion durations at the source. The ground shaking duration modifies further as waves travel to a particular site, due to the factors such as soil and distance (Bommer *et al.* 2009). In general, as seismic waves scatter with distance between the source and site, the duration of ground shaking tends to become larger because of the increased difference in time between the arrivals of different seismic waves. Ground motion recordings from soil sites usually exhibit longer durations than rock sites (Bommer *et al.* 2009).

This study uses ground motion records from crustal and subduction events (M_w 4.8 - M_w 9.2), and the increase in duration with magnitude for these ground motions can be seen clearly in Figure 2.2 (b). The relationship between site epicentral distances and duration is also apparent in the record set, as shown in Figure 2.2(c). Record *PGAs* vary between 0.02g and 0.73g. Figure 2.2(d) shows that most of the long duration records have low *PGA* because they are recorded at large distances from the source, and seismic wave amplitudes have attenuated significantly (Bommer *et al.* 2009). Long duration records also may have differences in frequency content and response spectra shape from shorter duration records (Atkinson and Boore 2003); this issue is addressed in further detail in the discussion of ground motion intensity measures in Section 2.5. The database ground motion recordings are mostly for stiff soil and rock sites.

2.4 Building Design and Analytical Modeling

To assess the effect of the ground motion duration on the collapse of structures, nonlinear dynamic analysis is conducted for 17 archetypical reinforced concrete building models designed and detailed according to the requirements of past and present U.S. seismic codes. The use of this wide array of building models, which vary in terms of the fundamental period, ductility capacity and other key properties, enables us to quantify the influence of ground motion duration on the response of buildings with different structural properties.

The buildings in this study can be broadly classified into two categories: (a) modern ductile reinforced concrete frames and (b) older non-ductile reinforced concrete frames. It is meaningful to consider modern-type ductile buildings because current seismic codes do not directly address ground motion duration in design. The inclusion of non-ductile concrete frame buildings is important because these structures are prevalent in high seismic regions worldwide, and may be particularly vulnerable to earthquake-induced collapse (Liel *et al.* 2011). The modern ductile frames are designed by Haselton *et al.* (2011) according to the provisions of the International Building Code (ICC 2003), ASCE 7-05 (ASCE 2005), and ACI 318-02 (ACI 2002). These buildings satisfy all the requirements of so-called "special" moment resisting reinforced concrete frames, including strong-column-weak-beam requirements, shear capacity design and detailing requirements. The group of non-ductile buildings is designed by Liel et al. (2011) in accordance with Uniform Building Code (ICBO 1967) for the highest seismic zone at that time (*i.e.* California). These frames have somewhat lower strength and significantly lower deformability than the modern frames of comparable height. In particular, the low quantity and poor detailing of transverse reinforcement in structural elements and joints makes them susceptible to brittle failure modes. Table 2.1 provides the height, framing system (space or

perimeter frame type) and other design details for each building. The last column in Table 2.1, μ_T, provides one measure of the building ductility capacity, or the amount of inelastic deformation the structure can undergo, as obtained from static pushover analysis. Note that there are other measures of building ductility capacity, but this pushover-based measure defined by FEMA P695 (FEMA 2009) is used here to quantify relative differences in building deformability. Additional documentation of building design and modeling can be found in Haselton *et al.* (2011) and Liel *et al.* (2011).

Table 2.1 Building design information.

ID[a]	T_1 [b] (s)	Design Base Shear Coefficient [c]	μ_T [d]
02MS	0.60	0.125	15.9
04MP	1.08	0.092	11.5
04MS	0.91	0.092	12.4
08MP	1.69	0.050	10.3
08MS	1.81	0.050	7.7
12MP	1.97	0.044	13.0
12MS	2.15	0.044	7.3
20MP	2.59	0.044	9.1
20MS	2.53	0.044	9.6
02OS	1.03	0.086	3.4
02OP	1.00	0.086	8.0
04OP	1.89	0.068	2.7
04OS	1.92	0.068	2.4
08OP	2.33	0.054	2.2
08OS	2.23	0.054	2.6
12OP	2.73	0.047	2.1
12OS	2.35	0.047	2.9

[a] Building information provided in ID: First two characters indicate the number of floors; third character "O" denotes older design and "M" denotes modern design; last character indicates "S" for space frame and "P" for perimeter frame.
[b] First-mode elastic (fundamental) structural period based on eigenvalue analysis, considering cracked concrete sections.
[c] Ratio of the design base shear to the building weight (V_{design}/W).
[d] Ductility capacity as determined by nonlinear static pushover analysis.

The archetypical buildings are modeled as two-dimensional, three-bay frames of varying height, as shown in Figure 2.3. These models are implemented in OpenSees (OpenSees 2012), an open-source, object-oriented software platform developed by PEER. In order to simulate structural response up to the point of structural collapse, the nonlinear analytical models must be capable of capturing important modes of deterioration and failure. Accordingly, a model

comprised of lumped plasticity beam-column elements and inelastic joint shear springs has been used to represent the flexural behavior of beams and columns and joint shear failure. The plastic hinges in the lumped plasticity beam-column element are modeled using the hysteretic material developed by Ibarra *et al.* (2005), which is capable of simulating stiffness and strength degrading hysteresis behavior of the beams and columns as the structure collapses. Examples of the tri-linear monotonic backbone curve and the hysteretic behavior of the element hinges and joint springs are provided in Figure 2.4. The plastic hinges' negative post-capping stiffness represents strain softening response caused by spalling of cover concrete and buckling of longitudinal reinforcing bars. Model parameters for beam-column hinges are determined from the empirical equations obtained by calibrating the Ibarra hysteresis model to more than 250 experimental tests of concrete columns (Haselton *et al.* 2008). Therefore, model properties such as rotation capacity and post-capping stiffness vary according to the design and detailing properties of each frame and beam or column. A key parameter from the perspective of this study is the cyclic deterioration, which is modeled in each hinge by a parameter λ that represents the cyclic hysteretic energy dissipation capacity of the element (Ibarra *et al.* 2005). The values of λ have been calibrated to experimental data such that more ductile well-detailed columns and beams have higher λ, indicating that the element is able to dissipate more energy and has a lower rate of strength and stiffness deterioration (Haselton *et al.* 2008). Prediction of column shear failure and loss of gravity load bearing capacity in dynamic analysis is progressing with newly developed computational models (Elwood 2004; Ghannoum *et al.* 2008), but is not considered in this study and models do not capture shear critical column response. The modern building columns are designed to prevent this failure mode through capacity design provisions of transverse reinforcement. In the older buildings, columns are assumed to display flexure-shear failure, *i.e.*

yielding before shear failure occurs. Foundation flexibility is modeled with an elastic, semi-rigid rotational spring at the base of each column. Destabilizing P-Δ effects are incorporated using a nonlinear geometric transformation. In addition, a leaning column of truss elements is connected to the frame by rigid struts (Figure 2.3). The load, P, on the leaning column includes the gravity loads that are not tributary to the modeled 2-dimensional frame.

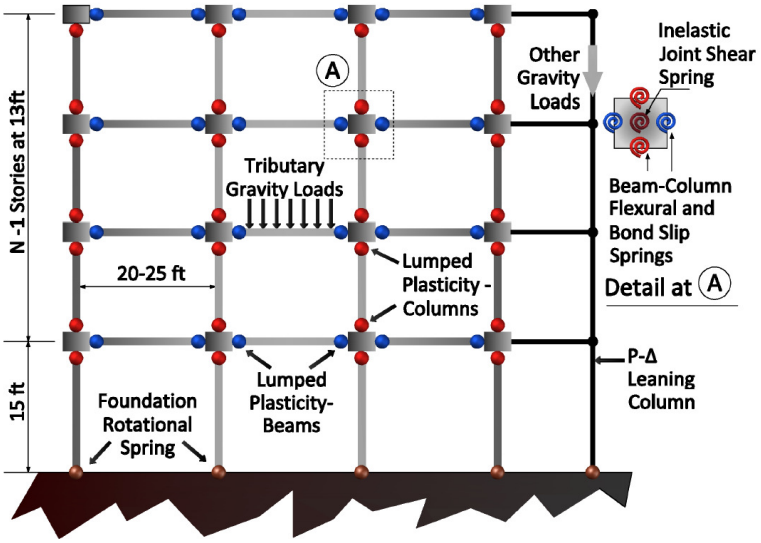

Figure 2.3 Schematic of N story building model showing key nonlinear elements used for dynamic analysis.

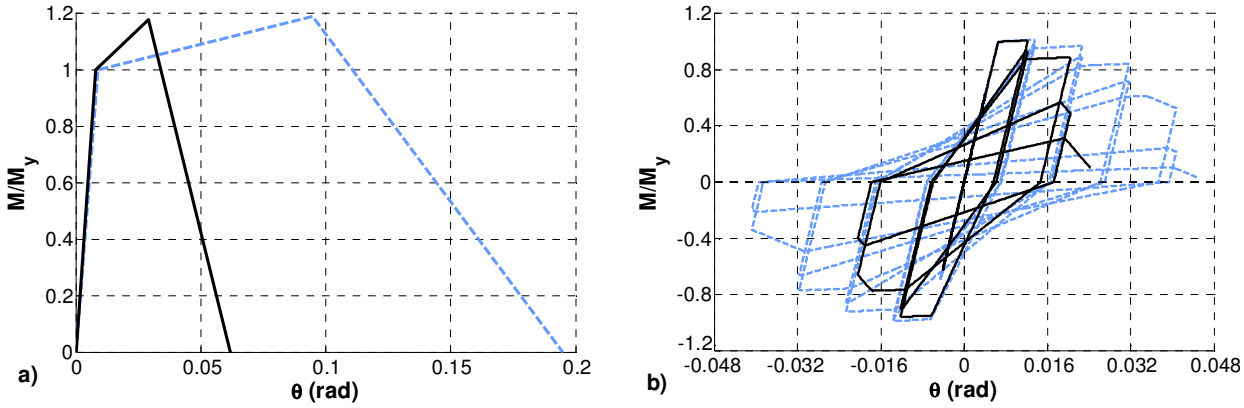

Figure 2.4 Properties of component model for the typical ductile (dashed) and non-ductile (solid) reinforced concrete columns, illustrating differences in (a) monotonic and (b) cyclic behavior (Liel *et al.* 2011).

2.5 Nonlinear Analysis

The seismic response of the building model is evaluated using incremental dynamic analysis (IDA) (Vamvatsikos and Cornell 2002). In IDA, a nonlinear building model is subjected

to a ground motion with a particular intensity, and the time history of building response, including key engineering demand parameters such as peak interstory drift, roof drift, or floor acceleration, are measured. The ground motion record is then scaled to increasing intensity and dynamic analysis is repeated. This procedure of scaling and time history analysis is repeated until dynamic instability in the form of large interstory drifts occurs, indicating building collapse. The severity of the ground motion is quantified using an intensity measure such as *PGA* or $S_a(T_1)$, the spectral acceleration at the first-mode period of the building. Scaling of records is needed to simulate the behavior of the structure to varying levels of seismic demand, providing insight into how the structure might respond under rare large intensity ground motions, for which few or no recordings are available. To account for record-to-record variability in frequency content and other ground motion features, the analysis is conducted for a suite of different ground motions.

Recent research has shown that, in addition to the ground motion intensity, the spectral shape of ground motions affects inelastic structural response (Baker and Cornell 2006). The intensity measure conventionally used in building fragility analysis, $S_a(T_1)$, does not account for the spectral shape of the ground motion record because it represents the response spectral value only at a single period, usually the fundamental period of the structure. In particular, $S_a(T_1)$ does not capture period elongation and higher mode effects, such that different ground motions with the same $S_a(T_1)$, but different shapes, may affect highly nonlinear multiple degree of freedom structures differently. This observation is significant because rare ground motions that are large enough to cause collapse have a distinct shape (Baker and Cornell 2006). Other intensity measures, such as peak ground velocity (*PGV*), which is correlated to the failure of long period structures, suffers from a similar deficiency because it does not cover the wide range of

frequencies required to adequately capture the spectral shape of the ground motion recording (Matsumura 1992). The use of inelastic spectral displacement, or S_{di}, as an intensity measure, has been shown to be effective in representing both ground motion intensity and the spectral shape effect (Tothong and Luco 2007).

Inelastic spectral displacement is calculated as the maximum (spectral) displacement of a single-degree-of-freedom oscillator with bilinear material properties (Tothong and Cornell 2006). S_{di} is typically calculated for 5% damping, and depends on the specified first-mode elastic period and the yield displacement of the oscillator, d_y (Figure 2.5 (a)). In this study, d_y is obtained from nonlinear pushover analysis of building model and is structure-specific (FEMA 2009). The bilinear oscillator is assumed to have a 5% post-yield hardening stiffness ratio and is infinitely ductile. The shape of the response spectra for periods greater than the oscillator's fundamental period is implicitly captured by S_{di}, due to the oscillator yielding and elongation of the oscillator period (Tothong and Cornell 2006). Because S_{di} accounts for spectral shape variability as well as ground motion intensity, its use reduces record-to-record variability in structural response as compared to other intensity measures (Ruiz-Garcia 2010). S_{di} does not account for the portion of the spectra where periods are shorter than the first-mode period, which may influence higher modes. Nevertheless, this study uses S_{di} as an intensity measure due to its simplicity and at the same time its suitability in accounting for the most important issues related to spectral shape, since higher modes are not critical for the building set of interest. Since long duration records tend to have different frequency content than their short duration counterpart because of the type of rupture and wave path effects (Atkinson and Boore 2003), the use of S_{di} is particularly important here, because it allows us to focus on ground motion duration distinct

from spectral shape issues. Also, if S_{di} is used, structural response results have been shown to be unbiased by the scale factor applied to the record before the analysis (Tothong and Luco 2007).

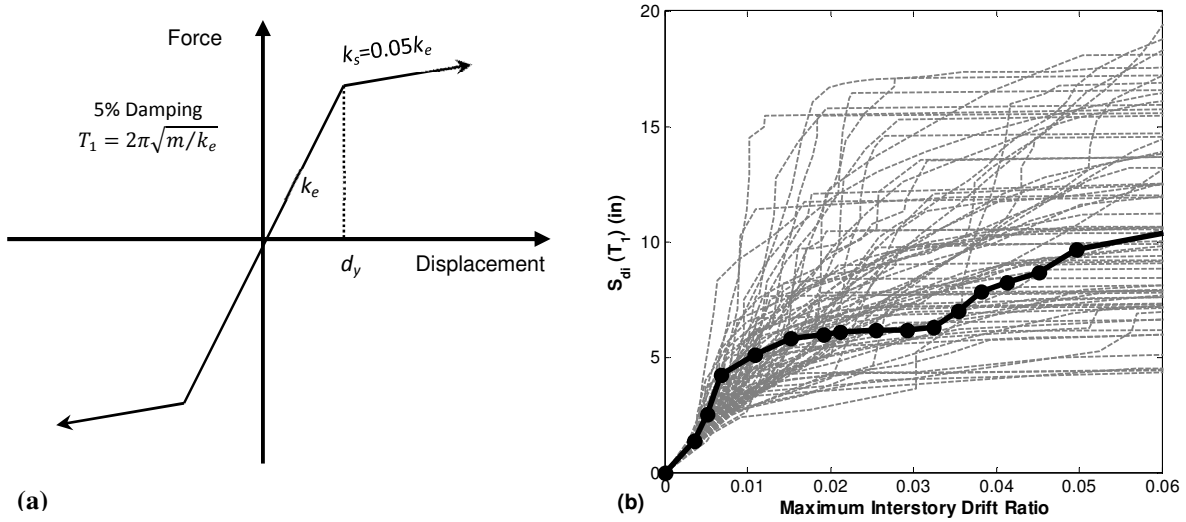

Figure 2.5 (a) Properties of the single-degree-of-freedom oscillator used in calculation of inelastic spectral displacement, S_{di}, (b) Incremental dynamic analysis results for the 4 story modern reinforced concrete building (04MP).

IDA results for the 4 story modern reinforced concrete space frame (04MP) are shown in Figure 2.5 (b), where, the interstory drifts are plotted for increasing levels of inelastic spectral displacement for 76 different ground motions. The black line highlights IDA results for one of the ground motion time histories, describing the trends in the maximum interstory drift of the structure as it is subjected to increasing intensities of same ground motion. The results for the other ground motions are shown in gray.

2.6 Collapse Analysis Results

2.6.1 Overview

The collapse capacity of a structure is quantified by a ground motion's inelastic spectral displacement when it is scaled to level at which structural collapse occurs. A larger value of S_{di} at collapse (for a particular building period and d_y) indicates that the structure is able to withstand larger ground motion intensities before the collapsing. To quantify the influence of ground

motion duration on the collapse capacity of a structure, a multivariate regression model is fitted to structural analysis results from all buildings using the generalized linear model (GLM) framework (Fox 2008). In the process of finding the best-fit GLM model, the influence of various building properties (*e.g.* fundamental period, ductility or deformation capacity, and lateral load resisting system) and ground motion properties (*e.g.* peak ground acceleration and significant duration) on the collapse S_{di} is considered. Figure 2.6 shows the relationship between collapse S_{di} and duration for four different buildings, where each marker indicates the collapse S_{di} value recorded for one of the 76 ground motion records and the curves represent the fitted GLM models. Results for all the buildings show a decrease in collapse S_{di} with increasing ground motion duration.

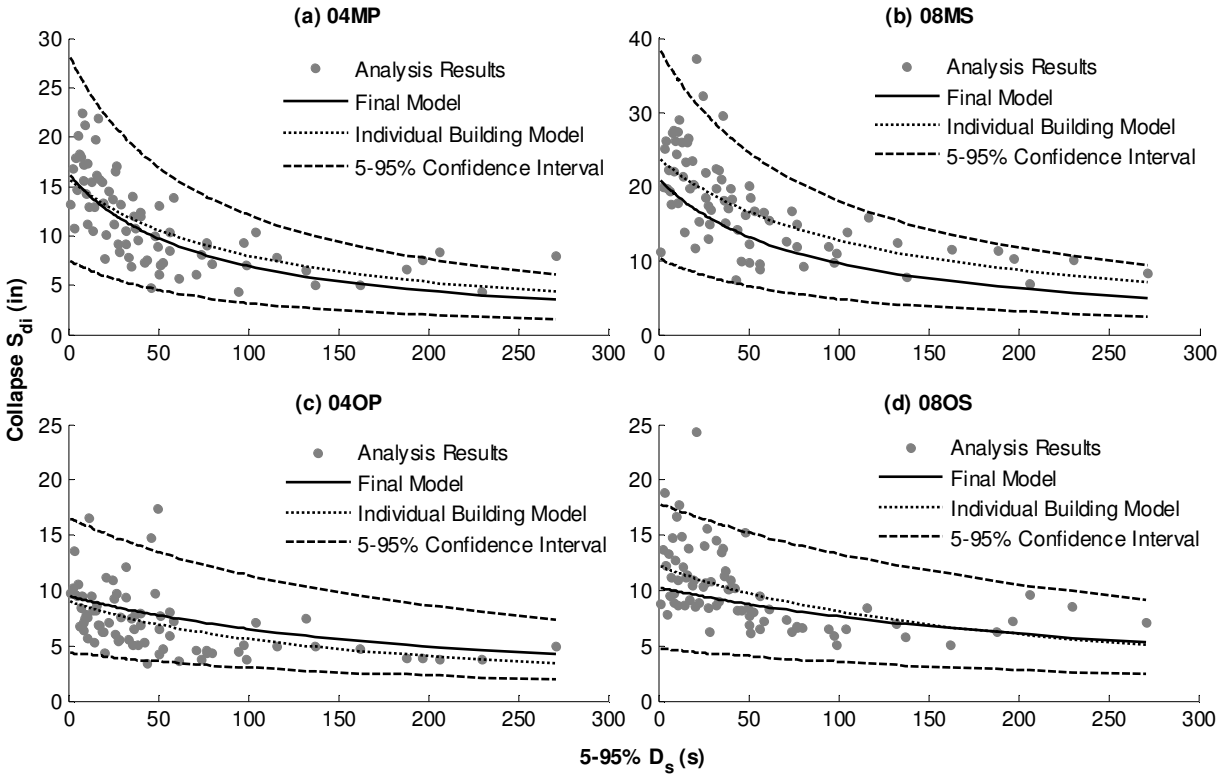

Figure 2.6 Variation of Collapse S_{di} with Ground Motion Duration for (a) Modern 4 Story building, (b) Modern 8 Story Building, (c) Older 4 Story Building, and (d) Older 8 Story Building.

In Figure 2.6, and the discussion below, the best GLM model fitted to the data from all buildings, the so-called "common" or "final" model, indicates that the collapse capacity of a structure depends on its ductile or non-ductile nature and its fundamental period, along with the duration of the ground motion to which it is subjected. The curve labeled "individual building model" has been fitted only to the results from that particular building model. The development of the GLM model and the functional form is discussed in more detail in the following sections.

2.6.2 Statistical Analysis of Collapse Results

The structural collapse capacity variable, S_{di}, is modeled using GLM as a function of two structural parameters, the building's fundamental period (T_1) and its ductility capacity, and a ground motion duration parameter (*5-95% D_S*). Building ductility capacity is included in the model by assigning building ductility flag values of $B_F = 1$ for the modern ductile buildings and $B_F = 2$ for the older non-ductile buildings. We also computed building-specific structural ductility capacity parameters from nonlinear pushover analysis (reported in Table 2.1) as possible predictors for preliminary GLM models, but the flag variable distinguishing simply between those buildings that are quite ductile (quantitatively representing ductility values obtained from pushover analysis with $\mu_T \geq 7$) and those that are not ($\mu_T \leq 7$) was found to be a more significant predictor collapse S_{di} than the building-specific values. Mathematically, the GLM model can be expressed as:

$$\boldsymbol{S_{di}} = f\left(\boldsymbol{T}_1, \boldsymbol{B_F}, \boldsymbol{D_S}\right) + error \qquad (2.6.1)$$

GLMs are a general form of the linear regression models. In linear regression modeling, the vector of response variables, $\boldsymbol{Y}$ (in our case, collapse $\boldsymbol{S_{di}}$)**,** is expressed as a linear

combination of n predictor variables, $\boldsymbol{X} = [1, x_1, x_2, \ldots, x_n]$ (in our case, $x_1 = \boldsymbol{T_I}$, $x_2 = \boldsymbol{B_F}$ and $x_3 = \boldsymbol{D_S}$):

$$\boldsymbol{Y} = \boldsymbol{X}^T \boldsymbol{\beta} + error \tag{2.6.2}$$

$\boldsymbol{\beta}$ is the (1+n) x 1 vector of estimated model parameters (*i.e.* regression coefficients) for the predictor variables $\boldsymbol{X}$. A linear least-squares regression model is appropriate for a continuous response variable, $\boldsymbol{Y}$, which is normally distributed with constant variance. In GLM, the distribution of $\boldsymbol{Y}$ may follow any exponential family distribution whose parameters can be varied to represent both discrete (*e.g.* binomial, Poisson) and continuous (*e.g.* normal, gamma) probability distributions. The GLM methodology also introduces a linearizing link function *g(.)* which is a one-on-one continuous differentiable transformation between the expectation of the response variable E($\boldsymbol{Y}$) and the linear predictor $\boldsymbol{X^T \beta}$.

$$g\left(E\left[\boldsymbol{Y}\right]\right) = \boldsymbol{X}^T \boldsymbol{\beta} \tag{2.6.3}$$

The expected value of $\boldsymbol{Y}$ predicted using GLM is therefore calculated as:

$$E\left[\boldsymbol{Y}\right] = g^{-1}\left(\boldsymbol{X}^T \boldsymbol{\beta}\right) \tag{2.6.4}$$

The link function varies for different distributions of $\boldsymbol{Y}$. The typical linear regression model is a special case of GLM where $\boldsymbol{Y}$ has a normal distribution and the link function is the identity function.

In this study, the response variable values of $\boldsymbol{Y} = \boldsymbol{S_{di}}$ are assumed to follow a gamma distribution. The gamma distribution is capable of mimicking the shape of the lognormal or the

exponential distribution by varying its parameters. This property makes the gamma distribution a good choice for S_{di} because collapse capacities are continuous and positive, and are typically assumed to follow a lognormal distribution. The gamma distribution requires a simple reciprocal (inverse) link function to define the relationship between the linear predictors and response variable such that:

$$E[S_{di}] = g^{-1}\left(X^T\beta\right) = \frac{1}{X^T\beta} \tag{2.6.5}$$

This inverse link function captures the nonlinear variation of S_{di} with respect to its predictor variables. The gamma distribution is defined by a shape parameter, which controls the skewness of the distribution, and a scale parameter, which is related to the spread of the distribution (Myers *et al.* 2010). To calculate the expected value (mean) of the response parameter, the GLM methodology uses a constant shape parameter and scale parameters changing across the predictor variables to capture the variation in the variance of data. When the shape parameter is constant, the gamma distribution has a non-constant variance that is directly proportional to the square of the mean.

The GLM modeling is carried out using the *glm* package in *R* (R 2011), which estimates the model parameters by an iterative procedure that maximizes the likelihood function to determine the most probable parameter values for the given observed data. The GLM model is fitted for different combinations of one, two or three of the predictor variables T_1, B_F and D_S and multiplicative interaction variables (*e.g.* $T_1 \times B_F$) between them. The analysis is carried out on a single matrix for all 17 buildings and all 76 ground motions with a 1292 x 1 S_{di} vector as the response variable and a 1292 x (1 or 2… or 6) predictor variable matrix X. The predicted

residual sum of squares (PRESS) for each model is calculated and the "best" model is defined by the predictors and coefficients, $\boldsymbol{\beta}$, which minimize the PRESS (Predicted REsidual Sums of Squares) score (Weisberg 2005). The fitted GLM model, reported in Equation 2.6.6, shows that all three predictors and an interaction term between $\boldsymbol{D_s}$ and $\boldsymbol{T_1}$ are important. For comparison, separate GLM models were also fit to the data from each of the 17 buildings individually, and labeled as "Individual building model" in Figure 2.6.

$$E[S_{di}]\,(in) = \left[\frac{1}{\left(\begin{array}{c} 2.33x10^{-2} + 1.29x10^{-3} * D_s - 2.23x10^{-2} * T_1 \\ -4.28\ \text{x}10^{-4} * D_s * T_1 + 6.19\ \text{x}10^{-2} * B_F \end{array} \right)} \right] \tag{2.6.6}$$

The confidence intervals for the final model prediction can be obtained by calculating the 5 and 95% quantiles of the gamma distribution about each estimated response value (mean) with the shape and scale parameter values at that point. The confidence intervals were computed in the glm package in R and are illustrated for 4 typical buildings in Figure 2.6.

There are a variety of other measures of goodness of fit in the context of GLM. Analysis of Variance (ANOVA) is carried out on the final model predictors ($\boldsymbol{\beta}$), testing the statistical significance of each model parameter, which are themselves random variables. Table 2.2 summarizes the $\boldsymbol{\beta}$ values along with their standard error used in hypothesis testing. The null hypothesis stating that all coefficients $\boldsymbol{\beta}$ are zero can be rejected for all the predictors that have p value less than the significance value, α = 5%. The ANOVA results are summarized in Table 2.2 with p values extremely close to zero, indicating that the null hypothesis can be rejected and that each of the selected predictors is important.

Table 2.2 "Best" model parameters.

Model Parameter	β	Standard Error	p value
Intercept	2.33×10^{-2}	4.34×10^{-3}	9.2×10^{-8}
Duration, D_s	1.29×10^{-3}	8.59×10^{-5}	$<10^{-16}$
Fundamental Period, T_1	-2.23×10^{-2}	1.70×10^{-3}	$<10^{-16}$
$D_s \times T_1$	-4.27×10^{-4}	3.78×10^{-5}	$<10^{-16}$
Building Ductility Flag, B_F	6.18×10^{-2}	1.86×10^{-3}	$<10^{-16}$

The S_{di} estimates calculated according to Equation (2.6.6) have been shown for selected buildings in Figure 2.6 and are plotted against the actual values obtained from nonlinear analysis in Figure 2.7 (a). For a model that perfectly predicts the response variable, the estimated values from the GLM model would be the same as the actual values, falling on the 45^0 line. The GLM model follows this trend, with dispersion around 45^0 line representing the uncertainty in the prediction. To check the robustness of the chosen "best" GLM model, a cross-validation procedure is carried out. In cross-validation, a subset of the data is dropped from the original dataset and the GLM model is fitted to the remaining data (referred to hereafter as the "reduced model"). The reduced model is then used to predict values for the dropped subset of data. The robustness of the model is evaluated by its ability to predict values the reduced dataset has not seen before (i.e. the dropped values). Typically, around 10% of the data is dropped. In this study, the 76 observations associated with one building are dropped at a time. Figure 2.7 (b) shows that results from the reduced models results also follow the expected 45^0 line. In Figure 2.7 (c), the cross-validated and estimated S_{di} values are very similar.

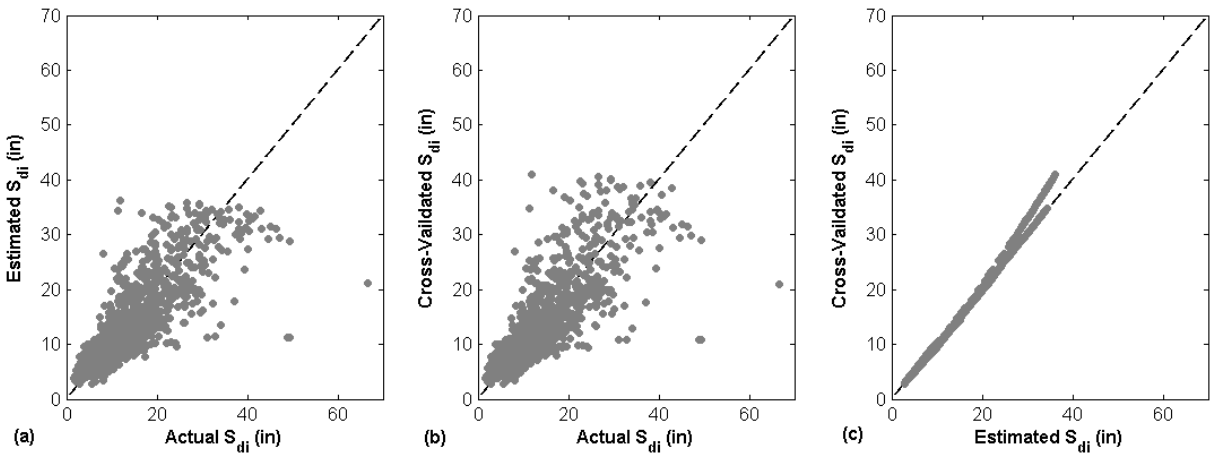

Figure 2.7 Comparison of the selected "best" GLM model and cross-validated GLM models with collapse S_{di} from nonlinear analysis ("Actual S_{di}") for all buildings.

The "best" GLM model illustrated in Figure 2.8 shows variation in collapse $E[S_{di}]$ values with ground motion duration (*5-95%* D_s) and the fundamental period of structure (T_1) for the two subsets of buildings with different ductility capacities. The figure illustrates a clear decrease in collapse capacity with increase in duration for both ductile and non-ductile buildings. For example, for ductile and non-ductile buildings with T_1=1s, there will be a 23% and 15% decrease, respectively, in mean collapse capacity on being subjected to a ground motion record having *5-95%* D_s of 60s instead of a record having *5-95%* D_s of 30s. The longer duration ground motions require a structure to undergo a larger number of load reversal cycles, resulting in higher accumulation of damage and higher imposed energy demands at lower levels of ground motion intensity. This behavior is examined in more detail in Sections 2.6.3.2 and 2.6.3.3. Figure 2.8 further illustrates, unsurprisingly, that the modern buildings, which are designed and detailed to be ductile, have higher S_{di} collapse capacities than the non-ductile buildings regardless of *5-95%* D_s and T_1. As shown many times before (*e.g.* Ibarra *et al.* (2005), Liel *et al.* (2011)), structures with higher ductility capacity are able to deform more before collapsing, resulting in more energy dissipation, and enabling them to withstand higher amplitudes of shaking before collapsing. The difference in collapse capacities of ductile and non-ductile buildings reduces as

the ground motion duration increases, because the rate of decrease of collapse capacity with duration is higher for ductile buildings, as discussed in more detail in Sec 2.6.3.3. Figure 2.8 also shows that an increase in T_1 is associated with an increase in collapse S_{di} values. The effect of the fundamental period T_1 on the collapse S_{di} can be explained by the shape of inelastic displacement spectrum. Like the elastic displacement spectrum, inelastic spectral displacement for a particular ground motion tends to increase with longer building periods so this trend reflects the average shape of the spectra.

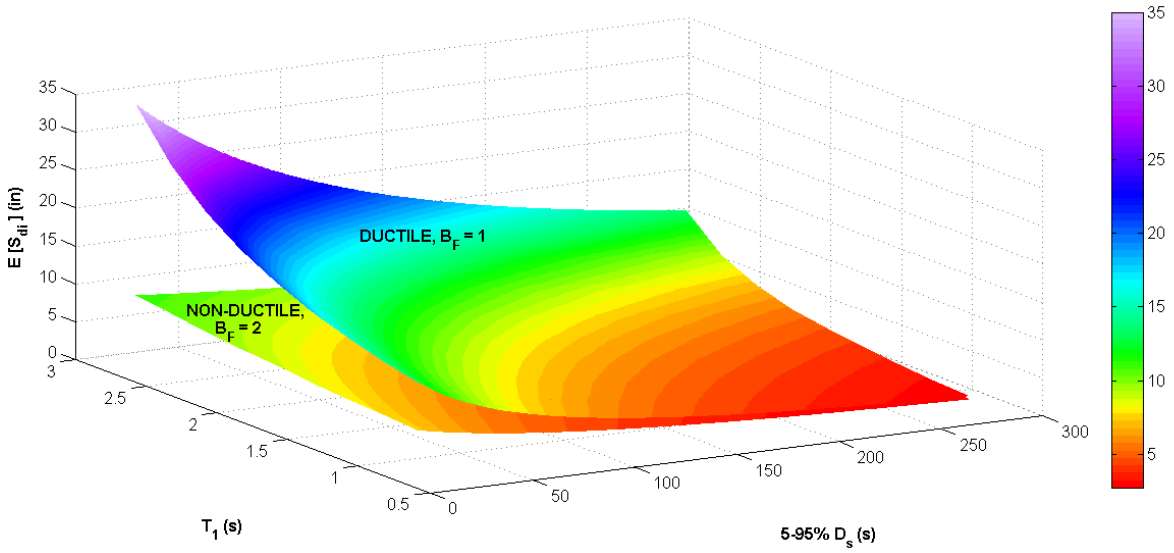

Figure 2.8 Variation of E[S_{di}]with *5-95% D_s* and T_1 from the final GLM Model.

2.6.3 Duration's Effect on Structural Collapse

The GLM model indicates that the collapse capacity of the structure is significantly affected by the duration of ground motion to which it is subjected. This section attempts to explicate the trends observed in the statistical analysis and to assess how variation in ground motion duration leads to differences in structural response.

2.6.3.1 Interstory and Residual Drift Demands

The time histories of interstory drift ratios and residual interstory drift ratios are two of the structural response parameters measured during the nonlinear dynamic analysis. Figure 2.9 shows the variation of maximum interstory drift (*i.e.* the peak transient drift in the building, considering all stories) during the time history, and maximum residual interstory drift at the end of analysis for the 4 story modern building (04MP) for all ground motion records, scaled to three different ground motion intensity levels. There is essentially no trend observed between the maximum interstory drifts or residual drifts and duration, at ground motion intensities of S_{di} = 2.25 in. (building undergoing linear behavior) and 7.5 in (building undergoing nonlinear behavior). (Figure 2.9 (a)-(d)). (For reference, the range of collapse S_{di} for 04MP building is 4.3-22.4 inches with around 21% of the records having collapse S_{di} less than 7.5 in.) This observation agrees with Hancock and Bommer's(2006) review of literature, which showed no relationship between duration and drift demands. In Figure 2.9 (e)-(f), results are plotted for each record for the ground motion intensity level just below the intensity level at which collapse occurs. Since each record collapses at a different level, the intensity of each of the ground motions in these figures is different. These results show a slight decrease in drifts as the duration of ground motion increases. This general decrease in drift values, although a bit scattered, is because the longer duration records are likely scaled to lower intensities because, as shown earlier, they cause collapse at lower ground motion intensities. According to the results shown in Figure 2.9 and similar observations for the other buildings, longer duration ground motion does not seem to lead to larger interstory or residual drifts in buildings, and hence, these drifts do not appear to be the explanation for why collapse occurs at lower ground motion intensities when subjected to the longer duration records.

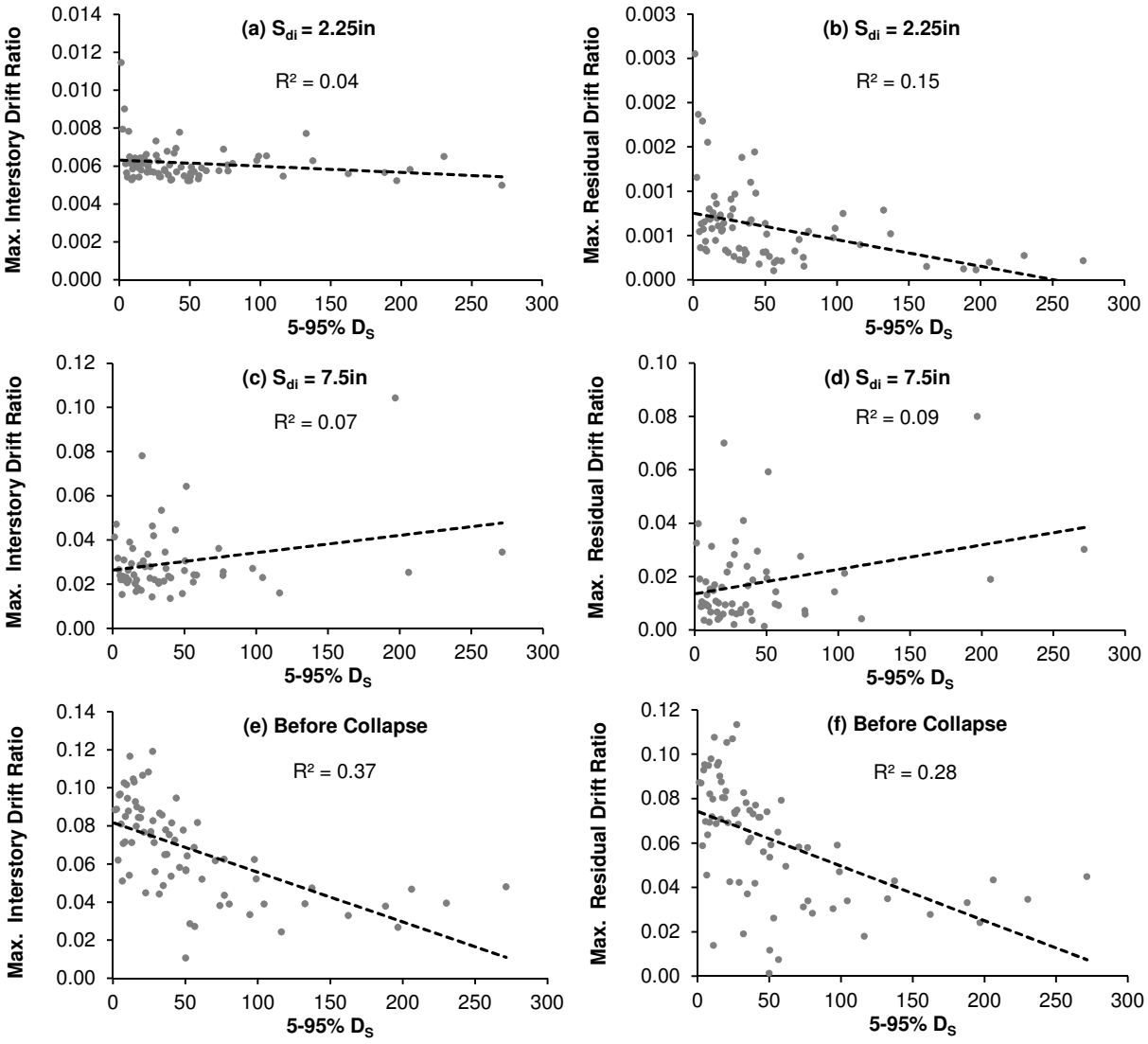

Figure 2.9 Variation of max. interstory drift and max. residual interstory drift when all ground motions are scaled to intensities of S_{di} =2.25 in. and 7.5 in. for the modern 4 story building (04MP). In (e) and (f) each ground motion is scaled to the intensity just below that causing collapse.

2.6.3.2 Hysteretic Energy Demand

To interrogate the differences in structural response under longer and shorter duration ground motions, the total hysteretic energy dissipated by a structure as it deforms on being subjected to each ground motion is calculated. During the course of ground shaking, seismic energy is transferred to the structure where it takes the form of kinetic energy or elastic strain energy, or is dissipated through damping and hysteretic behavior (Elnashai and Sarno 2008).

Hysteretic energy can be used to represent the energy dissipated by the structure or, alternatively, the energy demand on the structure on being subjected to a dynamic force having load reversal cycles such as an earthquake.

The hysteresis energy dissipated by the structure is equal to the area inside the hysteresis loop, which can be expressed in various ways: bending moment versus rotation, story shear versus lateral displacement, or axial forces versus axial displacements etc. For the purpose of this analysis, the hysteretic energy dissipated at each story over the duration of ground shaking is calculated as the area enclosed by the hysteresis loop formed by the earthquake-induced story shear forces and the relative displacement between floors at each story. The total hysteresis energy is calculated as the sum of hysteretic energy dissipated for all stories over the course of a particular ground motion time history.

Total Hysteretic Energy, $$E_H = \sum_{i=1}^{N} \sum_{j=1}^{n} E_{j,i,H} \quad (2.6.7)$$

Here, $E_{j,I,H}$ is hysteresis energy dissipated in the j^{th} cycle at the i^{th} story, n refers to the number of cycles in structural response and N is the total number of stories.

The total hysteresis energy calculated considers both elastic and inelastic displacements and so represents the sum of the elastic strain energy and inelastic hysteretic energy. Elnashai and Sarno (2008) proposed that the inelastic part of the energy dissipation of structure can be represented by a ductility factor based on total hysteresis energy, μ_E, which is defined as the ratio of total hysteresis energy to the elastic strain energy. In this formulation, the elastic strain energy is calculated as 0.5 x F_y x d_y, where F_y and d_y are the load and displacement at first yield. Accordingly, the trends observed between total hysteresis energy, E_H, and ground motion

duration will be the same as the trends between μ_E and ground motion duration for a building having a particular F_y and d_y. Therefore, we use the total hysteresis energy as a simple and efficient parameter for the examining variability in inelastic energy dissipation by a particular structure on being subjected to different duration ground motions.

The total hysteretic energy dissipated by the 04MP building model for different duration ground motions at different S_{di} levels is shown in Figure 2.10. More energy is dissipated by the system on being subjected to long duration ground motions in comparison to short duration ground motions at a particular ground motion intensity, as captured by the simple linear regression in Figure 2.10 (a)-(b). The greater energy demand from the long duration records for a given ground motion intensity level can be attributed to the larger number of cycles. The effect of the number of cycles becomes more significant at higher intensity levels, with greater inelastic deformations, as seen by the increase in regression line slope between Figure 2.10 (a) and (b). Figure 2.10 (c) shows the energy dissipated at the scale level just below that at which collapse occurs; the total energy dissipated at the intensity level just before collapse increases slightly with increasing duration. If the trendline were completely flat, the analysis would indicate that the same amount of energy demand is required to collapse the structure, regardless of duration. However, the longer ground motions, which are scaled to lower intensity levels, actually impose more energy demands on the structure compared to shorter duration records before collapse occurs, as indicated by the positive trend in Figure 2.10 (c). For a given imposed energy demand, short duration ground motions may be more damaging, in part because of pulse effects (Champion and Liel 2012), although we did not investigate this directly in our study. Similar results were observed for the other buildings.

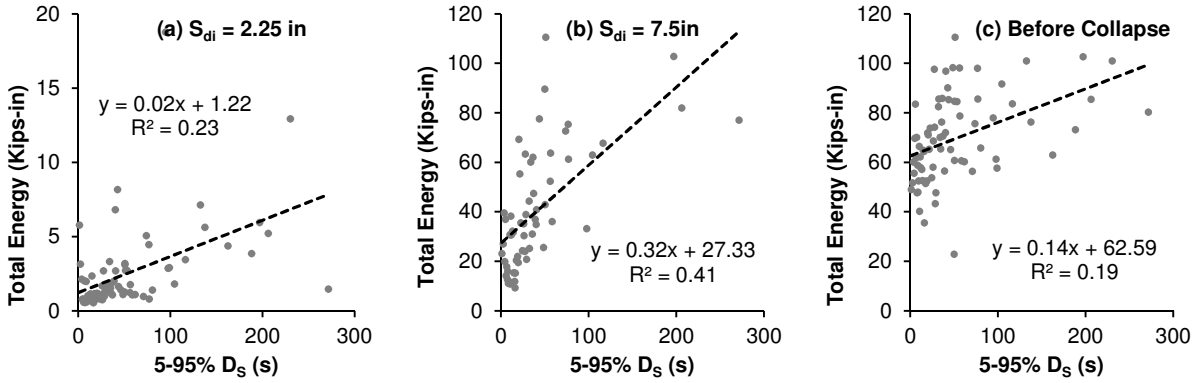

Figure 2.10 Total hysteretic energy dissipated by the modern 4 story building (04MP) at ground motion intensity levels of (a) S_{di} = 2.25 in, (b) S_{di} =7.5 in and (c) just before collapse.

2.6.3.3 Effect of Building Properties: Sensitivity Analysis

To further explore the relationship between duration, structural response and building properties, a simplified single-degree-of-freedom (SDOF) model is created and a sensitivity analysis is carried out by varying the SDOF's properties. The nonlinear properties of the SDOF were calibrated such that the static pushover analysis results from the multiple-degree-of-freedom (MDOF) model of the 4 story modern building (04MP) and the SDOF model matched as closely as possible. The SDOF model so calibrated has the same fundamental period, base shear coefficient and ductility capacity as the MDOF, as shown in Figure 2.11Figure 2.11 (a). To ensure the SDOF model has similar dynamic and cyclic behavior to the MDOF model, incremental dynamic analysis is carried out on SDOF models with this same backbone, but varying values of the cyclic deterioration parameter, λ. The SDOF model with λ that results in median collapse capacities nearly identical to the MDOF model for groups of short ($0 < 5\text{-}95\%\ D_s < 35$s) and long duration ($5\text{-}95\%\ D_s > 35$s) records is selected as the final calibrated SDOF model, also referred to as the "Base" model.

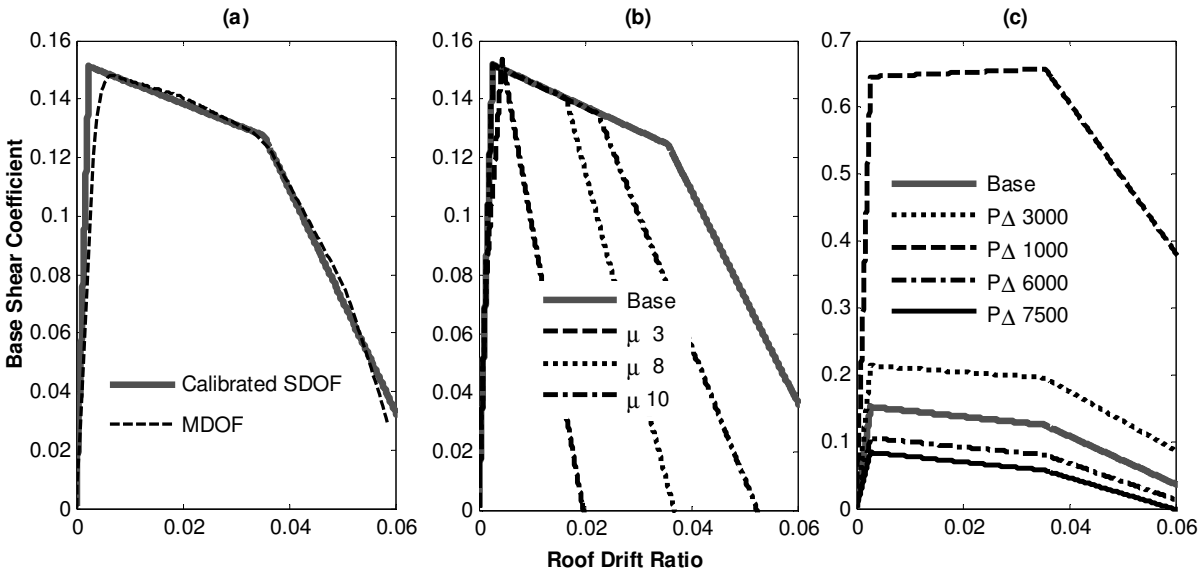

Figure 2.11 Pushover results (a) Comparing SDOF "Base" model and MDOF, (b) For SDOF "Set μ", (c) For SDOF "Set PΔ".

For the sensitivity analysis, three sets of SDOF models are created from the "Base" model by varying one structural property at a time. The first set of models, referred to as "Set λ," have the same monotonic pushover backbones, but different energy dissipation capacities, quantified by the model parameter λ. The "Base" model has $\lambda = 35$, and the other SDOF models have lower ($\lambda = 5$ *or* 20) and higher ($\lambda = 50$ *or* 65) values, indicating less and more energy dissipation capacity. For comparison, the equivalent SDOF to the ductile 4 story building has $\lambda = 35$ and the equivalent SDOF to the non-ductile 4 story building has $\lambda = 11$. The second set of models, "Set μ", have different building ductility capacities, but the same fundamental period, base shear, yield displacement, and cyclic deterioration parameters as the "Base" model (Figure 2.11 (b)). The "Base" model has a relatively high ductility capacity of 14.8 because it represents a modern, ductile building; the other models comprising Set μ have lower ductility capacities of 3, 8 and 10. The third set of models have different levels of gravity loads applied to the "Base" model, resulting in different levels of P-Δ effects on the structure. This set, referred to as "Set PΔ" and illustrated in Figure 2.11 (c), has the "Base" model with gravity load of 4812 kips

applied to the oscillator, the same as the MDOF, and models variations with gravity loads of 1000, 3000, 6000 and 7500 kips.

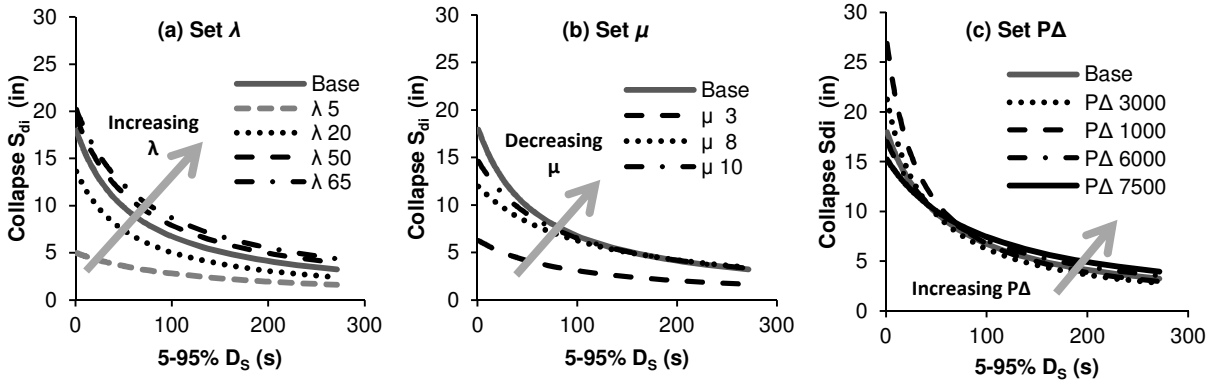

Figure 2.12 GLM model fitted for the SDOF models in sensitivity analysis showing effect of duration on response of SDOFs with varying (a) Energy dissipation capacities, (b) Ductility capacities and (c) P-Δ effects.

The SDOF building models are analyzed through IDA with the same set of ground motions used for the MDOF analysis. The analysis results enable us to assess the interaction between ground motion duration and structural response for buildings with different properties. A GLM model using the inverse link function is fitted to results for each SDOF building, to predict the collapse S_{di} as a function of the *5-95% D_s*; the fitted models for each set are illustrated in Figure 2.12. As expected, decreased energy dissipation capacity, *i.e.* decreased λ, generally brings down the collapse capacity of the structure for all ground motion durations, as shown in Figure 2.12 (a). In addition, the rate of decrease in collapse capacity with duration is bigger for models with more energy dissipation capacity, as indicated by the steeper slopes of the fitted GLM model for greater λ. Similarly for ductility capacity, Figure 2.12 (b) shows that the SDOF models with higher ductility capacity have larger collapse capacities, but that the rate of decrease of collapse capacity with duration is higher for more ductile models as compared to the less ductile models. For buildings in "Set PΔ", plotted in Figure 2.12 (c), higher gravity loads cause

decrease in overall collapse capacities for shorter durations due to P-Δ deformations, but the collapse capacities become very close in the long duration ground motion range.

These results indicate that duration is having a more significant influence on the collapse capacity of more ductile structures than those that are less ductile, which may seem counter intuitive. All buildings show a decrease in collapse capacity with increasing duration because, as the duration increases, the structure becomes unable to dissipate the energy imposed by so many cycles. Since the weaker, less ductile buildings (*i.e.* low μ_T and low λ) have less overall energy dissipation capacity, even relatively short duration records may have enough cycles to exhaust their energy dissipation capacity. In contrast, the highly ductile and stronger modern buildings can withstand greater ground motion intensities before collapse for shorter duration earthquakes, but as the duration increases, their capacity to withstand higher intensity ground motions become lesser and lesser because a larger and larger part of their energy dissipation capacity is being utilized. In contrast, past researchers have suggested that duration has a larger influence on more deteriorating systems (Amadio *et al.* 2003; Elnashai and Sarno 2008); this is likely because at moderate intensity levels the non-ductile systems will show the effects of duration while the ductile systems will not because the ground motion intensities are not near the collapse capacity of the buildings. Bommer *et al.* (2004) found that strength degradation became important at lower ground motion intensity levels under longer duration motions. Although Mahin (1980) found P-Δ to be important in an SDOF study, the level of P-Δ does not appear to as significantly influence the duration relationship, as do the cyclic deterioration and ductility capacity parameters. In particular, we note that, for longer duration ground motions, for which the ground motion intensities and displacement demands are less, there is no difference in how duration

affects collapse resistance, suggesting that P-Δ does not have a critical impact on collapse in this range.

2.7 Does Duration Matter for Collapse Risk?

It can be concluded from the previous sections that ground motion duration influences the structural collapse capacity. To quantify how important this effect is for collapse risk assessment, collapse fragility functions are created for all of the reinforced concrete building models, and four are plotted in Figure 2.13. These fragility functions describe the probability of collapse as a function of the ground motion intensity *(S_{di})*, assuming a lognormal probability distribution[1]. For simplicity of illustration, the ground motion records are divided into two groups: *Short* duration records (*5-95% D_s*: 0-35 s, Median D_s = 13s) and *Long* duration records (*5-95% D_s* >35 s, Median D_s = 74 s), such that there are 39 and 37 records, respectively, in each group. For comparison, these fragility curves are compared to a typical "duration-blind" fragility curve, obtained using the general set of ground motions from FEMA P695 (FEMA 2009). The fragility curve parameters for all buildings subjected to the *Short* and *Long* and FEMA P695 (FEMA 2009) ground motions are provided in Table 2.3. The median collapse capacity (denoted x_M in Table 2.3) quantifies the S_{di} level at which the probability of collapse is 0.50 for each building model.

[1] The Chi-square goodness-of-fit test conducted at the 5% significance level indicates that the lognormal distribution assumption is acceptable for the collapse fragility functions developed for all the buildings. The test indicated lack of fit for a few of the buildings' *Long* duration fragility curves, due to the wide variability of response predictions associated with records with very different duration. Since the test indicated acceptability of the lognormal assumption for more than 75% of the buildings subjected to the long duration set, the assumption is taken as valid.

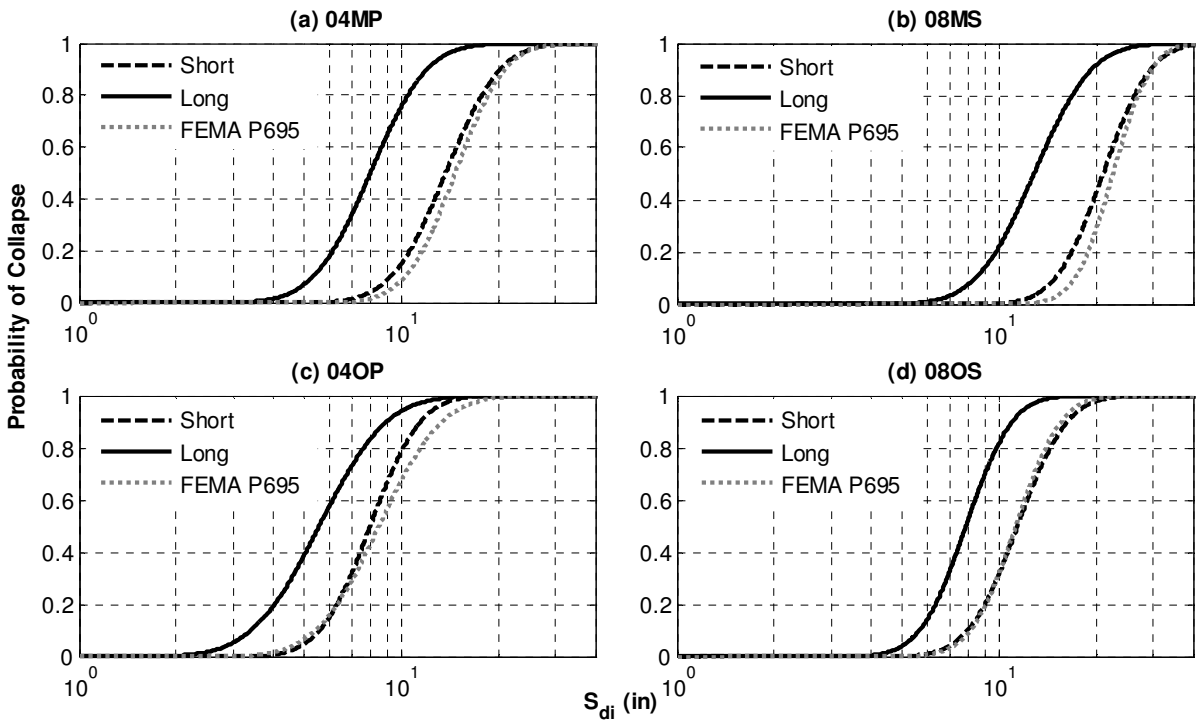

Figure 2.13 Collapse fragility functions for *Short* duration, *Long* duration and FEMA P695 (FEMA 2009) far field records for (a) Modern 4 Story building, (b) Modern 8 story building, (c) Older 4 story building, and (d) Older 8 story building.

Table 2.3 Summary of collapse fragility function parameters for all buildings subjected to *Short*, *Long* and FEMA P695 (FEMA 2009) ground motions.

ID	Short 5-95 % D_s		Long 5-95% D_s		FEMA P695		Variation in Median Capacities Compared to x_{ms}	
	x_{ms} (in)	β_s	x_{mL} (in)	β_L	x_{mF} (in)	β_F	x_{ml}	x_{mF}
02MS	11	0.36	5.9	0.48	13	0.32	-48%	16%
04MP	14	0.31	8.0	0.32	15	0.28	-42%	7%
04MS	14	0.40	6.2	0.40	15	0.33	-56%	8%
08MP	16	0.28	11	0.34	17	0.23	-33%	8%
08MS	21	0.27	13	0.32	23	0.21	-39%	7%
12MP	20	0.33	14	0.34	22	0.28	-33%	9%
12MS	22	0.30	14	0.32	24	0.25	-34%	10%
20MP	28	0.26	20	0.30	32	0.25	-30%	15%
20MS	31	0.31	19	0.34	34	0.33	-38%	11%
02OS	5.0	0.21	3.3	0.30	5.0	0.21	-33%	1%
02OP	6.4	0.31	3.6	0.28	6.6	0.26	-43%	4%
04OP	8.0	0.28	5.6	0.38	8.5	0.35	-31%	6%
04OS	10	0.28	6.8	0.23	10	0.21	-30%	0%
08OP	9	0.27	6.5	0.31	9.1	0.34	-26%	3%
08OS	11	0.28	7.9	0.26	11	0.25	-31%	-1%
12OP	13	0.45	8.7	0.27	11	0.33	-31%	-17%
12OS	13	0.27	9.2	0.25	12	0.23	-30%	-5%

For the same building, the collapse fragility curve for the *Long* records is consistently located to the left of the collapse fragility curve of *Short* duration records, indicating the increased structural fragility when buildings are subjected to longer duration ground motions. Considering results from all 17 buildings, the *Long* duration records lead to median collapse capacities that are 26 to 56% lower than *Short* duration records. The increase in predicted probability for a given ground motion level may be even more significant; for example, in Figure 2.13 (a), at $S_{di} = 9$ in the probability of collapse predicted by the *Short* duration fragility is 8% compared to 64% predicted by the *Long* duration fragility. The biggest decrease in collapse capacity between the *Short* and *Long* duration records is seen in the modern buildings; similar results were observed in the SDOF sensitivity analysis. In addition, the lognormal standard deviation of the fragility curve (denoted β) which quantifies the dispersion in the prediction, is greater for the *Long* duration fragility curve for most of the buildings, due to the larger variation in the record durations in the *Long* duration set (ranging from 35 to 271.3 s). As can be seen in Figure 2.13, the FEMA P695 (FEMA 2009) ground motions predict collapse fragilities very similar to those obtained using the *Short* duration ground motions (on average approximately a 5% difference in median collapse capacities).

The results show clearly that the longer duration records make a structure more fragile, and current risk assessment methodologies, which evaluate the collapse capacity of structure without consideration of ground motion duration, may not give a clear picture of collapse risk at sites that are more likely to experience long duration ground motions. A comprehensive risk assessment, which accounts for the probability distribution of different duration ground motions occurring at a particular site, is outside the scope of this study. Nonetheless, to explore the effects of duration on risk, we note that a number of researchers have proposed empirical

predictions for duration of ground motion at a site, as a function of earthquake magnitude, site-to-source distance, and other parameters (Abrahamson and Silva 1996; Bommer *et al.* 2004; Kempton and Stewart 2006), and apply these relationships to compare predicted durations at a Seattle site and a San Francisco site. The earthquake scenarios contributing most to the hazard of having a 2% in 50 year ground motion event at a rock site in Seattle and San Francisco are obtained from seismic deaggregation of probabilistic seismic hazard analysis by USGS (2012a). The deaggregation generated the most important earthquake scenarios for the selected hazard level as a M_w 7.74 earthquake with closest distance ($R_{closest}$) of 12.5 km for the San Francisco site and a M_w 9.02 earthquake with $R_{closest}$ = 109 km for the Seattle site. Using the relationship proposed by Abrahamson and Silva (1996), the expected ground motion durations from these earthquakes are about 27s and 95s for the San Francisco and Seattle rock sites, respectively. For a ductile concrete building having a period of 1s, this difference in ground shaking durations corresponds to 40% reduction in median collapse resistance.

This illustrative calculation of collapse risk in Seattle and San Francisco is based on one of the important earthquake scenarios only at each site and examines the effect of duration, all else being equal. In a complete probabilistic seismic hazard analysis of the collapse risk of a particular building at a particular site, it is necessary to consider all possible earthquake scenarios which could affect a site, as well as the distribution of ground motion intensities and durations associated with those events. To do so, more data are needed to improve the ground motion duration prediction equations. Since the existing relationships have been mostly developed using a limited ground motion database consisting of shallow crustal events with moderate magnitudes and distances up to 200 km, they may not be suitable for predicting expected duration for subduction earthquakes and other larger magnitude events (especially those dominating the

hazard in Seattle). In addition, most ground motion prediction equations for intensity predict $Sa(T_1)$ not S_{di}, although, in future, more attenuation relationship for S_{di} may be developed (*e.g* (Tothong and Cornell 2006)). A better understanding of the probability distribution of ground motion intensities and durations at a site, combined with the fragility curves in Figure 2.13, is needed to obtain robust estimates of the collapse risk of structures at a site due to possible occurrence of a long or short duration ground motions.

2.8 Conclusions

Based on the results described above, we conclude that ground motion duration plays a significant role in the collapse resistance of a structure. The consistent trend observed across all the buildings is that the collapse capacity of a particular structure, quantified by the ground motion intensity at which collapse occurs, decreases as the duration of the record increases. As a consequence, when we consider two ground motions with the same intensity, the longer duration record proves more damaging for the structure than shorter duration record because the longer duration ground motion imposes higher energy demands on the structure. Even so, duration does not have much influence on the maximum drift responses of the structure. These results suggest that a vector of ground motion parameters that reflect ground motion intensity, frequency content and duration can provide better predictions of earthquake-induced collapse than an assessment that neglects duration; in this study, the ground motion intensity parameter S_{di} represented both intensity and frequency content. The significance of ground motion duration for collapse capacity depends on the ductility capacity and energy dissipation characteristics of the structure, as well as the intensity of ground motions expected at a particular site.

Current methods of building design and assessment do not typically consider the effect of ground motion duration. The vast majority of buildings are designed according to static methods

based on a code-defined design spectrum. In rare cases, nonlinear time history analyses are used in design, but it is not required by most codes to consider duration of records in ground motion selection procedures. However, these results indicate that longer duration ground motions make a structure more fragile and therefore, if we apply "duration blind" analyses at sites where long duration ground motions can be expected, we may be underestimating the risk of collapse of the structure.

The influence of duration on structural collapse informs the procedure generally adopted to select ground motions for nonlinear analysis of structures. Matching response spectra of the selected ground motions with the target design spectra or conditional mean spectra explicitly accounts for the intensity and frequency content of expected ground motions, but not duration. The ground motion duration is implicitly considered by matching parameters like magnitude, distance to site etc. for selected ground motions with hazard deaggregation, but it does not guarantee that the influence of expected duration on structural will be completely captured with the ground motion set so selected. Thus, our findings support recommendations by (Bradley 2011; Katsanos *et al.* 2010; Malhotra 2003) justifying ground motion duration as one of the parameters to consider in ground motion selection.

More research is needed before comprehensive risk assessments can be conducted that accounts for ground motion duration in the framework of performance-based earthquake engineering. First, probabilistic seismic hazard analyses that represent the joint probability of occurrence of ground motion intensity and duration at a particular site are needed. Longer duration ground motions tend to be less intense, but this depends on the site seismicity; duration is positively correlated with site-to-source distance and earthquake magnitude, but ground motion intensity is inversely correlated with distance. This effort is complicated by the wide

variation in ground motion duration predictions, even for a given set of earthquake properties, and by differences in ground motion frequency content between long and short duration ground motions. More investigation of the relationship between the earthquake source (*i.e*. interface vs. intraslab vs. crustal) and duration prediction is also needed. In addition, although this study examined a wide number of buildings with varying properties, different types of structures with different approaches to modeling cyclic deterioration and different failure mechanisms (*e.g*. shear critical columns) should also be examined to verify that results can be further extrapolated to other types of structures.

Appendix 2.A: Ground Motion Database

Table 2.4 Ground motion database.

Year	Earthquake	M[e](M$_w$)	Epi. Dis.(km)	Type	Station or ID	Soil[g]	PGA (g)	5-95% D$_s$(s)
1980[a]	Mammoth Lakes	4.8	1.1	Crustal	NGA0264	D	0.53	1.1
1935[a]	Helena, Montana	6	6.3	Crustal	NGA0001	C	0.15	2.3
1980[a]	Mammoth Lakes	5.7	2.8	Crustal	NGA0240	D	0.43	3.5
1976[a]	Friuli, Italy	6.5	20.2	Crustal	NGA0125	C	0.35	4.2
1976[a]	Friuli, Italy	6.5	20.2	Crustal	NGA0125	C	0.30	4.9
1994[a]	Northridge	6.7	26.5	Crustal	NGA0960	D	0.48	5.6
1989[a]	Loma Prieta	6.9	31.4	Crustal	NGA0767	D	0.54	6.4
1989[a]	Loma Prieta	6.9	94	Crustal	NGA0783	D	0.27	7
1994[a]	Northridge	6.7	16.3	Crustal	NGA0952	C	0.39	7.6
1992[a]	Landers	7.3	82.1	Crustal	NGA0848	D	0.31	8.2
1999[a]	Duzce, Turkey	7.1	41.3	Crustal	NGA1602	D	0.73	8.5
1994[a]	Northridge	6.7	13.4	Crustal	NGA0953	D	0.42	9.2
1979[a]	Imperial Valley	6.5	12.4	Crustal	NGA0189	D	0.29	10
1999[a]	Kocaeli, Turkey	7.5	98.2	Crustal	NGA1158	D	0.33	10.6
1979[a]	Imperial Valley	6.5	17.7	Crustal	NGA0162	D	0.27	11
1994[a]	Northridge	6.7	25.5	Crustal	NGA1003	D	0.47	11.5
1995[a]	Kobe, Japan	6.9	24.2	Crustal	NGA1107	D	0.34	12.9
1987[a]	Superstition Hills	6.5	11.2	Crustal	NGA0725	D	0.45	13.8
1979[a]	Imperial Valley	6.5	17.6	Crustal	NGA0162	D	0.17	14.6
1992[a]	Cape Mendocino	7	22.6	Crustal	NGA0829	D	0.24	15.3
1987[a]	Superstition Hills	6.5	35.8	Crustal	NGA0721	D	0.36	16
1989[a]	Loma Prieta	6.9	48.2	Crustal	NGA0776	C	0.37	16.4
1989[a]	Loma Prieta	6.9	47.9	Crustal	NGA0777	D	0.25	17.4
1992[a]	Landers	7.3	86	Crustal	NGA0900	D	0.15	18.9
1987[a]	Superstition Hills	6.5	19.5	Crustal	NGA0728	D	0.16	19.6
1986[a]	Taiwan SMART	7.3	77.6	Subduction	NGA0578	D	0.24	20.3
1986[a]	Hollister	5.4	14.8	Crustal	NGA0498	D	0.10	21.2
1985[b]	Valparaiso	7.8	85.7	Subduction	Melipilla	A/B	0.53	22.4
1999[a]	Chi-Chi, Taiwan	7.6	40.5	Crustal	NGA1182	C	0.30	24.3
1990[a]	Manjil, Iran	7.4	84	Crustal	NGA1636	D	0.13	25.7
1992[a]	Landers	7.3	13.7	Crustal	NGA0864	C	0.28	26.1
1992[a]	Landers	7.3	13.7	Crustal	NGA0864	C	0.27	27.2
1999[a]	Hector Mine	7.1	48	Crustal	NGA1762	D	0.18	27.5
1999[a]	Chi-Chi, Taiwan	7.6	32	Crustal	NGA1595	D	0.33	28.3
1990[a]	Manjil, Iran	7.3	40.4	Crustal	NGA1633	C	0.51	28.9
1992[a]	Landers	7.3	27.3	Crustal	NGA0850	D	0.17	31.8
1992[a]	Landers	7.3	21.3	Crustal	NGA0881	D	0.13	32.1
1985[b]	Valparaiso	7.8	115	Subduction	San Felipe, Chile	D/E	0.43	33.7
1999[a]	Chi-Chi, Taiwan	7.6	28.4	Crustal	NGA1536	D	0.18	34.6
1979[a]	St Elias, Alaska	7.5	74.8	Crustal	NGA1628	D	0.09	35.5
1992[a]	Landers	7.3	32.3	Crustal	NGA0882	D	0.11	36.3
1992[a]	Landers	7.3	32.3	Crustal	NGA0882	D	0.10	37
1999[a]	Chi-Chi, Taiwan	7.6	33.8	Crustal	NGA1547	D	0.12	38.7

Year	Earthquake	M[e](M$_w$)	Epi. Dis.(km)	Type	Station or ID	Soil[g]	PGA (g)	5-95% D$_s$(s)
2002[a]	CA/Baja Border	5.3	42.2	Crustal	NGA2003	D	0.04	39.9
1985[b]	Valparaiso	7.8	74.3	Subduction	Zapallar	A/B	0.31	40.4
1985[b]	Valparaiso	7.8	~ 65	Subduction	San Isidro	[f]	0.68	42.6
2002[a]	CA/Baja Border	5.3	42.2	Crustal	NGA2003	D	0.08	43.6
1999[a]	Chi-Chi, Taiwan	7.6	41.4	Crustal	NGA1246	D	0.19	45.9
1985[b]	Valparaiso	7.8	25.4	Subduction	el Almendral	[f]	0.30	48.4
1985[b]	Valparaiso	7.8	25.4	Subduction	el Almendral	[f]	0.16	49.9
2007[c]	KM, Indonesia	7.9	164.6	Subduction	West Sumatra	[f]	0.13	50.3
1979[a]	Imperial Valley	6.5	33.7	Crustal	NGA0169	D	0.35	50.3
1979[a]	Imperial Valley	6.5	33.7	Crustal	NGA0169	D	0.22	51
2007[c]	KM, Indonesia	7.9	164.6	Subduction	West Sumatra	[f]	0.09	52.9
1985[b]	Valparaiso	7.9	25.3	Subduction	Ventanas	[f]	0.20	55.9
1985[b]	Valparaiso	7.9	25.3	Subduction	Ventanas	[f]	0.23	56.3
1995[a]	Kobe,Japan	6.9	47.5	Crustal	NGA1113	D	0.08	58.3
1999[a]	Chi-Chi, Taiwan	7.6	69.3	Crustal	NGA1183	D	0.12	61.4
1995[a]	Kobe,Japan	6.9	47.5	Crustal	NGA1113	D	0.06	70.6
2002[a]	Denali, Alaska	7.9	189.6	Crustal	NGA2115	C	0.08	73.6
2002[a]	Denali, Alaska	7.9	189.6	Crustal	NGA2115	C	0.07	76.6
1999[a]	Chi-Chi, Taiwan	7.6	71.6	Crustal	NGA1181	D	0.10	76.9
1999[a]	Chi-Chi, Taiwan	7.6	71.6	Crustal	NGA1181	D	0.10	80.1
2002[a]	Denali, Alaska	7.9	148.1	Crustal	NGA2109	D	0.04	94.4
2002[a]	Denali, Alaska	7.9	93.4	Crustal	NGA2113	C	0.07	97.4
2002[a]	Denali, Alaska	7.9	93.4	Crustal	NGA2113	C	0.06	98.7
2002[a]	Denali, Alaska	7.9	150	Crustal	NGA2110	C	0.07	104.2
2002[a]	Denali, Alaska	7.9	296.4	Crustal	NGA2104	D	0.02	116.1
n/a[d]	Cascadia	9.2	446.8	Subduction	Seattle	B/C	0.16	132.3
n/a[d]	Cascadia	9.2	446.8	Subduction	Seattle	B/C	0.13	137.2
n/a[d]	Cascadia	9.2	481.3	Subduction	Seattle	B/C	0.05	162.2
n/a[d]	Cascadia	9.2	481.3	Subduction	Seattle	D/E	0.13	188
n/a[d]	Cascadia	9.2	446.8	Subduction	Seattle	D/E	0.16	196.7
n/a[d]	Cascadia	9.2	481.3	Subduction	Seattle	D/E	0.14	206
n/a[d]	Cascadia	9.2	446.8	Subduction	Seattle	D/E	0.18	230.1
n/a[d]	Cascadia	9.2	481.3	Subduction	Seattle	B/C	0.04	271.3

[a] Database: PEER Next Generation Attenuation (NGA) database (PEER 2012).
[b] Database: COSMOS Virtual Data Center (COSMOS 2011).
[c] Database: USGS National Strong-Motion Project (USGS 2012b).
[d] Database: Simulated Ground Motions - Caltech Virtual Shaker (Caltech 2011; Yang 2009).
[e] Earthquake Magnitude.
[f] Data not available.
[g] NEHRP Soil Classification (ASCE 2010).

CHAPTER 3 COLLAPSE RISK OF BUILDINGS IN THE PACIFIC NORTHWEST REGION DUE TO SUBDUCTION EARTHQUAKES

3.1 Background and Motivation

Recent seismic events in Sumatra, Indonesia (M_w 9.1, 2004), Tohoku, Japan (M_w 9.0, 2011), and Maule, Chile (M_w 8.8, 2010) are some of the largest earthquakes ever recorded (USGS 2012a). These events are classified as subduction earthquakes, which occur when an oceanic tectonic plate subducts beneath a continental plate. These earthquakes occur due to rupture at the interface of the two plates or deep within the subducting plate. In the Cascadia subduction zone in the Pacific Northwest region of the U.S. and Canada, the Juan de Fuca, Explorer and Gorda Plates are subducting beneath the North American Plate (Figure 3.1 (a)).

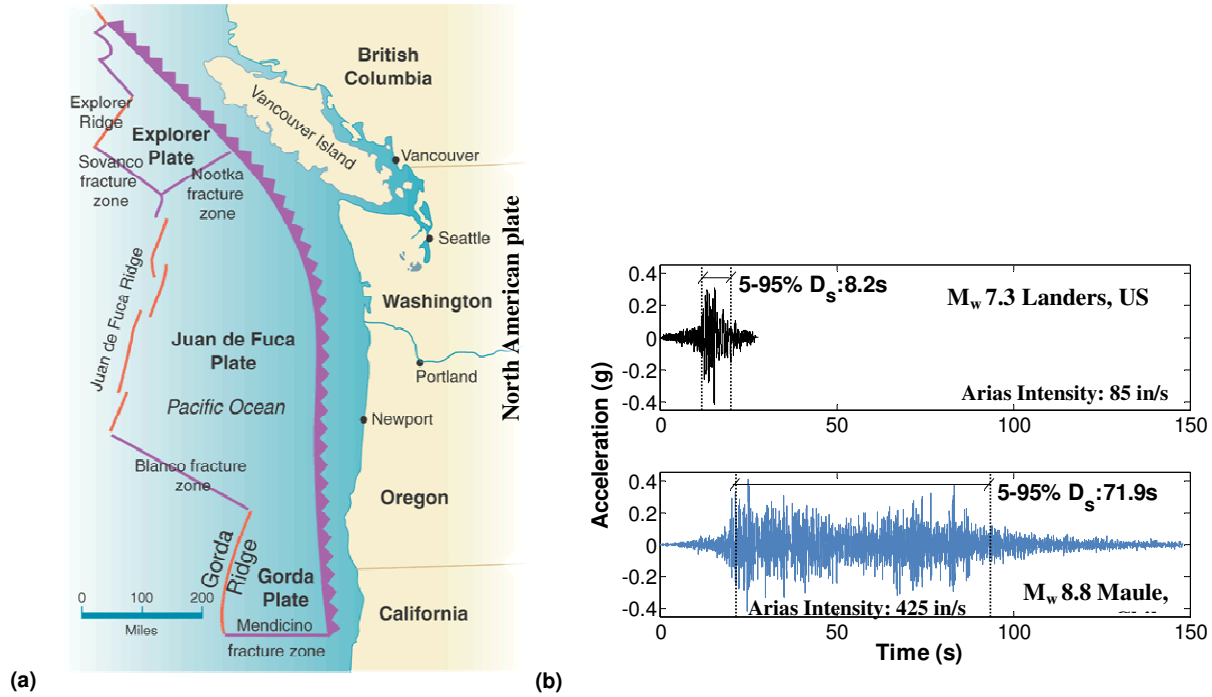

Figure 3.1 (a) Subduction fault zone along the Pacific Northwest coast (from (Thatcher 2001)). (b) Ground motion time history for Landers, US crustal earthquake (Station: NGA848) and Maule, Chile subduction earthquake (Station: Talca) having the same PGA, but different durations (ground motion data from CESMD 2012; PEER 2012).

In the last 3500 years, at least seven large subduction earthquakes (M_w>9) have taken place in the Cascadia subduction zone. These events have an estimated return period of 400 to

600 years, and the latest one occurred in January, 1700 (Pacific Northwest Seismic Network 2012; USGS 2012a). On this basis, seismologists expect a similar subduction earthquake to occur in the future. Such an event could potentially endanger life, structures and infrastructure in the cities of Portland, Oregon (metro area population ~2.3 million), Seattle, Washington (3.9 million), Vancouver, British Columbia (2.3 million) and other regions exposed to Cascadia subduction hazard in the Pacific Northwest (Government of Canada 2001; US Census 2012).

Ground motions from subduction earthquakes are generally longer in duration, and have more load reversal cycles and have higher energy associated with longer periods as compared to ground motions from more frequently recorded shallow crustal events. Figure 3.1 (b) shows the ground motion time histories from a crustal (Landers, U.S., M_w 7.3, 1993) and a subduction (Maule, Chile, M_w 8.8, 2010) earthquake with the same peak ground acceleration (PGA) of 0.42g. The subduction ground motion has substantially longer duration. Here, duration is quantified as the 5-95% significant duration, *5-95% D_s*, which is calculated as the time between which 5 to 95% of the energy of the accelerogram (quantified by the Arias Intensity) is accumulated (Bommer and Martínez-Pereira 1999). Figure 3.1(b) also demonstrates that the longer duration subduction motion results in a larger number of load reversal cycles. Regarding ground motion frequency content, Tremblay (1998) found that the response spectra of ground motions from subduction earthquakes have higher spectral intensities as compared to crustal earthquakes for building periods between 1-2s for sites located at moderate distances (20-70km) from the fault. Subduction ground motion intensities also attenuate at a slower rate than crustal ground motions with distance from the rupture under certain conditions. Specifically, Youngs *et al.* (1997) found that for a same magnitude event, ground motion prediction equations indicate higher intensity ground motions for subduction earthquakes than crustal earthquakes for

distances greater than 50km; the opposite is true for sites closer than 50km to the rupture. The rate of attenuation of the ground motion also depends on the mechanism of subduction earthquake: *interface* (occurring at the interface of overriding and subducting plates) or *inslab* (occurring within the subducting plate). Interface events, *e.g.* Maule, Chile (M_w 8.8, 2010), have flatter rates of seismic attenuation with distance as compared to inslab events, *e.g.* Nisqually, Washington, U.S. (M_w 6.8, 2001). Therefore, *interface* events can result in damaging levels of ground shaking over a larger area(Atkinson and Boore 2003).

The longer duration, greater long-period energy content and larger number of load reversal cycles associated with ground shaking from subduction earthquakes can affect structural response differently than ground motions from crustal earthquakes. In the Michoacan (Mexico City) subduction earthquake (M_w 8.2, 1985), around 20% of the 6-15 story buildings located in the region of greatest damage were damaged or collapsed; this damage was attributed to substantial long period spectral content in the ground motions (Beck and Hall 1986). Yang (2009) also illustrated the susceptibility of structures to subduction ground motions, showing that nonlinear dynamic analysis of 6 and 20 story steel moment frames employing slightly scaled recorded ground motions from the Tokachi Oki, Japan subduction earthquake (M_w 8.3, 2003) will result in collapse of the buildings. White and Ventura (2004) conducted nonlinear dynamic analysis on a 30 story residential building in Vancouver, Canada using crustal and subduction ground motions, finding that the structural response was more influenced by higher mode effects in the case of subduction ground motions as compared to crustal ground motions. The duration of the ground motions, combined with a large number of load reversal cycles, has also been shown to result in reduced structural collapse capacity. Raghunandan and Liel (2013) (Chapter 2 of the dissertation) conducted nonlinear dynamic analysis of 17 reinforced concrete ductile and non-

ductile moment frames and found a significant decrease in collapse capacity on being subjected to longer duration ground motions as compared to a shorter duration motions. The higher energy dissipation demands from the longer duration earthquakes causes more damage accumulation as compared to a shorter duration earthquake of the same intensity (Foschaar *et al.* 2012; Hancock and Bommer 2006; Raghunandan and Liel 2013). Mahsuli and Haukaas (2013) employed first order and second order reliability methods for analyzing the seismic risk in Vancouver metropolitan region and found that among different sources of seismicity in the region, earthquakes from subduction sources have the highest probability of seismic losses exceeding $100 billion (the seismic hazard at site is not included). Taken together, these studies indicate that structural response differs for crustal and subduction earthquakes, due to unique characteristics of subduction ground motion duration and frequency content.

Nevertheless, the influence of the variation in ground motion properties between crustal and subduction earthquake on probabilistic metrics of building performance and safety is uncertain. Recent studies (*e.g.* FEMA 2009; Haselton *et al.* 2011; Liel *et al.* 2011; Krishnan and Muto 2008) have quantified the collapse risk of modern code-conforming structures in California subjected to crustal motions. In fact, new risk-targeted seismic hazard maps in current building codes and standards ASCE 7 (ASCE 2010) and International Building Code (ICC 2012) define spectral values for building design (MCE_R) that are assumed to provide a uniform collapse risk of 1% in 50 years across the US (Luco *et al.* 2007). However, the true collapse risk of structures designed according to these codes in Pacific Northwest is not clear due to the different features of ground shaking and few studies quantifying structural performance on exposure to subduction ground motions. It is also not clear how older buildings with known deficiencies, such as non-

ductile concrete structures (Liel and Deierlein 2012), will perform under subduction ground shaking.

Buildings in the Pacific Northwest region are potentially at risk of earthquakes from crustal (*e.g.* Seattle fault) and subduction (Cascadia subduction zone) events. This paper assesses the risk of seismic building collapse in the Pacific Northwest, accounting for the unique characteristics of subduction ground motions. For this purpose, 36 concrete moment frame buildings are designed according to outdated and modern building codes for Portland and Seattle. The outdated codes considered are the 1967, 1973, 1994 Uniform Building Codes (ICBO 1967; ICBO 1993; ICBO 1994). The 2012 International Building Code is the current code (ICC 2012). These designs are used to generate nonlinear simulation models in *OpenSees* (2012) that capture key failure modes of non-ductile and ductile concrete frames to the point of structural collapse. Incremental dynamic analysis is carried out on these building models using two ground motion sets: a crustal ground motion set and a subduction ground motion set. Dynamic simulation results are summarized in the form of collapse fragility curves calculated for each set of ground motions, which represent the probability of collapse conditioned on ground motion intensity. In this study, separate building collapse fragility curves are created and compared for the crustal and subduction sets of ground motions. These fragility curves are integrated with the seismic hazard information for sites in Portland and Seattle to predict the risk of earthquake-induced collapse. The contribution of crustal and subduction earthquakes to the total collapse risk is computed by employing deaggregated hazard curves for crustal and subduction events at each site and convolving hazard curves with the respective building fragility curve. In order to assess the performance of the buildings at the sites considered in the study, the collapse risk of the

buildings is compared with the uniform collapse risk goal expressed in 2012 IBC of 1% probability of collapse in 50 years.

3.2 Ground Motion Database

In order to quantify the collapse capacities of buildings subjected to crustal and subduction ground motions, a ground motion database is compiled with both categories of motions. The *"Crustal"* set consists of 35 far-field crustal earthquake ground motions selected from the set of 44 ground motions used in FEMA P-695 (FEMA 2009). These records are from large magnitude shallow crustal earthquakes (M_w 6.5-7.6), recorded at moderate distances from the rupture (7-26 km) with $PGA > 0.15$g. The *"Subduction"* set consists of 42 ground motions from subduction events (M_w 6.8-9.0), collected from a number of different databases (CESMD 2012; K-NET 2012; NOAA 2012; PEER 2012; USGS 2012b). This set includes recordings from the recent Tohuku, Japan (M_w 9.0, 2011) and Maule, Chile (M_w 8.8, 2010) events, along with recordings from subduction earthquakes in Alaska and Washington states, as well as Chile, El Salvador, Indonesia, Japan, and Mexico. These ground motions have $PGA > 0.01$g and are recorded at larger distances from the rupture (27-392 km). The K-NET (2012) Japanese earthquake recordings were baseline corrected (zeroth order) and filtered with a 4^{th} order Butterworth filter (0.2Hz - 25Hz) using the software SeismoSignal (Boore and Bommer 2005; SeismoSoft 2012). The remainder of the recordings were obtained directly from the databases in a processed form, *i.e.* already baseline corrected and filtered. There are not many recordings available from large magnitude subduction earthquakes due to the rarity of their occurrence. Therefore, a third *"Simulated"* set comprised of 30 simulated ground motions from subduction earthquakes with M_w>8.5 is also compiled (Atkinson and Macias 2009; Mavroeidis *et al.* 2008; Sørensen *et al.* 2007; Yang 2009). The *Simulated* set may also be used to evaluate the

effectiveness of simulated subduction motions in capturing the structural response in comparison to structural response from recorded subduction motions. The ground motion information for all the three sets is provided in Appendix 3.A. In all three sets, most of the ground motions are recorded on rock or stiff soil sites. Since previous research has indicated that long period pulse records in near-fault sites can significantly reduce the collapse capacity of a structure (Champion and Liel 2012), near site effects are avoided by excluding ground motions with large pulses in velocity time history. These pulses are identified through the procedure developed by Baker (2007).

Figure 3.2(a) summarizes the characteristics of the ground motion recordings and earthquakes included in the database. All of the ground motions from large magnitude events ($M_w > 8$) are from subduction earthquakes. The large magnitude of the subduction earthquakes contributes to the longer duration of the subduction ground motions in the set, because higher moment magnitude events have a larger rupture area, which requires more time to release strain energy (Kramer 1996). The relationship between magnitude and duration also explains the larger duration of ground motions in the *Simulated* set, which are based on even larger magnitude subduction earthquakes (M_w>8.5), as compared to the recorded *Subduction* set (M_w 6.8-9.0). Figure 3.2(b) shows that the subduction ground motions are recorded at large distances from the earthquake hypocenter. The geology of subduction zones is such that the rupture typically occurs far beneath the surface and at a significant distance from the built environment. As seismic waves travel, they scatter, thus increasing the separation in arrival times between different waves at distant sites (Bommer *et al.* 2009). Therefore, these larger source-to-site distances contribute to the longer duration of ground shaking in the *Subduction* and *Simulated* sets as compared to the

Crustal ground motions. The mean duration of *Crustal*, *Subduction* and *Simulated* subduction record sets are 13.9s, 44.3s and 111.8s, respectively.

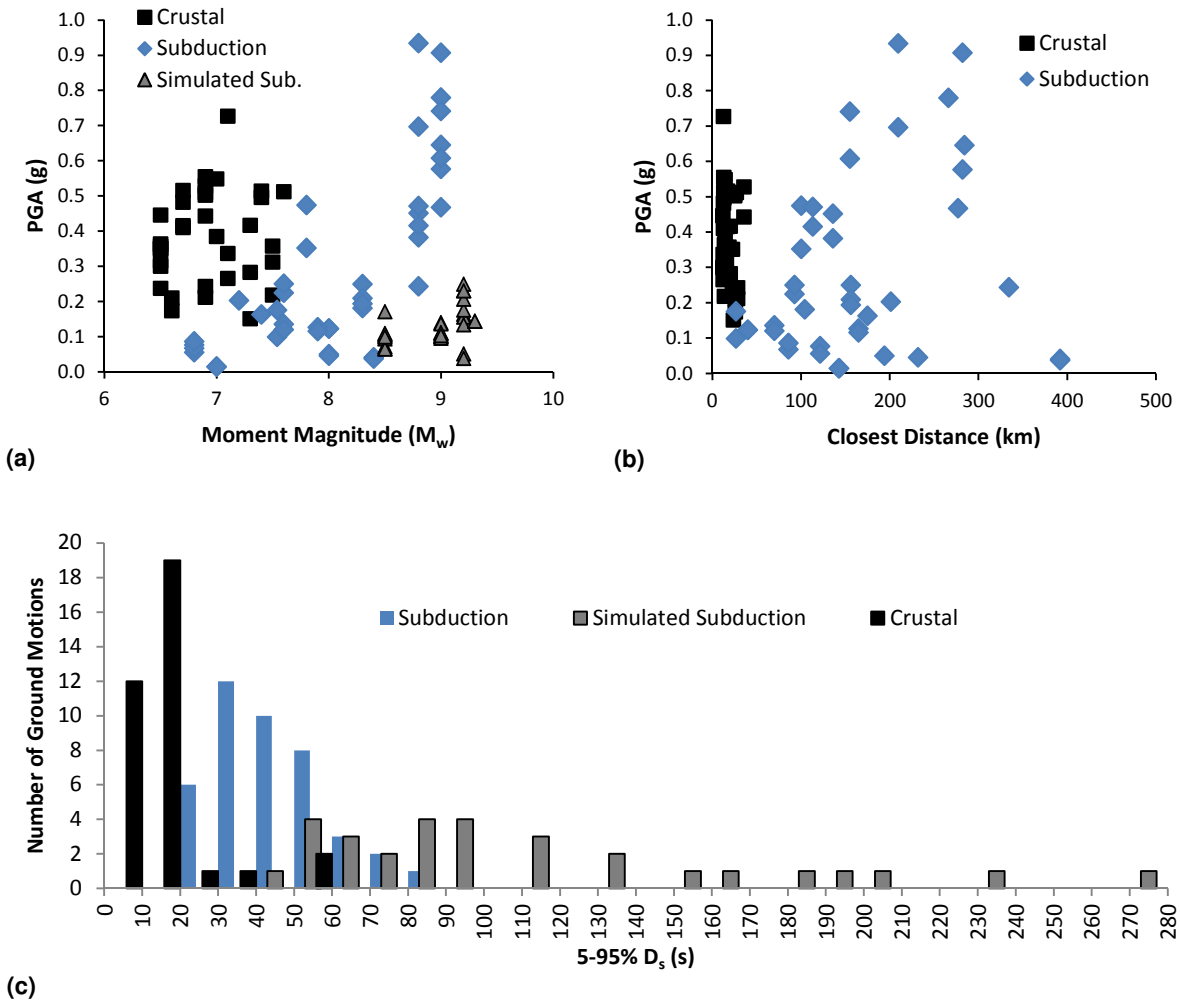

Figure 3.2. Subduction and crustal ground motion record sets, showing distribution of (a) peak ground acceleration versus earthquake magnitude, (b) peak ground acceleration versus closest distance to site and (c) 5-95% significant duration.

For the most part, the *Subduction* ground motions have relatively large *PGA* values (Figure 3.2(b)) despite being recorded at large distances from the site. This trend illustrates the slower attenuation of these waves with distance, compared to attenuation patterns for crustal events (Atkinson and Boore 2003). To examine ground motion frequency content, Figure 3.3 provides acceleration response spectra plots for all ground motions in the three different sets,

along with the mean response spectra for each set. To facilitate a comparison of ground motion frequency content, all the acceleration response spectra were scaled to 0.5g at 0.2s. The plots show that for the same short period spectral acceleration, the *Subduction* and *Simulated* subduction ground motions have a greater energy associated with longer periods as compared to the *Crustal* ground motions.

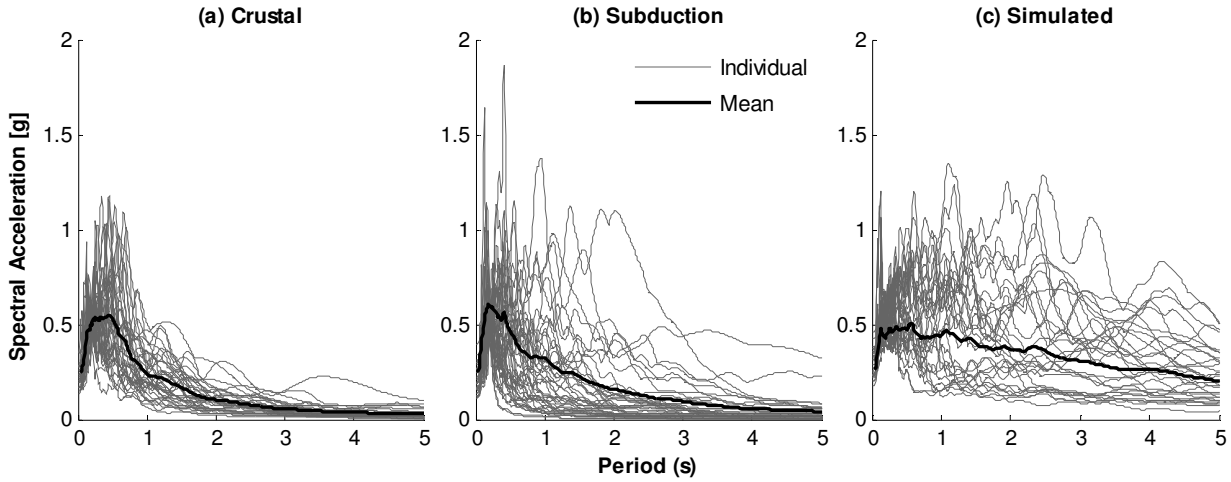

Figure 3.3. Individual ground motion response spectra (gray lines) and the mean response spectra (black line) for each set of ground motions.

3.3 Seismic Design History of the Pacific Northwest

In order to evaluate the collapse risk of existing and modern buildings in the Cascadia subduction region, it is important to understand the history of seismic design in the Pacific Northwest. The cities of Seattle, Washington and Portland, Oregon adopted municipal seismic provisions in 1946 and 1953, respectively (EERI 2005). By the 1960s or early 1970s, these local seismic provisions were replaced by statewide adoption of the Uniform Building Code (UBC). In this study, design is therefore based on the UBC and, later, the International Building Code (IBC). The rest of the paper focuses on one lateral force resisting system: concrete moment resisting frames. Reinforced concrete moment frames have been a relatively prevalent type

construction in cities of Portland and Seattle since the 1940s (Don 2007; EERI 2005), making them a suitable choice of structural system for studying the collapse risk of the buildings constructed in the region. All frames are space frames, meaning every frame line is assumed to resist lateral loads.

To explore the seismic design history, Figure 3.4 (b)-(d) illustrates the variation of seismic design force over the years for 2 story, 4 story and 8 story concrete buildings in Portland, Seattle and Los Angeles. (A more detailed illustration of variation of seismic design forces across different design codes from 1943 UBC to 2012 IBC is provided in Appendix 3.B). The seismic design forces are quantified in terms of design base shear coefficient, which is the ratio of the design base shear to the building weight. For the calculation of design base shear coefficient, the fundamental period is estimated based on approximate equations given in the respective building code. In this calculation, the story heights for any N-storied building are assumed to be 15ft for the first story and 13ft for the stories above. The Los Angeles design base shears are shown for comparison, since the seismic hazard in California has historically been better understood.

Figure 3.4 identifies the major changes in seismic design that have occurred over the years. In particular, it shows how the design base shear has changed to reflect improved understanding of the seismic hazard in the Pacific Northwest. In older codes, sites were divided into seismic zones representing the expected seismicity in a region, wherein sites with greater seismic hazard were located in higher seismic zones. In the early codes (prior to 1976), Seattle, like Los Angeles, was classified in the highest seismic zone (zone 3) because of its proximity to known crustal faults. In the 1976 UBC, Los Angeles was upgraded to a new, higher seismic zone 4, while Seattle remained in seismic zone 3. Due to lack of knowledge of the Cascadia

subduction hazard, Portland was assigned to seismic zone 2. The increase in design forces in Portland and Seattle in 1994 UBC resulted from inclusion of the Cascadia subduction zone earthquake hazard. Although this hazard was first acknowledged in the 1980s (Heaton and Kanamori 1984), this was its first addition to seismic design forces. The change was more dominant for Portland because the inclusion of the Cascadia subduction zone hazard upgraded the city from seismic zone 2B to seismic zone 3 whereas Seattle already fell in seismic zone 3 due to its proximity to crustal faults. With the adoption of the 2000 IBC, the seismic zonation concept was replaced with maps based on probabilistic seismic hazard analysis for every site of interest based on its geographic location (McGuire 2004). This probabilistic seismic hazard analysis includes both crustal and subduction earthquake sources.

Another major change in seismic design was the implementation of the requirements for ductile detailing of reinforced concrete. Detailing requirements were instituted in the early 1970s in response to the poor performance of non-ductile concrete buildings in the 1971 San Fernando earthquake, as well as other seismic events (Moehle 1998). The 1973 UBC was the first building code to require ductile moment frames for RC frame structures. Prior to 1973, ductile moment frames were required only for concrete or steel frame buildings taller than 160 feet in height. In 1973, it became mandatory for concrete space frames part of the lateral load resisting system to be ductile moment resisting, if in seismic zones 2 or 3. This change is shown in Figure 3.4 by the left-most vertical dashed line, which demarcates two groups of existing buildings: (1) non-ductile frames susceptible to brittle shear failure constructed prior to 1973 and (2) ductile frames with more transverse reinforcement and higher deformation capacity constructed post 1973. Compared to the 1967 UBC buildings, the ductile 1973 UBC frames are designed for the same level of expected seismicity, but the 1973 design forces are multiplied by 0.67 because the code

allows for reduction of design forces due to increased deformation capacity of ductile moment resisting structural frames.

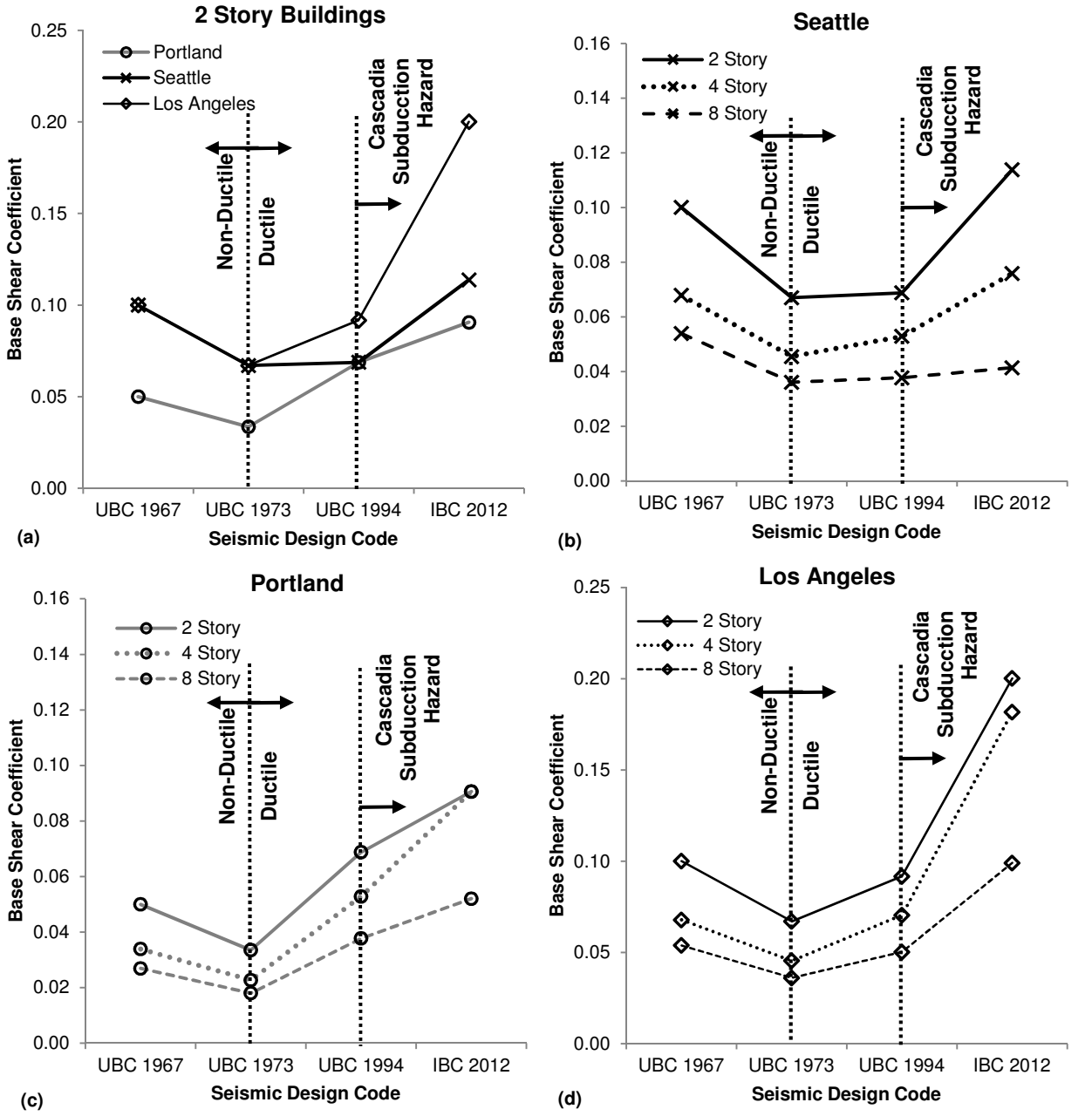

Figure 3.4. History of seismic design base shear coefficient (V_{design}/W) for (a) 2 story buildings in Seattle, Portland and Los Angeles, and buildings of varying height in (b) Seattle, (c) Portland, and (d) Los Angeles. The figure is annotated to show the significant changes in design and detailing occurring around 1973 and 1994. All buildings are assumed to be in site class D (stiff soils).

Although the changes in ductile detailing requirement are not directly shown in the design base shear coefficient values in Figure 3.4, the ductile moment frames also required more closely spaced transverse reinforcement (~4-5in), compared to non-ductile moment frames that had much wider transverse reinforcement spacing (~12-16in). The concept of ductile detailing requirements has remained since 1973, although the specifics have evolved over time.

3.4 Archetype Building Designs and Nonlinear Simulation Models

Table 3.1 Seismic design parameters for the archetypical buildings designed for each city and era.

Design Code	Portland		Seattle		Los Angeles	
	Design Force[1]	Design Detailing[2]	Design Force[1]	Design Detailing[2]	Design Force[1]	Design Detailing[2]
1967 UBC	Zone 2	NDMRF	Zone 3	NDMRF	Zone 3	NDMF
1973 UBC	Zone 2	DMRF	Zone 3	DMRF	Zone 3	DMRF
1994 UBC	Zone 3	SMRF-1	Zone 3	SMRF-1	Zone 4	SMRF-1
2012 IBC	S_s=0.98 g S_1=0.42 g	SMRF-2	S_s=1.37g S_1=0.53g	SMRF-2	S_s=2.40 g S_1=0.84 g	SMRF-2

[1] Provides information about the seismic hazard used in determining the required design base shear. The information is provided in terms of seismic zones for the 1967, 1973 and 1994 building groups. For the modern buildings, the seismic hazard is reported in terms of the risk-targeted Maximum Considered Earthquake (MCE_R) ground motion response acceleration value at T=0.2 s (S_s) and T=1 s (S_1) from the 2012 IBC.
[2] Design detailing provides information about the seismic detailing criteria for buildings designed. Details about these designations are provided in the text.

To assess the collapse risk of structures in the Pacific Northwest, 2, 4 and 8 story reinforced concrete buildings are designed according to four different design codes for Pacific Northwest sites in Seattle (47.6°N, 122.3°W) and Portland (45.5°N, 122.65°W). The site coordinates represent a central location in each city susceptible to high intensity shaking. Based on the observed seismic history, the authors elected to design buildings according to (1) the 1967 UBC, (2) the 1973 UBC, (3) the 1994 UBC and (4) current building codes (2012 IBC- equivalent to ASCE 7 (ASCE 2010), ACI 318 (ACI 2008)) to mark the major changes in seismic design and detailing requirements for concrete moment frames. Buildings are also designed for Los Angeles (34.05°N, 118.25°W) to compare the structural response of buildings in Portland and Seattle to buildings in a high seismic region susceptible to only crustal earthquakes.

Table 3.2 Archetype building design information.

Site	Stories	Design Base Shear Coefficient[1]	T_1[2]	μ[3]	Ω[4]
1967 UBC					
Seattle	2	0.100	0.70	4.0	2.9
	4	0.068	1.11	3.5	2.9
	8	0.054	2.02	3.0	1.7
Portland	2	0.050	0.70	4.3	5.8
	4	0.034	1.29	2.9	4.3
	8	0.027	2.30	2.9	2.8
Los Angeles	2	0.100	0.70	4.0	2.9
	4	0.068	1.11	3.5	2.9
	8	0.054	2.02	3.0	1.7
1973 UBC					
Seattle	2	0.067	0.65	13.0	5.6
	4	0.045	1.07	8.9	4.2
	8	0.036	1.88	6.2	2.9
Portland	2	0.033	0.65	14.95	10.7
	4	0.023	1.21	7.5	7.0
	8	0.018	2.17	7.8	4.5
Los Angeles	2	0.067	0.65	13.0	6.0
	4	0.045	1.07	8.9	4.2
	8	0.036	1.88	6.2	2.9
1994 UBC					
Seattle	2	0.069	0.6	14.7	5.9
	4	0.053	0.99	10.7	4.3
	8	0.038	1.79	7.8	3.1
Portland	2	0.069	0.6	14.7	5.9
	4	0.053	0.99	10.7	4.3
	8	0.038	1.79	7.8	3.1
Los Angeles	2	0.092	0.56	15.8	5.1
	4	0.07	0.95	10.7	3.5
	8	0.05	1.64	8.8	2.7
2012 IBC					
Seattle	2	0.114	0.58	14.5	3.9
	4	0.081	1	11.3	2.7
	8	0.044	1.8	9.5	2.3
Portland	2	0.091	0.63	14	4.2
	4	0.068	1	12.4	3.1
	8	0.037	1.98	7.8	2.5
Los Angeles	2	0.200	0.54	13.6	2.7
	4	0.130	0.86	12.8	2.4
	8	0.071	1.57	9.6	2

[1] Ratio of the design base shear to the building weight (V_{design}/W).
[2] First-mode elastic (fundamental) structural period based on eigenvalue analysis, considering cracked concrete sections. These values are larger than the initial period values estimated by Chopra and Goel (2000). However, collapse results are not sensitive to initial period of the building (Ibarra and Krawinkler 2003).
[3] Ductility capacity as determined by nonlinear static pushover analysis. It is computed as the ratio of ultimate displacement to the effective yield displacement calculated from the nonlinear pushover analysis of the building (FEMA 2009).
[4] Overstrength: Calculated as the ratio of maximum base shear of the building from nonlinear static pushover analysis to the ratio of design base shear.

The seismic design parameters for the three cities and four design codes are summarized in Table 3.1, and the properties of the resulting building designs are provided in Table 3.2.

Buildings are designed for gravity and earthquake loads and wind loads are assumed to not govern the design.

The buildings can be grouped into two major categories according to their deformation capacity. The non-ductile buildings designed according to 1967 UBC for Seattle, Portland and Los Angeles represents the older buildings that have inadequate deformation capacity due to poor reinforcement and detailing. These limitations do not allow them to deform inelastically and dissipate energy making them susceptible to brittle shear and axial failure; these buildings are indicated as NDMRF in Table 3.1. All the buildings designed in 1973 or later are subject to mandatory ductile reinforcement detailing and capacity design requirements, although the specific requirements vary depending on the design era of interest. The main difference between the ductile moment resisting frame (DMRF), and the special moment resisting frames (SMRF) is the strong column-weak beam requirement, which prevents or delays the formation of story mechanisms. Specifically, the DMRF has columns that are at least as strong as beams, whereas the SMRF requires columns that are at least 20% stronger than beams. The most recent (2012 IBC and 1994 UBC) designs require the concrete lateral load resisting system to be special moment resisting frames (SMRF) in high seismic zones. SMRF design is controlled by strong column-weak beam requirements, capacity design provisions preventing column shear failure, reinforcement detailing requirements for transverse reinforcement, lap splices and other features, and story drift limits. There are, however, minor differences in transverse reinforcement spacing requirements in buildings designed according to the 1994 UBC (denoted SMRF-1) and those those designed according to modern codes (SMRF-2). SMRF-1 also has a more stringent story drift requirement of (~1.3%), which governs the design of the taller buildings, as compared to

(~2 %) drift requirement for SMRF-2 buildings.[2] These factors results in slightly greater strength of the 1994 UBC buildings (indicated by the Ω in Table 3.2) as compared to the 2012 IBC buildings designed for similar base shear coefficients. The absence of capacity design and detailing regulations explains the lower strengths (Ω) and ductilities (μ) observed in the 1967 and 1973 buildings. According to USGS (2012), most of the sites in the central areas of Portland and Seattle have NEHRP site class C (*i.e.*, very dense soil and soft rock) or site class D (*i.e.* stiff soil profile). In this study, all 2012 buildings are designed for site class D. For the 1994 UBC buildings, a similar type of soil profile, S_2, is assumed, which corresponds to medium dense to dense soil conditions. In the 1967 and 1973 UBC, soil conditions are not required in calculation of design forces.

All buildings are modeled as two-dimensional, three bay, space frames as shown in Figure 3.5(a). The height of the first floor is assumed to be 15 feet and all the upper floors are 13 feet high. The columns in the two-dimensional frames are assumed to be 20 feet apart. The analytical models are implemented in the software *OpenSees* (2012). The nonlinear models must be capable of capturing different modes of strength and stiffness deterioration and component failure to successfully simulate structural collapse. The models used in this study use lumped plasticity beam-column elements to describe the flexural behavior of structural members. The plastic hinges are modeled using the hysteretic material developed by Ibarra *et al.* (2005), which can simulate the strength and stiffness deterioration due to hysteresis under dynamic loading. The material properties for the plastic hinges, such as strength, cracked stiffness, deformation capacity, and cyclic deterioration, are calculated based on empirical relationships obtained by

[2] The drift limit in the 1994 UBC is calculated by multiplying the drift requirement by the deflection amplification factor in the 2012 IBC. This ensures drift limits are comparable, since the 2012 IBC amplifies deflections obtained from analysis for drift calculations.

calibrating the model to experimental test results for more than 250 reinforced concrete columns (Haselton *et al.* 2008). The modeled properties of the beam-column plastic hinges vary depending on the structural element size and reinforcement detailing. As mentioned earlier in this section, the non-ductile buildings may be vulnerable to column shear failure and subsequent loss of gravity-load bearing capacity. The previously described lumped plasticity beam-column element is not sufficient for capturing these failure modes. Therefore, zero-length shear and axial springs are lumped along with the rotational spring at the top of the columns.

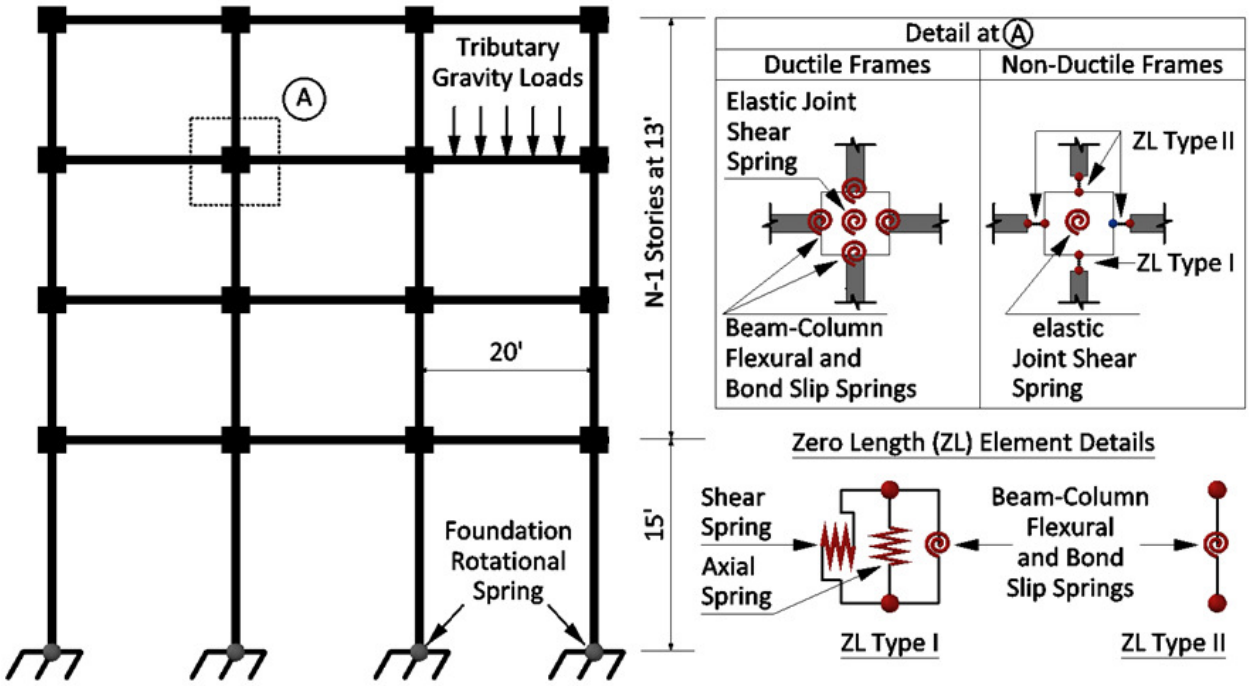

Figure 3.5. Graphical representation of the analytical building model along with nonlinear modeling parameters.

The axial and shear failure springs for each column are modeled with uniaxial materials. The model tracks the response of the associated beam-column element and detects axial and shear failure based when the response reaches pre-defined shear and axial limit surfaces. The shear and axial limit state surface is determined based on the properties of the columns. In the case of shear failure, the limit surface is defined in the small displacement range by the strength relationship proposed by Sezen (2002) and in the larger displacement range by the force-

displacement relationship proposed by Elwood (2004). The Sezen (2002) curve is triggered in the event of brittle shear failure; while the Elwood (2004) curve is triggered in the case a column yields in flexure, then fails in shear. Once the response reaches this surface, the properties of the respective shear and axial springs are updated to represent the expected negative slope of the element (Baradaran Shoraka and Elwood 2013). The response of the column is determined by the flexural response of the column until shear failure occurs. Since shear capacity design required for all the ductile moment resisting frames from the 1973 UBC onwards, it prevents column shear failures and this failure mode mode is not included in models of 1973 or later buildings. The axial force-displacement limit surface is defined by Elwood (2004). Flexible foundations are modeled by employing elastic, semi-rigid rotational springs at the base of base ground floor columns. A leaning column is connected to the frame by rigid struts to account for the destabilizing P-delta effects due to gravity loads not tributary to the frame.

3.5 Building Collapse Simulation

Incremental dynamic analysis (IDA) is carried out on each building model to measure the response of the structure under different ground shaking recordings (Vamvatsikos and Cornell 2002). In incremental dynamic analysis, a building simulation model is subjected to a ground motion with a particular intensity and the structural response is simulated. The ground motion is then scaled and reapplied to the building model, again measuring structural response. This process of scaling the ground motion continues until the structure collapses. The analysis is then repeated for other ground motions.

In the nonlinear dynamic analysis, collapse occurs when (a) interstory drifts increase without bounds due to large flexural deformations in beams and columns (“sidesway” collapse), (b) the total shear demand experienced by the columns in a story exceeds the total shear capacity

of columns at that story, or (c) the total gravity load (axial) demand experienced by the columns in a story exceeds the total axial capacity of columns at that story. Sidesway collapse due to large interstory drifts is the expected collapse mode for ductile moment frames that are susceptible to large flexural deformations under lateral loading (Haselton *et al.* 2011). On the other hand, the non-ductile buildings are incapable of undergoing such large deformations, instead experiencing brittle shear or axial in columns at small drift levels. Therefore, the global capacity-demand failure criteria (b) and (c) are used to identify when collapse occurs due to these failure modes. These criteria are similar to those proposed by Baradaran Shoraka (2013) The shear capacity of each column at each time step of the analysis is determined from the shear limit state surface that has been previously described. Once the response of the column reaches the limit surface, shear failure is initiated in the shear spring and its shear capacity deteriorates. In this region, the shear capacity is assumed to be equal to the demand in shear spring. This assumption is made since once shear failure has occurred; the demand is limited by the shear capacity of the spring. This works to a reasonable assumption as long as the column is experiencing strong part of the accelerogram and it captures shear failure in an effective manner because of strength deterioration of shear spring. The shear capacity of a column deteriorates until it reaches a residual level. Once the shear capacity is evaluated at the element (column) level at a particular time step, the story shear capacity is calculated as the sum of shear capacities for all columns at that story. Global lateral collapse occurs when the story shear capacity becomes lesser than residual story shear capacity for any floor. The residual story shear capacity is calculated as the sum of residual capacities of columns for that story determined according to column properties. Due to challenges with model convergence, this collapse mode is also triggered if the shear capacities of 3 or more columns (of 4 columns) in any story have deteriorated to the residual

level. A similar criterion is adopted for determining global axial failure of the structure. In this case, the column axial demand is calculated from the vertical (gravity) forces acting on the structure. Before column failure is triggered, the column axial capacity is calculated based on the axial limit surface proposed by Elwood (2004). Once the column response hits the limit surface, the column axial capacity is assumed to be zero from that time step onwards. This assumption is based on the sudden nature of axial failure resulting in drastic reduction of column capacity, which also produces convergence problems. The story axial demand and story axial capacity is calculated as the sum of axial demand and axial capacity for the columns at that level.

A significant consideration when conducting IDAs is the choice of measure to quantify the intensity of the ground motion (referred to as an "intensity measure" or IM). Two possible intensity measures are the elastic spectral acceleration at a building's fundamental period, $S_a(T_1)$, and the inelastic spectral displacement at the fundamental period, $S_{di}(T_1)$. $S_a(T_1)$ is one of the most commonly used IMs. It cannot, however, capture the spectral shape of the ground motion, which can significantly influence nonlinear structural response (Baker and Cornell 2006; Haselton *et al.* 2011). Consequently, an alternative IM, the inelastic spectral displacement metric, is also used here. $S_{di}(T_1)$ is defined as the maximum displacement of a single-degree-of-freedom oscillator with bilinear behavior (Tothong and Luco 2007).

As illustrated in

Figure 3.6(a), the oscillator is assumed to have the same period as the fundamental period of the building of interest and a 5% post-yield hardening stiffness ratio. The yield displacement, d_y, is calculated according to FEMA (2009) based on nonlinear static pushover analysis of the building model. The value of S_{di} reflects both the intensity and shape of the ground motion

spectra, due to period elongation of the oscillator that makes it respond to different regions of the spectra. Although S_{di} cannot capture higher mode effects, it is a simple measure that sufficiently captures the effects of spectral shape on structural response and ensures that structural response is not biased by the scale factor applied to the record for the analysis (Tothong and Luco 2007). It is worth stating, however, that the hazard curves developed by USGS (2012) are in terms of *Sa(T).* These curves are required for calculation of an annualized probability of collapse of structure at a particular site that accounts for the seismic hazard.

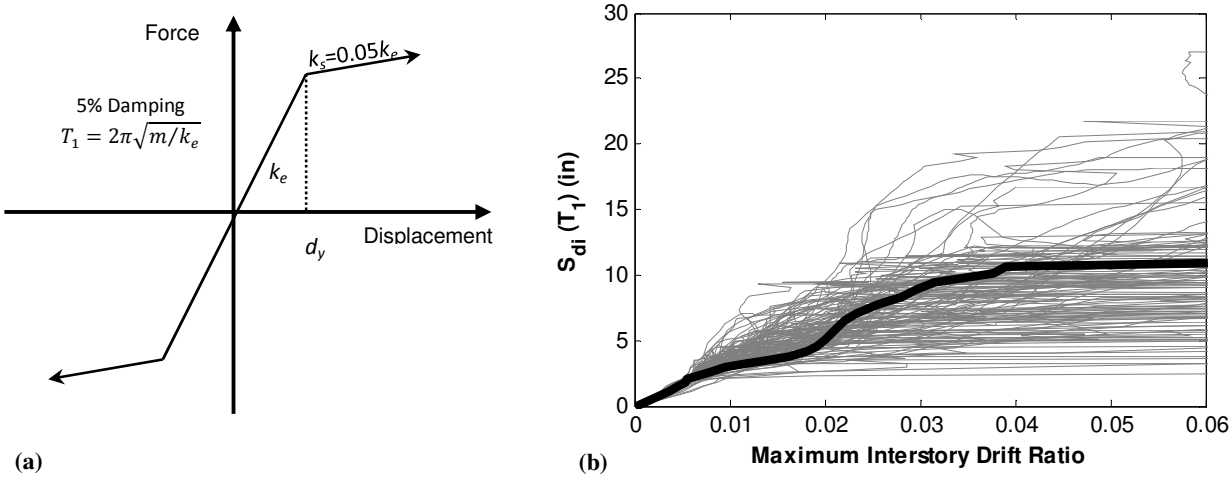

Figure 3.6. (a) Properties of a single-degree-of-freedom oscillator for calculation of $S_{di}(T_1)$. (b) Incremental dynamic analysis results for 4 story building in Portland designed according to the 2012 IBC. In (b), the black line highlights the results for a single ground motion.

Figure 3.6(b) illustrates incremental dynamic analysis results for a 4 story Portland building designed according to 2012 IBC and subjected to the *Subduction* ground motion set. The collapse capacity of the structure is quantified by the ground motion intensity at which collapse occurs for each of the different ground motions. For the highlighted ground motion in

Figure 3.6(b), collapse occurs at S_{di} = 11.3in, in which the original ground motion is scaled by a factor of 5.2 to cause collapse of the structure. These results are used to compute the

median and dispersion of the collapse capacity, where the median collapse capacity corresponds to the intensity of ground motion that has a 50% probability of causing collapse of the building and the uncertainty in the collapse capacity is due to record-to-record variability in structural response. For the structure and ground motion set in

Figure 3.6(b), the median collapse capacity is S_{di} = 9.6in and the dispersion (quantified by the logarithmic standard deviation) is 0.47.

One of the concerns of using incremental dynamic analysis is excessive scaling of the ground motions, resulting in unrealistic structural response. However, Tothong and Luco (2007) have shown that if intensity of the ground motion is measured in terms of S_{di}, structural response is not biased by the scale factor applied to the record for the analysis. Also, the ground motion recordings that cause collapse of the buildings extremely rare, therefore scaling of ground motions is necessary to obtain these rare ground. For the incremental dynamic analysis of the 4 story building in Figure 3.6(b), scale factors varying between 1.7-11.7 (average 5) are applied to *Crustal* ground motions to induce collapse in the structure.

3.6 Assessments of Collapse Risk

3.6.1 Collapse Fragility of Archetype Buildings

To quantify the collapse safety of a building on being subjected to crustal and subduction records, building collapse fragility curves for a given type of earthquake event are generated from the incremental dynamic analysis results. Table 3.3 summarizes the collapse analysis results in terms of the median S_{di} collapse capacity (denoted x_m) and lognormal standard deviation of the fragility curve (denoted β) for all of the archetype buildings considered in the study. The collapse S_{di} values for a particular building are assumed to follow a lognormal

distribution. The goodness-of-fit of the distribution is not rejected with the Kolmogorov–Smirnov normality test at the 5% significance level.

Table 3.3. Summary of collapse fragility curve parameters for all archetypical buildings subjected to Crustal, Subduction and Simulated subduction ground motion sets.

ID[1]	Crustal (C)		Subduction (S)		Simulated (Si)		Variation in x_m (%)			Variation in β (%)		
	x_m (in) [2]	β[3]	x_m (in)	β	x_m (in)	β	C vs. S	C vs. Si	S vs. Si	C vs. S	C vs. Si	S vs. Si
6002	4.2	0.29	3.6	0.28	2.8	0.36	13%	33%	23%	5%	-23%	-29%
7002	10.6	0.30	7.1	0.29	4.2	0.46	33%	60%	40%	2%	-55%	-57%
9002	9.9	0.32	6.0	0.33	4.2	0.50	40%	58%	30%	-5%	-56%	-49%
2002	10.2	0.28	5.2	0.39	4.3	0.45	49%	58%	17%	-40%	-62%	-16%
6004	6.9	0.27	5.9	0.24	5.1	0.25	15%	26%	14%	12%	8%	-4%
7004	14.3	0.35	8.6	0.23	6.9	0.24	40%	52%	20%	34%	30%	-6%
9004	14.9	0.36	8.4	0.28	6.6	0.39	44%	56%	22%	22%	-6%	-36%
2004	14.9	0.37	8.4	0.30	6.5	0.39	44%	57%	23%	20%	-4%	-30%
6008	9.2	0.18	7.7	0.23	7.8	0.27	17%	16%	-2%	-28%	-50%	-17%
7008	19.9	0.22	14.2	0.32	12.7	0.29	29%	36%	10%	-47%	-31%	11%
9008	23.1	0.21	16.8	0.36	13.4	0.34	28%	42%	20%	-70%	-63%	4%
2008	20.5	0.27	14.1	0.32	12.8	0.34	31%	38%	9%	-16%	-25%	-8%
6102	4.3	0.30	3.7	0.26	2.8	0.37	13%	34%	24%	14%	-21%	-42%
7102	11.0	0.32	7.5	0.26	4.3	0.48	32%	61%	42%	17%	-52%	-82%
9102	9.9	0.32	6.0	0.33	4.2	0.50	40%	58%	30%	-5%	-56%	-49%
2102	8.7	0.43	5.8	0.34	4.1	0.43	34%	52%	28%	22%	0%	-28%
6104	6.8	0.23	6.3	0.28	5.1	0.21	8%	25%	19%	-22%	8%	24%
7104	13.9	0.37	9.2	0.26	6.6	0.27	34%	52%	28%	30%	26%	-6%
9104	14.9	0.36	8.4	0.28	6.6	0.39	44%	56%	22%	22%	-6%	-36%
2104	14.9	0.37	8.5	0.30	6.8	0.37	43%	54%	19%	18%	-1%	-23%
6108	9.0	0.20	8.1	0.31	3.0	0.40	10%	67%	63%	-60%	-104%	-27%
7108	20.1	0.22	15.1	0.30	13.9	0.29	25%	31%	8%	-37%	-31%	4%
9108	23.1	0.21	16.8	0.36	13.4	0.34	28%	42%	20%	-70%	-63%	4%
2108	22.3	0.23	15.8	0.32	14.0	0.27	29%	37%	11%	-38%	-15%	17%
6202	4.3	0.30	3.7	0.26	2.8	0.37	13%	34%	24%	14%	-21%	-42%
7202	11.0	0.32	7.5	0.26	4.3	0.48	32%	61%	42%	17%	-52%	-82%
9202	10.1	0.29	5.3	0.40	4.3	0.41	48%	57%	18%	-38%	-43%	-3%
2202	9.5	0.36	5.4	0.37	4.3	0.36	43%	55%	21%	-3%	-1%	2%
6204	6.8	0.23	6.3	0.28	5.1	0.21	8%	25%	19%	-22%	8%	24%
7204	13.9	0.37	9.2	0.26	6.6	0.27	34%	52%	28%	30%	26%	-6%
9204	14.1	0.30	8.2	0.30	6.4	0.41	41%	54%	22%	1%	-35%	-36%
2204	14.9	0.35	9.1	0.35	6.4	0.45	39%	57%	30%	0%	-28%	-28%
6208	9.0	0.20	8.1	0.31	3.0	0.40	10%	67%	63%	-60%	-104%	-27%
7208	20.1	0.22	15.1	0.30	13.9	0.29	25%	31%	8%	-37%	-31%	4%
9208	23.5	0.24	16.2	0.33	12.9	0.31	31%	45%	20%	-36%	-29%	5%
2208	22.0	0.24	14.8	0.37	12.5	0.36	33%	43%	16%	-58%	-51%	5%

[1] Building information provided in ID: First digit indicates the design era (7: 1973, 9: 1994, 2: 2010), the second digit indicates the location of the building (0: Seattle, 1: Portland, 2: Los Angeles) and the last two digits indicate the number of stories.
[2] Median collapse capacity (x_m) is quantified in terms of S_{di}.
[3] Logarithmic standard deviations of collapse capacity.

To dig into the trends in these results,

Figure 3.7 illustrates the collapse fragility curves calculated separately for each of the *Crustal*, *Subduction* and *Simulated* ground motion sets for the Portland, Seattle and Los Angeles 4 story modern buildings. These results indicate that the median collapse capacity of the Portland and Seattle buildings is 43% and 44% higher (*i.e.,* has a lower probability of collapse) if subjected to only *Crustal* ground motions, rather than the *Subduction* motions. The Los Angeles building, which has higher maximum base shear (from nonlinear pushover analysis) than Portland and Seattle buildings, showed a similar increase in median collapse capacity (39%) on being subjected to *Crustal* instead of *Subduction* ground motions. These results imply that, for a given level of ground motion intensity, the probability of collapse for these 4 story buildings is lower if the ground shaking comes from a crustal earthquake than if it comes from a subduction earthquake. Similarly,

Figure 3.8 demonstrates the variation in collapse fragility curves for the non-ductile 4 story buildings designed according to 1967 UBC for the cities of Seattle, Portland and Los Angeles when subjected to *Crustal*, *Subduction* and *Simulated* ground motions. The *Subduction* ground motion set reduces the collapse capacity of buildings in Portland, Seattle and Los Angeles by 15%, 8% and 8%, respectively, in comparison to *Crustal* set. Although the trend is the same as that observed for the modern buildings, the decrease in the collapse capacity is not as large as that observed for buildings designed according to the 2012 IBC (

Figure 3.7).

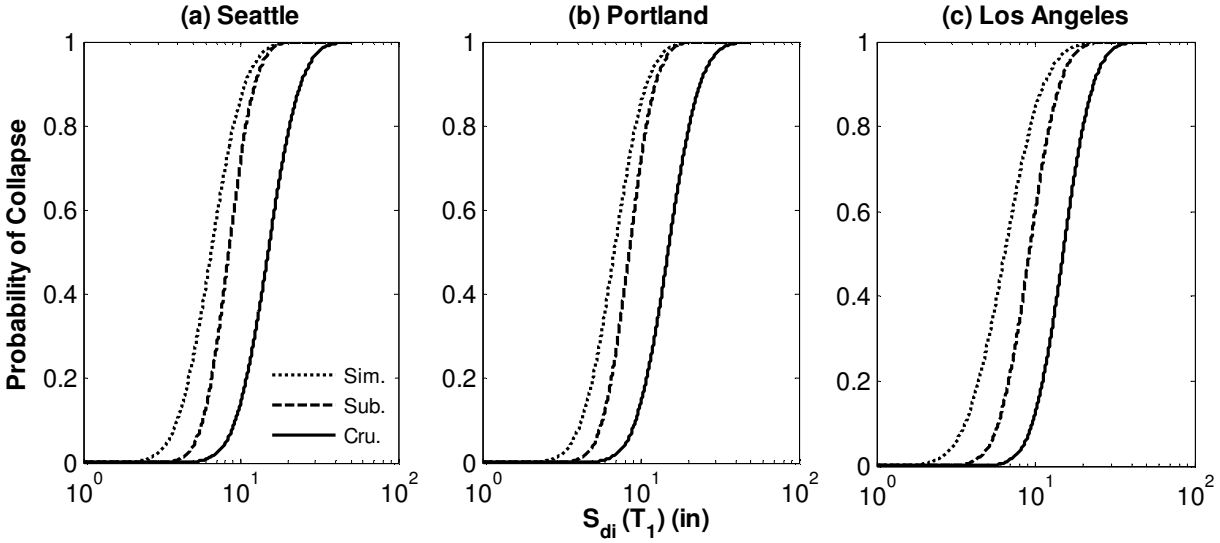

Figure 3.7. Building collapse fragility curves developed for 4 story buildings designed according to current codes (2012 IBC) in Portland, Seattle and Los Angeles for the three different ground motion sets.

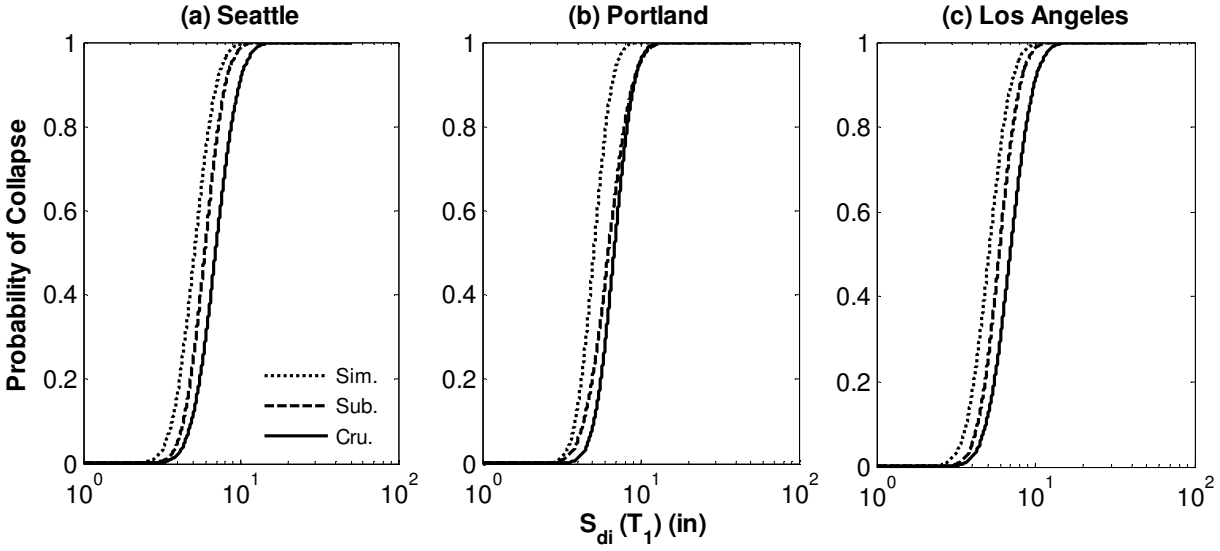

Figure 3.8. Building collapse fragility curves developed for 4 story buildings designed according to outdated codes (1967 UBC) in Portland, Seattle and Los Angeles for the three different ground motion sets.

In Figure 3.9, the variation in median collapse capacities from *Crustal*, *Subduction* and *Simulated* sets of ground motions are illustrated for the 4 story Portland buildings designed according to the 1967 UBC, the 1973 UBC, the 1994 UBC and the 2012 IBC. These results confirm that the gap between collapse capacities under *Subduction* and *Crustal* motions is wider

for more ductile buildings. These differing impacts of subduction motions can be explained by the longer duration of subduction ground motions and different deformation capacities and levels of cyclic deterioration of the buildings designed to represent different eras. For ground motions having the same S_{di}, the longer duration ground motions are more damaging to all structures, due to the larger number of load reversal cycles and the hysteretic energy demand on the structure. However, the rate of reduction in collapse capacity with duration is higher for ductile buildings as compared to non-ductile buildings due to their large deformation capacities; for structures with smaller deformation capacity and hysteretic energy capacity, duration is less important because even a short duration record is able to exhaust the structure's capacity (Raghunandan and Liel 2013).

On average, ductile (2012 IBC) and non-ductile (1967 UBC) buildings subjected to *Subduction* ground motions have median collapse capacities that are 36% and 12% lower respectively, than when subjected to *Crustal* ground motions, confirming the trends observed in

Figure 3.7,

Figure 3.8 and Figure 3.9 for the 4 story buildings. In addition, the building collapse capacities measured under recorded *Subduction* ground motions are around 24% higher than those obtained with the *Simulated* subduction motions. Results also show that the record-to-record variability in the collapse capacity, represented by β, is slightly lower for the *Crustal* fragility curves (average of 0.29 across all the buildings) as compared to the fragility curves obtained using the *Subduction* or *Simulated* sets (average of 0.31 and 0.36), which is probably due to the wider range of ground motion durations found in either of the two subduction sets. In spite of these variations, the consistent trend of decrease in collapse capacities of buildings due

to subduction ground motions definitively indicates the higher vulnerability of the building stock to subduction rather than crustal shaking and the need for including their effects in building design.

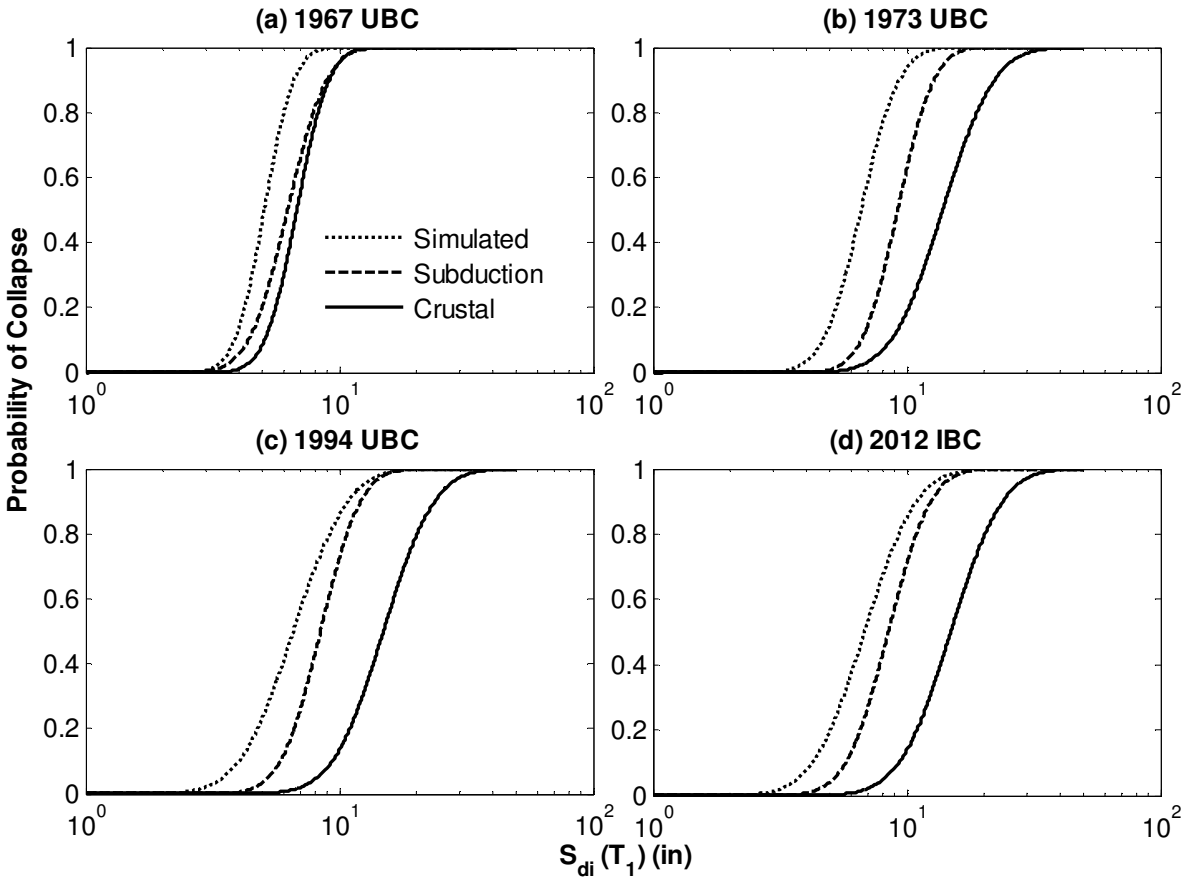

Figure 3.9. Building collapse fragility curves developed for 4 story buildings designed according to 1967 UBC, 1973 UBC, 1994 UBC and 2012 IBC in Portland, showing increasing discrepancy between response to subduction and crustal motions for the new, more ductile buildings.

Besides the differences observed in collapse capacities between results obtained when subjected to *Crustal* or *Subduction* motions, the absolute median collapse capacity of the buildings located in Portland, Seattle and Los Angeles vary according to the design era, design seismic forces and design detailing requirements. The median collapse capacity here is quantified in terms of *Sa (T=1s)* for all buildings. A spectral period of 1s second is employed for all structures because it permits comparison among the buildings with different T_1. Table 3.4

summarizes the collapse median capacity for *Crustal* set of ground motions for the all the buildings and this information is sufficient for comparison of strength amongst buildings. As seen in Table 3.4, among the older non-ductile buildings (1967 UBC), all of the buildings with the same number of stories have similar collapse capacities, regardless of building location, because the dominant mode of failure for these buildings is shear and axial failure of the columns and all buildings had similar column sizes with large reinforcement spacing. For the first generation of more ductile buildings (1973 UBC), the Los Angeles and Seattle buildings have the larger collapse capacities than Portland buildings due to the differences in design seismic zone. However, in 1994, due to increase in seismic design forces for Portland buildings due to identification of Cascadia subduction hazard, the collapse capacities of Portland and Seattle are the same (same design forces) and the Los Angeles buildings have higher collapse capacities because they are designed for higher design forces. For the modern buildings (2012 IBC), the design forces are lowest for Portland and largest for Los Angeles with Seattle in between. The same trend is reflected in the collapse capacities, such that collapse capacities in increasing order are: Portland, Seattle and Los Angeles.

Table 3.4 Summary of median collapse capacity for all archetypical buildings subjected to *Crustal* set of ground motions.

Design Code	Number of Stories	Design Base Shear Coefficient			Median Collapse Capacity (*Sa (T =1s)*, (g))					
					Crustal			Subduction		
		Portland	Seattle	Los Angeles	Portland	Seattle	Los Angeles	Portland	Seattle	Los Angeles
1967 UBC	2	0.050	0.100	0.100	0.64	0.63	0.63	0.63	0.62	0.62
1973 UBC	2	0.033	0.067	0.067	1.67	1.62	1.62	1.32	1.26	1.26
1994 UBC	2	0.069	0.069	0.092	1.62	1.62	1.74	1.13	1.13	1.09
2012 IBC	2	0.091	0.114	0.200	1.48	1.69	1.73	1.05	1.02	1.19
1967 UBC	4	0.034	0.068	0.068	0.62	0.69	0.69	0.59	0.64	0.64
1973 UBC	4	0.023	0.045	0.045	1.23	1.61	1.61	0.83	1.19	1.19
1994 UBC	4	0.053	0.053	0.070	1.67	1.67	1.64	1.04	1.04	1.02
2012 IBC	4	0.068	0.081	0.130	1.66	1.66	1.89	1.03	1.02	1.21
1967 UBC	8	0.027	0.054	0.054	0.6	0.65	0.65	0.54	0.55	0.55
1973 UBC	8	0.018	0.036	0.036	1.18	1.72	1.72	0.88	1.48	1.48
1994 UBC	8	0.038	0.038	0.050	1.79	1.79	1.88	1.41	1.41	1.39
2012 IBC	8	0.037	0.044	0.071	1.61	1.56	1.79	1.22	1.16	1.30

3.6.2 Influence of Ground Motion Parameters on Collapse Capacity

Previous research demonstrates that ground motion frequency content and duration both strongly influence structural response. Additionally, it is well-established that subduction earthquakes have distinct duration and frequency content from crustal records (as in Figure 3.3). This section investigates how these two ground motion parameters influence the observed trends in collapse capacity between ground motions from crustal and subduction earthquakes.

3.6.2.1 Frequency Content of the Ground Motions

As described previously, subduction ground motions are expected to have higher energy associated with longer periods. The primary objective of using inelastic spectral displacement (S_{di}) as an intensity measure is to quantify the effect of spectral shape and ground motion intensity on structural response since the bilinear oscillator used to calculate S_{di} elongates during response "feeling" the spectral intensity at long period. Therefore, the results expressed in terms of S_{di} already include the influence of different spectral shapes of *Crustal* and *Subduction* set of ground motions on building response and collapse capacity. To illustrate this point, Figure 3.10 shows pairs of ground motions that have the same S_{di} and cause collapse of a building at the same level, but have different spectral shapes and even different $Sa(T_1)$. The differences in shapes between the records with equal S_{di} demonstrate the power of the S_{di} intensity measure in reflecting ground motion frequency content. In a sense, the use of S_{di} puts the crustal and subduction ground motion sets on a level playing field in terms of frequency content and intensity, wherein both the spectral intensity at T_1 and for $T > T_1$ are considered in the composite S_{di} IM. To illustrate this point more generally, Figure 3.11(a) fits a linear regression between the collapse capacities the ductile buildings and ground motions (quantified in terms of spectral acceleration at which collapse occurs $Sa(T_1)$) and the fundamental period of the building (T_1).

Since $Sa(T_1)$ is calculated solely at T_1, this IM does not account for the ground motion's spectral intensities at any other period. In order to see the variation of frequency content of the *Crustal* and *Subduction* ground motion sets, separate linear regression between collapse $Sa(T_1)$ and T_1 is fitted to both ground motion sets and it is seen that the slope fit to the *Crustal* results is 48% higher that the subduction set. This implies the *Crustal* collapse capacities have a different relationship with building period than the *Subduction* collapse capacities, implying a sensitivity to ground motion spectral shape. Once the intensity measure is switched to $S_{di}(T_1)$ as in Figure 3.11(b), the slope of the linear regression line for the *Crustal* set is only 13% higher than slope of regression line for *Subduction* set. A similar trend was observed for the non-ductile buildings (not shown). These findings therefore suggest that, while there is definitely difference in frequency content between crustal and subduction ground motions, but it is accounted for the collapse capacity comparisons by using S_{di} instead of $Sa(T_1)$.

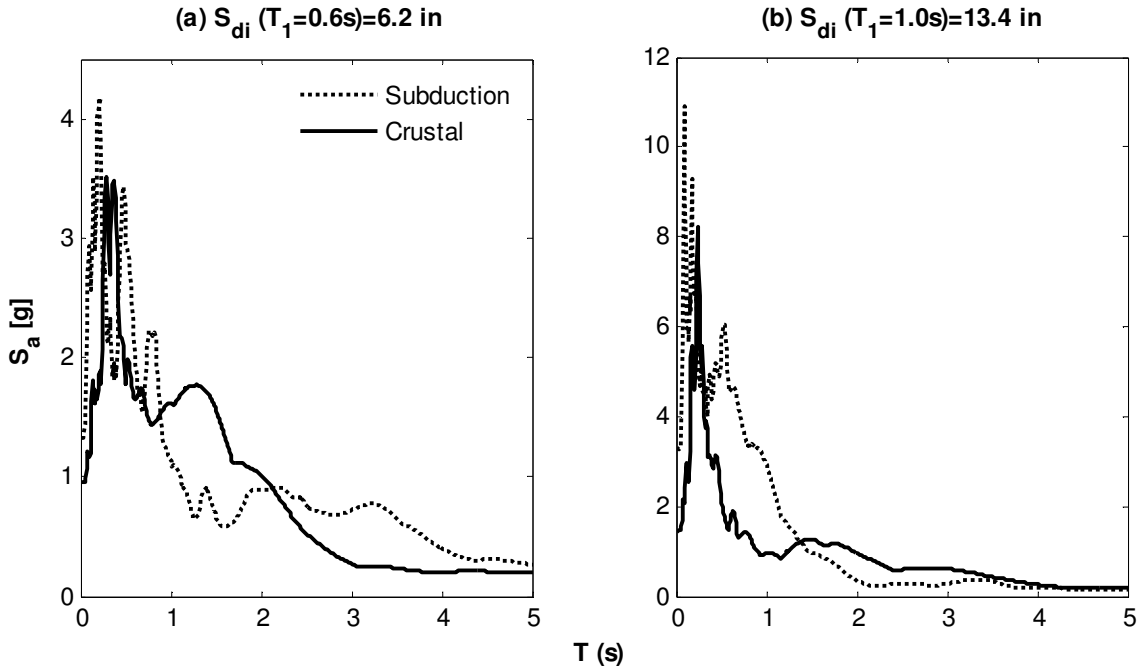

Figure 3.10 Response spectra for pairs of ground motions producing the same collapse capacity when quantified in terms of S_{di}, for (a) the 1994 UBC 2 Story Seattle Building and (b) the 2012 IBC 4 Story Seattle Building. The ground motion records shown in (a) are crustal: Kocaeli, Turkey (M_w 7.5, 1999) and subduction: Kepulauan Mentawai, Indonesia (M_w 7, 2007) and in (b) are crustal: El Centro (M_w 6.5, 1979) and subduction: Tokachi Oki (M_w 8.3, 2003).

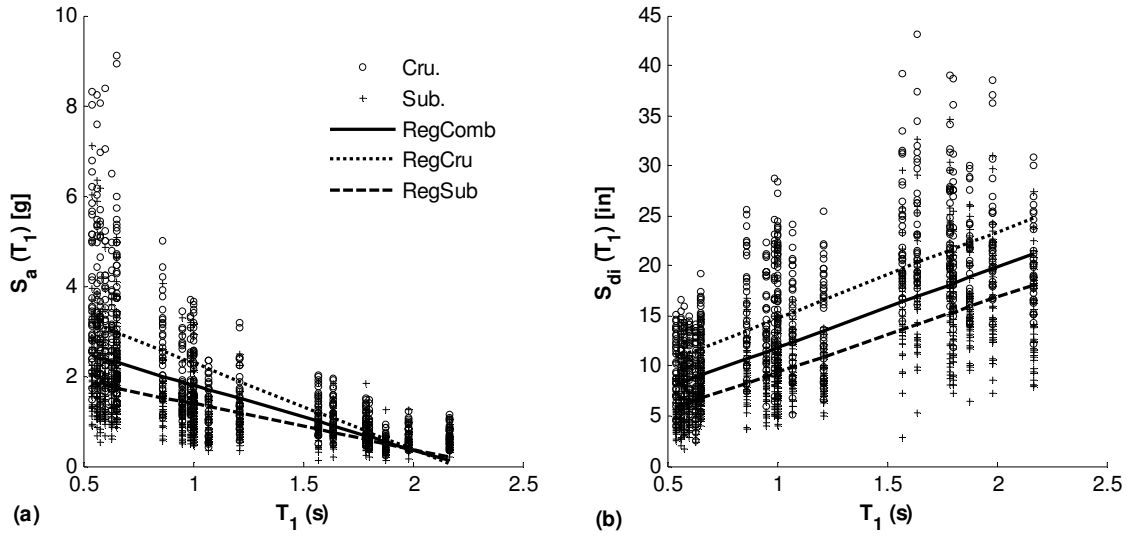

Figure 3.11 Variation of collapse capacity of the 27 ductile buildings with T_1 calculated using intensity measures (a) spectral acceleration, $Sa(T_1)$ and (b) inelastic spectral displacement S_{di} for the *Crustal* and *Subduction* ground motions.

3.6.2.2 Ground Motion Duration

Raghunandan and Liel (2013) (Chapter 2 of this thesis) found that ground motion duration is significant in predicting the collapse capacity of the structure. Since S_{di} accounts for most of the ground motion long period frequency content, the duration of the ground motion can be considered as the main reason for observed reduction in collapse capacity in Table 3.3. To further confirm this statement, the generalized linear regression model (GLM) by Raghunandan and Liel (2013) is used to predict the collapse capacity of each building when subjected to each of the records in the database. The GLM model takes as input ground motion duration and structural parameters related to the building fundamental period and deformation capacity. Figure 3.12 plots the collapse S_{di} obtained from nonlinear dynamic analysis ("Actual S_{di}") against the model predictions ("Estimated S_{di}"). In Figure 3.12(a) the results for all building are scattered more or less symmetrically around the 45^0 line, indicating that the estimates for S_{di} from the GLM model are similar to the observed value for most of the buildings and that the ground motion duration parameter has significant explanatory power for the trends observed. However,

there are some points that are substantially offset from the 45^0 line for both *Crustal* and *Subduction* records. Closer evaluation of results for individual buildings (*e.g.* Figure 3.12(b) and (c)) revealed that this offset occured mainly for taller buildings (8 story). This observation suggests that higher mode effects that are important predictors of collapse capacity for taller buildings that are not accounted for by the S_{di} and duration-based model. The effects of higher modes are not judged to be crucial here, since they introduces a small and consistent bias in both the *Crustal* and *Subduction* collapse assessments. We find no systematic bias associated with long period frequency content, confirming that spectral shape issues are adequately covered by the existing model.

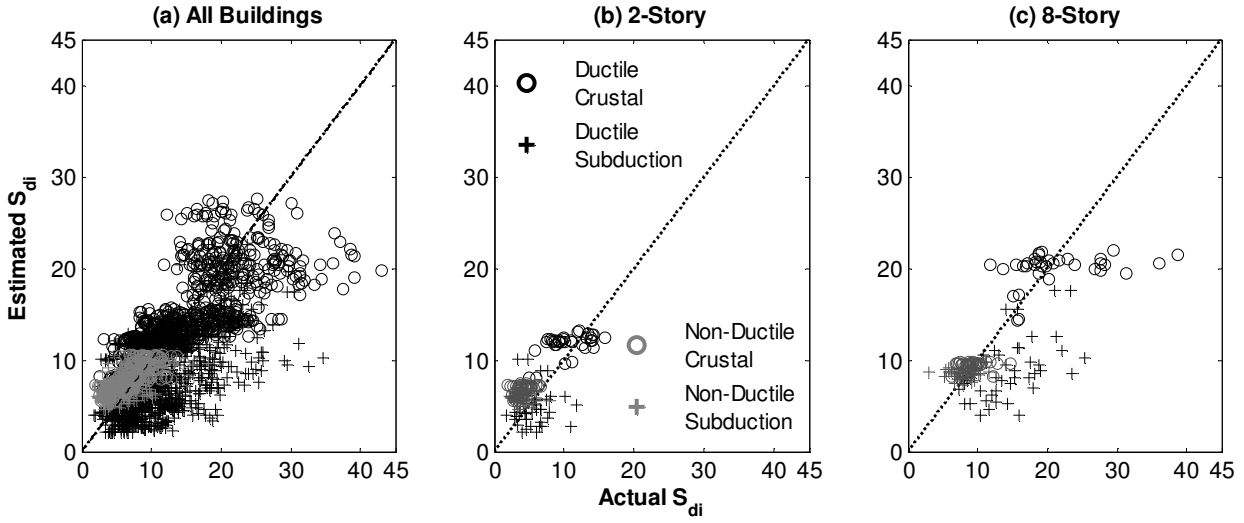

Figure 3.12 Comparison of actual collapse S_{di} from nonlinear dynamic analyses of building models and estimated collapse S_{di} estimated from the prediction equation in Raghunandan and Liel (2013).

3.6.3 Seismic Collapse Risk

USGS (2012a) provides seismic hazard curves for every location, defining ground motion intensity in terms of *Sa(T)* for pre-defined values of T. In theory, probabilistic seismic hazard analysis could be conducted in terms of $S_{di}(T)$. However, this information is not currently available. Accordingly, in this study, collapse fragility curves are recalculated for *Crustal* and

Subduction ground motions for the IM *Sa (T=1s)* for the buildings. There is a general increase in the record-to-record variability of collapse fragility curves with *Sa(T=1s)* as compared to $S_{di}(T_1)$ because the former does not account for spectral shape effects and because of the use of a common period in the calculations. The median collapse capacities with the *Sa(T=1s)* are 15% to 35% (average of 30%) lower for *Subduction* ground motions as compared to *Crustal* ground motions for all the buildings.

The probability of collapse in 50 years for each building is quantified using Equation 3.6.1 and 3.6.2, assuming a Poisson distribution of earthquake occurrences:

$$P[Collapse] \approx Annual\ rate\ of\ collapse = \int_0^\infty \lambda[SA]\ f(c)dc \tag{3.6.1}$$

$$P[Collapse\ in\ 50\ years] = 1 - (1 - P[Collapse])^{50} \tag{3.6.2}$$

In these calculations, $P[Collapse]$ is the annual collapse probability (which is equal to annual frequency of collapse for small probability values), $\lambda[SA]$ is the mean annual frequency of exceedance of the spectral acceleration demand, and $f(c)$ is the lognormal probability distribution of the collapse capacity, *i.e.* the derivative of the collapse fragility curve. Both the capacity (c) and the demand (SA) are quantified in terms of *Sa(T=1s)*. For consistency with previous studies, the standard deviation of natural logarithm of collapse capacity, β, is assumed to be equal to 0.8, and considers uncertainty in design and modeling on top of record-to-record variability (Luco *et al.* 2007). In this study, these calculations are carried out separately for crustal and subduction events for each building by substituting the respective site-specific hazard

curve and collapse fragility curve in Equation 3.6.1 and 3.6.2. USGS (2012) generates the separate hazard curves by deaggregating the total hazard curve for a site and then grouping the portions of the hazard associated with the different types of earthquake events. The two collapse probabilities are then added together to calculate the annual total $P[Collapse]$ and $P[Collapse\ in\ 50\ years]$ for a building at a site (Equation 3.6.3 and 3.6.4).

$$P[Collapse]_{T} = P[Collapse]_{Cru} + P[Collapse]_{Sub} \tag{3.6.3}$$

$$P[Collapse\ in\ 50\ years]_{T} = P[Collapse\ in\ 50\ years]_{Cru} + P[Collapse\ in\ 50\ years]_{Sub} \tag{3.6.4}$$

To illustrate this process, Figure 3.13(a) provides hazard curves for the three sites (Seattle, Portland and Los Angeles) assuming a soil site (NEHRP Site Class D, V_{s30}=230m/s). Figure 3.13(b) shows the corresponding set of building capacity curves for 4 story buildings designed according to the 2012 IBC.

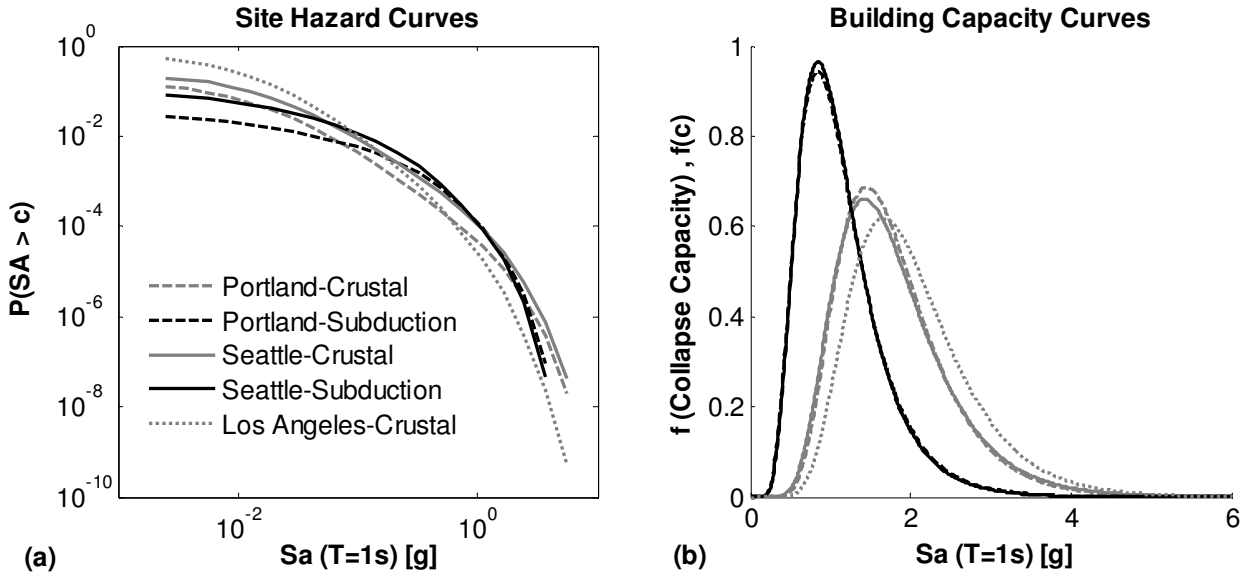

Figure 3.13. For sites in Portland, Seattle and Los Angeles: (a) seismic hazard curves for a soil site, and (b) building capacity curves for the 4 story building designed according to current codes (derivative of building fragility curve).

Table 3.5. Metrics of collapse risk for archetypical buildings.

P [Collapse] [1]												
Building Code	Stories	Seattle					Portland					Los Angeles
		C	S	T-CS	T-C	T-C vs. T-CS	C	S	T-CS	T-C	T-C vs. T-CS	T
1967 UBC	2	6.7×10^{-4}	1.0×10^{-3}	1.7×10^{-3}	1.6×10^{-3}	-0.5%	2.8×10^{-4}	6.7×10^{-4}	9.6×10^{-4}	9.4×10^{-4}	-1.6%	5.2×10^{-4}
1967 UBC	4	5.6×10^{-4}	9.7×10^{-4}	1.5×10^{-3}	1.4×10^{-3}	-7.4%	2.9×10^{-4}	7.4×10^{-4}	1.0×10^{-3}	9.8×10^{-4}	-5.9%	4.2×10^{-4}
1967 UBC	8	6.2×10^{-4}	1.2×10^{-3}	1.8×10^{-3}	1.5×10^{-3}	-17.4%	3.1×10^{-4}	8.5×10^{-4}	1.1×10^{-3}	1.0×10^{-3}	-10.9%	4.7×10^{-4}
1973 UBC	2	1.0×10^{-4}	2.6×10^{-4}	3.6×10^{-4}	2.5×10^{-4}	-31.1%	4.0×10^{-5}	1.8×10^{-4}	2.2×10^{-4}	1.5×10^{-4}	-31.9%	5.0×10^{-5}
1994 UBC	2	1.0×10^{-4}	3.2×10^{-4}	4.3×10^{-4}	2.5×10^{-4}	-41.2%	4.3×10^{-5}	2.4×10^{-4}	2.9×10^{-4}	1.6×10^{-4}	-43.7%	4.2×10^{-5}
2012 IBC	2	9.5×10^{-5}	4.0×10^{-4}	5.0×10^{-4}	2.3×10^{-4}	-54.1%	5.2×10^{-5}	2.8×10^{-4}	3.3×10^{-4}	1.9×10^{-4}	-41.6%	4.2×10^{-5}
1973 UBC	4	1.0×10^{-4}	2.9×10^{-4}	4.0×10^{-4}	2.5×10^{-4}	-35.9%	7.7×10^{-5}	4.3×10^{-4}	5.1×10^{-4}	2.8×10^{-4}	-43.8%	5.2×10^{-5}
1994 UBC	4	9.8×10^{-5}	3.8×10^{-4}	4.8×10^{-4}	2.3×10^{-4}	-51.2%	4.0×10^{-5}	2.8×10^{-4}	3.2×10^{-4}	1.5×10^{-4}	-53.4%	4.9×10^{-5}
2012 IBC	4	9.9×10^{-5}	4.0×10^{-4}	5.0×10^{-4}	2.4×10^{-4}	-52.1%	4.0×10^{-5}	2.9×10^{-4}	3.3×10^{-4}	1.5×10^{-4}	-54.1%	3.3×10^{-5}
1973 UBC	8	9.2×10^{-5}	1.8×10^{-4}	2.7×10^{-4}	2.2×10^{-4}	-19.6%	8.4×10^{-5}	3.8×10^{-4}	4.7×10^{-4}	3.1×10^{-4}	-34.1%	4.3×10^{-5}
1994 UBC	8	8.5×10^{-5}	2.0×10^{-4}	2.9×10^{-4}	2.0×10^{-4}	-30.0%	3.4×10^{-5}	1.6×10^{-4}	1.9×10^{-4}	1.3×10^{-4}	-32.8%	3.4×10^{-5}
2012 IBC	8	1.1×10^{-4}	3.0×10^{-4}	4.2×10^{-4}	2.7×10^{-4}	-34.9%	4.3×10^{-5}	2.1×10^{-4}	2.5×10^{-4}	1.6×10^{-4}	-36.6%	3.8×10^{-5}

P[Collapse in 50 years] [1]												
Building Code	Stories	Seattle					Portland					Los Angeles
		C	S	T-CS	T-C	T-C vs. T-CS	C	S	T-CS	T-C	T-C vs. T-CS	T
1967 UBC	2	3.3%	5.0%	8.3%	8.1%	-2.4%	1.4%	3.3%	4.7%	4.6%	-2.5%	2.6%
1967 UBC	4	2.8%	4.8%	7.6%	6.9%	-8.8%	1.5%	3.7%	5.2%	4.8%	-6.7%	2.1%
1967 UBC	8	3.1%	6.2%	9.2%	7.5%	-18.4%	1.6%	4.2%	5.8%	5.1%	-11.6%	2.4%
1973 UBC	2	0.5%	1.3%	1.8%	1.3%	-31.1%	0.2%	0.9%	1.1%	0.8%	-31.9%	0.3%
1994 UBC	2	0.5%	1.6%	2.2%	1.3%	-41.2%	0.2%	1.2%	1.4%	0.8%	-43.6%	0.2%
2012 IBC	2	0.5%	2.0%	2.5%	1.1%	-54.0%	0.3%	1.4%	1.7%	1.0%	-41.6%	0.2%
1973 UBC	4	0.5%	1.5%	2.0%	1.3%	-35.9%	0.4%	2.1%	2.5%	1.4%	-43.7%	0.3%
1994 UBC	4	0.5%	1.9%	2.4%	1.2%	-51.0%	0.2%	1.4%	1.6%	0.8%	-53.3%	0.2%
2012 IBC	4	0.5%	2.0%	2.5%	1.2%	-52.0%	0.2%	1.5%	1.7%	0.8%	-54.0%	0.2%
1973 UBC	8	0.5%	0.9%	1.4%	1.1%	-19.8%	0.4%	1.9%	2.3%	1.5%	-34.0%	0.2%
1994 UBC	8	0.4%	1.0%	1.4%	1.0%	-30.1%	0.2%	0.8%	1.0%	0.7%	-32.8%	0.2%
2012 IBC	8	0.6%	1.5%	2.1%	1.4%	-35.0%	0.2%	1.1%	1.3%	0.8%	-36.5%	0.2%

[1] Indicates hazard curve and fragility curve use in calculation of P (Collapse) and P(Collapse in 50 years) (a) C: Hazard Curve-Crustal, Fragility Curve-Crustal [Equation (1,2)], (b) S: Hazard Curve-Subduction, Fragility Curve-Subduction [Equation (1,2)], (c) T-CS: Total value, C+S [Equation (3,4)], (d) T-C: Hazard Curve-Total (Crustal and Subduction), Fragility curve-Crustal [Equation (1,2)].

The same set of calculations is carried out for the three sites and the respective building capacity curves for all of the buildings. In Table 3.5, column "C", $P[Collapse]_{Cru}$ and

$P[Collapse\ in\ 50\ years]_{Cru}$ are calculated based on the hazard curve for crustal earthquakes at the site of interest and the crustal-derived building capacity curve for the building located at that site. Similar calculations are carried out for column "S" , except employing the subduction hazard curve and subduction-derived building capacity curve. In column "T-CS", $P[Collapse]_T$ and $P[Collapse\ in\ 50\ years]_T$ are calculated according to Equations 3.6.3 and 3.6.4. Finally, in column "T-C", $P[Collapse]_T$ and $P[Collapse\ in\ 50\ years]_T$ are calculated from Equations 3.6.1 and 3.6.2 using a crustal building fragility curve and a total seimic hazard curve accounting for both crustal and subduction components of hazard. The variation of $P[Collapse\ in\ 50\ years]$ for all the buildings in Seattle, Portland and Los Angeles is also illustrated in Figure 3.14.

Table 3.5 results indicate that subduction earthquakes contribute about 60-81% of the total seismic collapse risk for buildings located in Seattle. For buildings located in Portland, subduction earthquakes are even more important (accounting for 70-88% of the collapse risk). The higher contribution from subduction earthquakes to the collapse risk (quantified in terms of probability of collapse) is due not only to the damaging features of the ground motions, but also to the fact that these events are likely to lead to ground motions large enough to cause collapse. The lower end of the range of Subduction earthquake contribution in seismic collapse risk above is from old non-ductile buildings because for these buildings the percentage reduction in median collapse capacity between Crustal and Subduction set was smaller.

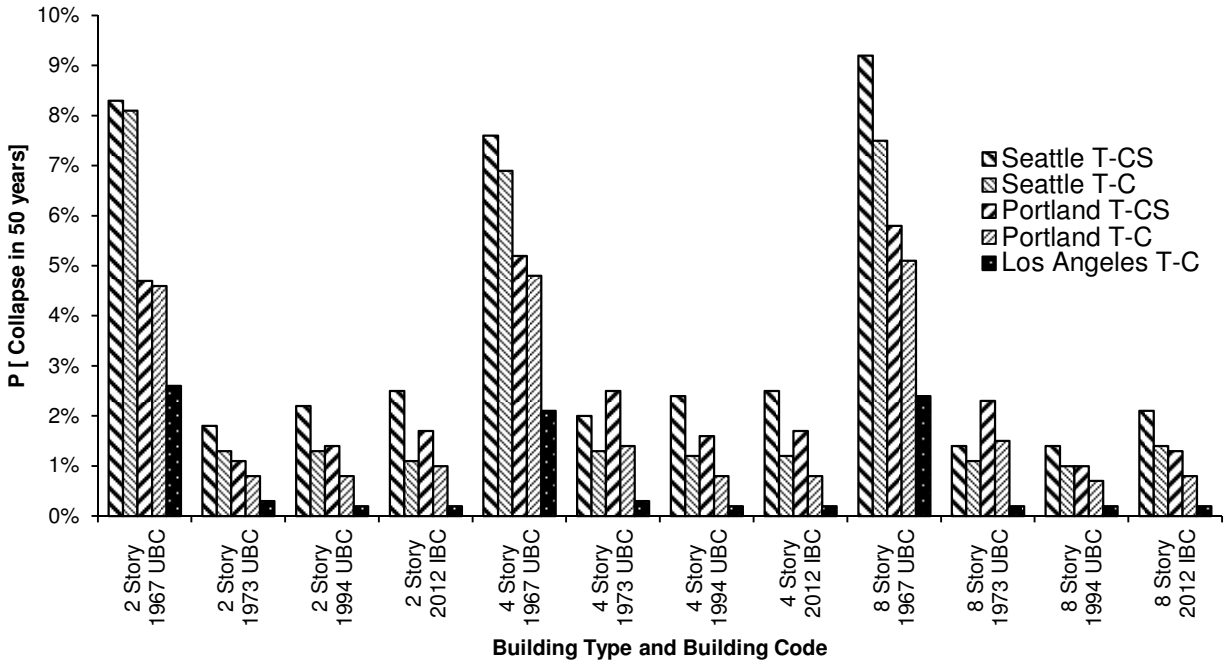

Figure 3.14 Probability of collapse in 50 years for all archetype buildings calculated using (a) separate seismic hazard and building fragility curves for crustal and subduction earthquakes(T-CS) and, (b) Total seismic hazard curve and crustal building fragility curve(T-C).

Table 3.5 represents how the collapse risk calculation is currently conducted for sites susceptible to subduction earthquakes. The collapse risk calculation does not usually employ separate building capacity curves for crustal and subduction earthquakes, although the hazard represents the hazard from all sources (Luco *et al.* 2007). Results from section 3.6.1 indicate that for the same intensity ground motion, the probability of collapse is higher if the building is subjected to subduction earthquake ground motion as compared to crustal earthquake ground motions. Therefore, if the collapse risk calculation does not account for the decrease in collapse capacities from subduction ground motions, the collapse risk of the buildings at sites susceptible to subduction ground motions is underestimated. For the set of the ductile buildings (post 1970) and sites employed in this analysis, $P[Collapse]$ is underestimated on average by 41% if separate building capacity curves for subduction earthquake are not used in building seismic collapse risk calculation for a site at risk of subduction earthquake shaking. However,

$P[Collapse]$ is underestimated only by around 8% on average using Crustal building fragility and total hazard curves in case of non-ductile buildings designed according to 1967 UBC. This lower understimation for non-ductile buildings can be explained based on low energy dissipation capacity leading to brittle failure at low intensities of ground motion which causes less variation in building capacities for Crustal and Subduction set of ground motions.

The risk-targeted design maps in current building codes (ASCE 7-10) define design values (i.e. MCE_R) for a collapse probability 1% in 50 years. However, buildings designed according to these MCE_R have collapse probabilities that are significantly higher for sites in Seattle (2.1 -2.5% in 50 years) and Portland (1.3-1.7% in 50 years). The target uniform probability of collapse for the MCE_R values in the design maps may not be achieved in the Pacific Northwest where there is a significant risk of subduction ground motions. For the Los Angeles site where the seismic hazard is assumed to be completely from crustal sources however, the seismic collapse risk is far below 1% (around 0.2%). This indicates the effectiveness of design values from MCE_R in preventing impending collapse of structures in predominantly crustal hazard dominated sites. It is also interesting to note that, on average all the buildings from different design eras in Seattle and Portland have >1% probability of collapse in 50 years. The collapse risk on an average is around 4.2 and 3.2 times higher for non-ductile older buildings as compared to ductile buildings UBC 1973 onwards indicating high vulnerability of older non-ductile building stock in Pacific Northwest.

3.7 Conclusions

The built environment of the Pacific Northwest region of the U.S. and Canada is at risk from both subduction and crustal earthquake events. To date, most of the research quantifying building response and safety has focused on crustal, California-type ground motions. Due to the

distinct geologic characteristics of subduction earthquake sources and attenuation however, ground motions from subduction events are different from crustal ground motions in terms of duration and frequency content. This paper quantifies the impact of these ground motions on building response for a set of RC frame buildings designed according to 1967, 1973, 1994 and 2012 building codes through nonlinear incremental dynamic analysis. These results are used to quantify the collapse risk – a proxy for building safety – of modern and older buildings in the Cascadia subduction zone.

The principal findings of the study are threefold. First, the median collapse capacity of a ductile and non-ductile structure reduces by an average 36% and 12% respectively when subjected to subduction ground motions as compared to crustal ground motions. This observation, which applies to buildings of varying height and designed to represent a range of building eras, suggests that a smaller intensity subduction ground motion is needed, on average, to collapse a building, compared to a ground motion from a crustal earthquake. Both the longer duration of subduction ground motions and the larger frequency content at long periods contribute to the higher susceptibility of buildings to ground shaking for the subduction events. The second finding stems from the first: due to the unique characteristics of building response under subduction ground shaking, the risk of collapse of modern properly designed buildings in Portland or Seattle is 1.7% and 2.1% in 50 years respectively. These levels of risk are greater than building code targeted value 1% probability of collapse in 50 years. Moreover, the collapse risk in the Pacific Northwest is greater than risk of collapse of an equivalently designed building for Los Angeles (by a factor of 10 for Seattle and 8 for Portland). When the collapse risk is deaggregated by source for the modern buildings, in Portland, subduction shaking contributes about 85% of the collapse risk. In Seattle, subduction shaking contributes about 77%. These

numbers also make it apparent that seismic performance assessments based only on crustal type motions may underestimate significantly the seismic risk in regions with a subduction hazard. The results from this study can be used to modify the design MCE_R values to account for collapse risk from more damaging subduction earthquakes and ensure the uniform 1% in 50 year collapse probability throughout the country.

This study also explored the use of simulated ground motions in nonlinear time history analysis to make up for the limited number of recordings from subduction events. The results show that the simulated ground motions were generally more harmful for structural response than the recorded subduction or crustal ground motions. This difference is attributed to the longer period spectral content of the simulated motions and longer durations than those of the recorded subduction earthquake ground motions. The cause of these spectral differences is unclear. They may be real features of actual large magnitude events, for which few if any recordings are available, an artifact of the simulation process, or both. This is a topic for future research.

Appendix 3.A: Ground Motion Database

Table 3.6 Ground motion database.

Year	Earthquake	M[g](M$_w$)	Epi. Dis.(km)	Type	Station or ID	Soil[h]	PGA (g)	5-95% D$_s$(s)
1992[a]	Landers	7.3	86.0	Crustal	NGA900	D	0.15	18.9
1971[a]	San Fernando	6.6	39.5	Crustal	NGA68	D	0.17	11.2
1971[a]	San Fernando	6.6	39.5	Crustal	NGA68	D	0.21	10.5
1995[a]	Kobe, Japan	6.9	46.0	Crustal	NGA1116	E	0.21	11.8
1999[a]	Kocaeli, Turkey	7.5	53.7	Crustal	NGA1148	B	0.22	11.0
1979[a]	Imperial Valley	6.5	33.7	Crustal	NGA169	D	0.24	51.0
1995[a]	Kobe, Japan	6.9	46.0	Crustal	NGA1116	E	0.24	10.3
1999[a]	Hector Mine	7.1	26.5	Crustal	NGA1787	B	0.27	11.7
1992[a]	Landers	7.3	82.1	Crustal	NGA848	D	0.28	10.4
1987[a]	Superstition Hills	6.5	11.2	Crustal	NGA725	D	0.30	13.6
1999[a]	Kocaeli, Turkey	7.5	98.2	Crustal	NGA1158	D	0.31	11.8
1976[a]	Friuli, Italy	6.5	20.2	Crustal	NGA125	D	0.31	4.9
1999[a]	Hector Mine	7.1	26.5	Crustal	NGA1787	B	0.34	9.7
1979[a]	Imperial Valley	6.5	33.7	Crustal	NGA169	D	0.35	50.3
1976[a]	Friuli, Italy	6.5	20.2	Crustal	NGA125	D	0.35	4.2
1987[a]	Superstition Hills	6.5	35.8	Crustal	NGA721	D	0.36	16.0
1999[a]	Kocaeli, Turkey	7.5	98.2	Crustal	NGA1158	D	0.36	10.6
1979[a]	Imperial Valley	6.5	29.4	Crustal	NGA174	D	0.36	8.7
1992[a]	Cape Mendocino	7.0	22.7	Crustal	NGA829	C	0.39	15.3
1994[a]	Northridge	6.7	26.5	Crustal	NGA960	C	0.41	6.3
1994[a]	Northridge	6.7	13.3	Crustal	NGA953	A	0.42	9.2
1992[a]	Landers	7.3	82.1	Crustal	NGA848	D	0.42	8.2
1989[a]	Loma Prieta	6.9	9.8	Crustal	NGA752	B	0.44	13.2
1987[a]	Superstition Hills	6.5	11.2	Crustal	NGA725	D	0.45	13.8
1994[a]	Northridge	6.7	26.5	Crustal	NGA960	C	0.48	5.6
1990[a]	Manjil, Iran	7.4	40.4	Crustal	NGA1633	D	0.50	30.6
1995[a]	Kobe, Japan	6.9	8.7	Crustal	NGA1111	B	0.50	11.2
1995[a]	Kobe, Japan	6.9	8.7	Crustal	NGA1111	B	0.51	9.7
1999[a]	Chi-Chi, Taiwan	7.6	77.5	Crustal	NGA1485	B	0.51	10.8
1990[a]	Manjil, Iran	7.4	40.4	Crustal	NGA1633	D	0.51	28.9
1994[a]	Northridge	6.7	13.3	Crustal	NGA953	A	0.52	8.4
1989[a]	Loma Prieta	6.9	9.8	Crustal	NGA752	B	0.53	11.9
1992[a]	Cape Mendocino	7	22.7	Crustal	NGA829	C	0.55	10.9
1989[a]	Loma Prieta	6.9	31.4	Crustal	NGA767	D	0.56	6.4
1999[a]	Duzce, Turkey	7.1	41.3	Crustal	NGA1602	D	0.73	8.5
2001[b]	Nisqually	6.8	121.4	Subduction	20010228	-[i]	0.08	21.0
2001[b]	Nisqually	6.8	121.4	Subduction	20010228	C	0.06	21.3
2001[b]	El Salvador	7.6	92.43	Subduction	20010113	C	0.23	21.7
2001[b]	El Salvador	7.6	92.43	Subduction	20010113	C	0.25	25.8
1979[a]	St Elias, Alaska	7.54	26.46	Subduction	NGA1628	C	0.18	26.9
2004[c]	Southeast off Kii Peninsula, Japan	7.4	175.0	Subduction	NARH05	C	0.16	27.1
2007[b]	KM, Indonesia	7	142.7	Subduction	20070913	C	0.01	32.2
2007[b]	KM, Indonesia	7	142.7	Subduction	20070913	C	0.01	33.3
2003[c]	Tokachi Oki, Japan	8.3	156.0	Subduction	TKCH11	C	0.25	34.3
2005[c]	Off Miyagi prefecture, Japan	7.2	201.0	Subduction	IWTH02	C	0.20	34.9
1979[a]	St Elias, Alaska	7.54	26.5	Subduction	NGA1628	-[i]	0.10	35.5
2001[b]	El Salvador	7.6	70.0	Subduction	20010113	-[i]	0.14	35.7
1985[d]	Valparaiso, Chile	7.8	100.0	Subduction	Llaylay	C	0.35	35.9

Year	Earthquake	M[g](M$_w$)	Epi. Dis.(km)	Type	Station or ID	Soil[h]	PGA (g)	5-95% D$_s$(s)
2001[b]	El Salvador	7.6	70.0	Subduction	20010113	-[i]	0.12	37.3
2003[c]	Tokachi Oki, Japan	8.3	156.0	Subduction	HDKH06	C	0.21	38.9
2003[c]	Tokachi Oki, Japan	8.3	104.0	Subduction	HDKH07	C	0.18	39.0
1985[d]	Valparaiso, Chile	7.8	100.0	Subduction	Llaylay	C	0.47	39.2
2003[c]	Tokachi Oki, Japan	8.3	156.0	Subduction	HDKH06	C	0.19	39.4
2001[b]	Nisqually	6.8	85.8	Subduction	20010228	-[i]	0.07	40.0
2001[b]	Nisqually	6.8	85.8	Subduction	20010228	-[i]	0.09	40.5
2010[e]	Maule, Chile	8.8	334.2	Subduction	STL	C	0.24	40.7
2011[c]	Tohuku, Japan	9	277.0	Subduction	IBRH18	C	0.47	41.6
1985[d]	Michoacan, Mexico City	8	40.0	Subduction	NOAA	-[i]	0.12	42.1
1985[d]	Michoacan, Mexico City	8	40.0	Subduction	NOAA	-[i]	0.12	44.2
2011[c]	Tohuku, Japan	9	284.0	Subduction	IBRH15	C	0.65	44.6
2007[b]	Southern Sumatra, Indonesia Earthquake	8.4	392.2	Subduction	20070912	-[i]	0.04	44.9
2007[b]	Southern Sumatra, Indonesia Earthquake	8.4	392.2	Subduction	20070912	-[i]	0.04	46.7
2010[e]	Maule, Chile	8.8	209.3	Subduction	ANGO	D	0.70	49.8
2003[f]	Tokachi Oki	8	194.0	Subduction	HKD 125	C	0.05	50.1
2007[b]	KM, Indonesia Earthquake	7.9	164.6	Subduction	20070912	-[i]	0.13	50.3
2011[c]	Tohuku, Japan	9	282.0	Subduction	TCGH13	C	0.91	50.7
2010[e]	Maule, Chile	8.8	209.3	Subduction	ANGO	D	0.93	50.8
2011[c]	Tohuku, Japan	9	266.0	Subduction	FKSH10	C	0.78	52.1
2007[b]	KM, Indonesia Earthquake	7.9	164.6	Subduction	20070912	-[i]	0.12	52.9
2003[f]	Tokachi Oki	8	232.0	Subduction	HKD 124	C	0.05	54.5
2010[e]	Maule, Chile	8.8	136.0	Subduction	HUA	C	0.45	56.0
2011[c]	Tohuku, Japan	9	282.0	Subduction	TCGH13	C	0.58	60.5
2010[e]	Maule, Chile	8.8	136.0	Subduction	HUA	C	0.38	61.7
2010[e]	Maule, Chile	8.8	113.1	Subduction	TAL	C	0.47	69.9
2010[e]	Maule, Chile	8.8	113.1	Subduction	TAL	C	0.42	71.9
2011[c]	Tohuku, Japan	9	155.0	Subduction	IWTH27	C	0.74	79.7
2011[c]	Tohuku, Japan	9	155.0	Subduction	IWTH27	C	0.61	85.3
n/a[j]	Cascadia	9.2	446.8	Subduction	Seattle	B/C	0.16	132.3
n/a[j]	Cascadia	9.2	446.8	Subduction	Seattle	B/C	0.13	137.2
n/a[j]	Cascadia	9.2	481.3	Subduction	Seattle	B/C	0.05	162.2
n/a[j]	Cascadia	9.2	481.3	Subduction	Seattle	D/E	0.13	188
n/a[j]	Cascadia	9.2	446.8	Subduction	Seattle	D/E	0.16	196.7
n/a[j]	Cascadia	9.2	481.3	Subduction	Seattle	D/E	0.14	206
n/a[j]	Cascadia	9.2	446.8	Subduction	Seattle	D/E	0.18	230.1
n/a[j]	Cascadia	9.2	481.3	Subduction	Seattle	B/C	0.04	271.3
2004[k]	Sumatra–Andaman	9.3	-[i]	Simulated	-[i]	-[i]	0.14	59.0
2004[k]	Sumatra–Andaman	9.3	-[i]	Simulated	-[i]	-[i]	0.14	65.2
1964[l]	Prince William Sound, Alaska	9.2	-[i]	Simulated	-[i]	-[i]	0.25	151.8
1964[l]	Prince William Sound, Alaska	9.2	-[i]	Simulated	-[i]	-[i]	0.23	92.2
n/a[m]	Cascadia	9	-[i]	Simulated	Vancouver, Canada	C	0.11	118.5
n/a[m]	Cascadia	9	-[i]	Simulated	Vancouver, Canada	C	0.11	119.5
n/a[m]	Cascadia	9	-[i]	Simulated	Vancouver, Canada	C	0.1	85.8
n/a[m]	Cascadia	8.5	-[i]	Simulated	Vancouver, Canada	C	0.11	65.6

Year	Earthquake	M[g](M_w)	Epi. Dis.(km)	Type	Station or ID	Soil[h]	PGA (g)	5-95% D_s(s)
n/a[m]	Cascadia	8.5	-[i]	Simulated	Vancouver, Canada	C	0.1	49.6
n/a[m]	Cascadia	8.5	-[i]	Simulated	Vancouver, Canada	C	0.09	51.1
n/a[m]	Cascadia	9	-[i]	Simulated	Seattle	B/C	0.14	94.6
n/a[m]	Cascadia	9	-[i]	Simulated	Seattle	B/C	0.1	93.5
n/a[m]	Cascadia	9	-[i]	Simulated	Seattle	B/C	0.1	110
n/a[m]	Cascadia	8.5	-[i]	Simulated	Seattle	B/C	0.07	65.1
n/a[m]	Cascadia	8.5	-[i]	Simulated	Seattle	B/C	0.07	79.3
n/a[m]	Cascadia	8.5	-[i]	Simulated	Seattle	B/C	0.06	86.1
n/a[m]	Cascadia	9	-[i]	Simulated	Victoria, Canada	B/C	0.14	85.1
n/a[m]	Cascadia	9	-[i]	Simulated	Victoria, Canada	B/C	0.11	87.2
n/a[m]	Cascadia	9	-[i]	Simulated	Victoria, Canada	B/C	0.1	96.0
n/a[m]	Cascadia	8.5	-[i]	Simulated	Victoria, Canada	B/C	0.17	52.1
n/a[m]	Cascadia	8.5	-[i]	Simulated	Victoria, Canada	B/C	0.11	53.1
n/a[m]	Cascadia	8.5	-[i]	Simulated	Victoria, Canada	B/C	0.1	70.9

[a] Database: PEER Next Generation Attenuation (NGA) database (PEER 2012).
[b] Database: USGS National Strong-Motion Project (USGS 2012b).
[c] Database: Kyoshin Network (K-NET 2012).
[d] Database: NOAA, National Geophysical Data Center (NOAA 2012).
[e] Database: Center for Engineering Strong Motion Data (CESMD 2012).
[f] K-Net ground motions from (Atkinson and Macias 2009).
[g] Earthquake Magnitude.
[h] NEHRP Soil Classification (ASCE 2010).
[i] Data not available.
[j] Simulated Ground Motions – Cascadia (Caltech 2011; Yang 2009).
[k] Simulated Ground Motions – Indonesia (Sørensen *et al.* 2007).
[l] Simulated Ground Motions – Alaska (Mavroeidis *et al.* 2008).
[m] Simulated Ground Motions – Cascadia (Atkinson and Macias 2009).

Appendix 3.B: Seismic Design History for Seattle, Portland and Los Angeles

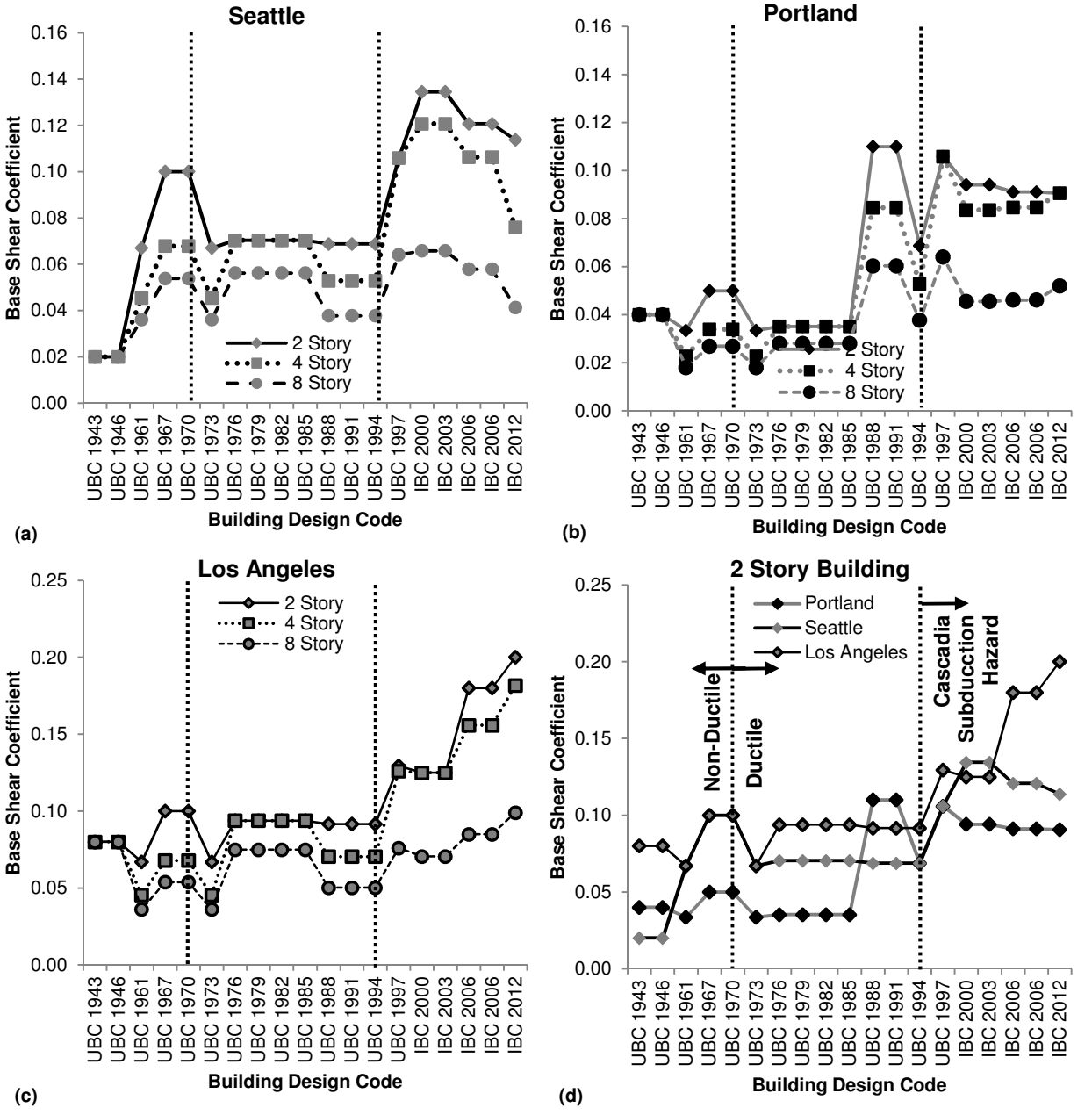

Figure 3.15 Seismic design base shear coefficient values illustrating variations across years for Seattle, Washington, Portland, Oregon and Los Angeles, California.

CHAPTER 4 PHYSICAL DAMAGE INDICATORS FOR AFTERSHOCK COLLAPSE VULNERABILITY ASSESSMENT

4.1 Introduction

Major earthquakes, or "mainshocks", are typically followed by smaller magnitude earthquakes known as "aftershocks", which originate at or near the rupture zone of the larger earthquakes (USGS 2012a). Smaller earthquakes known as foreshocks also sometimes occur before the mainshock, originating around the same location. For example, the Tohuku (M_w 9, 2011), Japan earthquake was preceded by around 20 foreshocks with $M_w > 5$ and followed by several hundred aftershocks, as show in Figure 4.1. Around 30 of these aftershocks had M_w greater than 6 and one had M_w of 7.9 (USGS 2012a). According to Omori's law, aftershocks can occur over a long period of time following the mainshock, although their frequency decreases exponentially with time (Reasenberg and Jones 1989, 1994). As a result of these phenomena, buildings can be exposed to a sequence of multiple earthquakes, with typically no time for repair between the seismic events. In addition, the potential for structural damage during an aftershock is increased because the building may be already damaged by the mainshock. In the U.S. alone, there are several documented cases of aftershock damage to mainshock-damaged buildings, such as after the Northridge (M_w 6.7, 1994) and Kern County (M_w 7.3, 1952) earthquakes (McDonald *et al.* 2000). From a public safety perspective, it is therefore important to quickly assess the integrity of buildings following a major earthquake, to avoid people entering unsafe buildings and to identify buildings that will require repair for the long-term safety of the occupants.

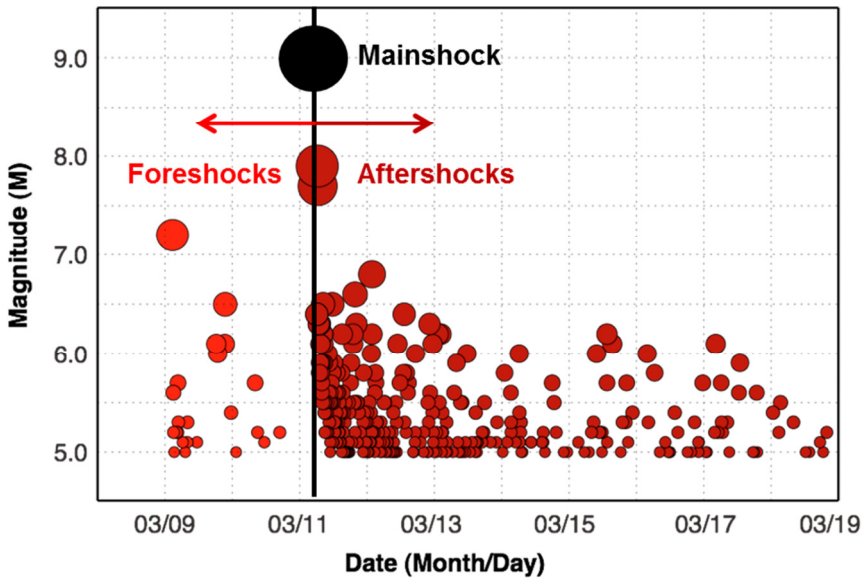

Figure 4.1 Foreshocks and aftershocks (first 8 days) associated with the Tohuku (M_w 9, 2011), Japan earthquake (Hayes and Wald 2011).

This study describes and exercises a probabilistic methodology to quantify building fragility to earthquake-induced damage and collapse considering earthquake sequences. The methodology is applied to a portfolio of reinforced concrete frame buildings, accounting for the variability of damage possible in mainshock and aftershock events. The four reinforced concrete frame buildings examined are designed and detailed according to current building codes, such that they are representative of modern U.S. construction. The response of each building is simulated with a nonlinear MDOF model, which is capable of capturing the critical aspects of strength and stiffness degradation of the building as the damage progresses, potentially leading to collapse. To quantify aftershock damage, the building models are subjected to a large number of earthquake mainshock-aftershock sequences and the structural response is recorded throughout the sequence to quantify the damage experienced by the structure due to mainshock and aftershock. The aftershock building fragilities, representing the probability of experiencing a specified level of damage, are conditioned on the level of mainshock damage. Mainshock structural damage is quantified by a variety of physical damage indicators: maximum drifts

(interstory and roof), residual drifts (interstory and roof) and failures of beams and columns. Results of the aftershock fragility assessment are then used to examine the relationship between the mainshock physical damage indicators and the capacity of the building to withstand subsequent shaking. The quantification of damage to buildings in earthquake sequences can equip us with the tools to mitigate the damage to the life and property as a result of better understanding of the building response and the building fragility in these events. Also, the relationship between physical damage observed in the structure and subsequent reduction in the collapse capacity due to that damage further helps in providing insight into the superiority of certain physical damage indicators in identifying buildings that pose a significant life safety risk.

4.2 Background

4.2.1 Analytical Studies of Aftershocks

A number of researchers have assessed the influence of earthquake sequences on the seismic response of buildings. For example, studies employing single-degree-of-freedom (SDOF) systems (Amadio *et al.* 2003; Hatzigeorgiou and Beskos 2009; Hatzigeorgiou 2010; Mahin 1980; Sunasaka and Kiremidjian 1993) found the earthquake sequences lead to higher structural damage and responses compared to a single earthquake. Mahin (1980) carried out one of the initial studies to assess the influence of aftershocks on structural response. Mahin (1980) examined the response of an elastic-perfectly plastic SDOF oscillator to ground motion recordings from the 1972 Managua, Nicaragua earthquake and two aftershocks, finding that the ductility and energy dissipation demands were increased during the combined event compared to the mainshock alone. More recently, Hatzigeorgiou and Beskos (2009) conducted a large set of analyses on elastic-plastic SDOFs, subjecting them to mainshock-aftershock sequences. They concluded that seismic sequences result in higher inelastic displacements of the SDOFs, as

compared to individual earthquake events. Building on the previous study, Hatzigeorgiou (2010) quantified ductility demand for several inelastic SDOF systems under ground motion sequences, finding that damage is greater than expected for a given design ground motion level if the possibility of earthquake sequences is considered.

More complex multiple-degree-of-freedom (MDOF) models have also been employed by a number of researchers (Fragiacomo *et al.* 2004; Hatzigeorgiou and Liolios 2010; Lee and Foutch 2004; Li and Ellingwood 2007; Ruiz-García and Negrete-Manriquez 2011; Ruiz-García *et al.* 2008). Nonlinear analysis of eight reinforced concrete frames by Hatzigeorgiou and Liolios (2010) under repeated earthquake sequences found more damage accumulation and higher structural responses in all the buildings when they were subjected to an earthquake sequence compared to a single event. The researchers also observed collapse of structures when subjected to earthquake sequences where separate events with intensity same as the sequence did not cause collapse alone.

Recent research work has indicated several efforts to develop procedures to quantify probabilistically, the increased fragility of buildings already damaged by a mainshock. Luco *et al.* (2004) computed the residual capacity of the mainshock-damaged building based on the intensity of the aftershock ground motion causing damage or collapse. Ryu *et al.* (2011) extended this approach to consider uncertainty in the definition of mainshock damage states. These methodologies have been applied to MDOF and equivalent SDOFs for a number of buildings(Raghunandan et al. 2012; Uma et al. 2011). Recently, Nazari et al. (2013) developed a quantifiable aftershock collapse probability criterion for woodframe buildings based on seismic response of the buildings using incremental dynamic analysis.

4.2.2 Post-earthquake Building Safety Assessments

Post-earthquake safety guidelines provide means and procedures to evaluate post-earthquake safety of structures as quickly and efficiently as possible. Many of these are based on the document that is extensively followed in the U.S.: ATC-20 (ATC 1989, 1995). In ATC-20, inspectors visually assess buildings after an earthquake, assigning each building one of the three tags: (i) *green* tag or INPECTED, indicating the building is safe to occupy and use; (ii) *yellow* tag or RESTRICTED USE, indicating limited use of the building post-earthquake due to possible dangerous conditions or may need further detailed evaluation; and (iii) *red* tag or UNSAFE, indicating the building is unsafe to occupy. For instance, a building will be tagged red if it is noticeably leaning. The rapid visual inspection of each building is expected to take around 10-20 minutes.

ATC-20 has been used extensively in the U.S. and elsewhere, including for major earthquakes in California such as Loma Prieta (M_w 6.9, 1989), Landers (M_w 7.3, 1992) and Northridge (M_w 6.7, 1994)(ATC 1995). After the 1994 Northridge earthquake, a total of 66,546 buildings were inspected, with around 23% of them were *yellow* or *red* tagged (EQE International 1994). More recently, a Hawaiian earthquake (M_w 6.7, 2006) required the post-earthquake assessment of around 1700 homes (Chock *et al.* 2006).

A small body of previous research has focused on examining post-earthquake building tagging procedures. Yeo and Cornell (2004) proposed a methodology for aftershock building tagging, which required convolving the aftershock ground motion hazard at a site with the probabilistic representation of the residual capacity of the structure at that site. Maffei *et al.* (2008) summarized possible building tagging criteria based on building's capacity to withstand future earthquakes and the probability of collapse of the structure. Note that both of these studies

relating to building tagging criteria have used the tagging terminology from ATC-20 (*i.e., red*, *yellow* and *green*), but define a set of tagging criteria that are wholly distinct from those used ATC-20's visual evaluations.

4.3 Archetypical Buildings and Building Models

Four archetypical reinforced concrete frame structures of varying height are considered in this study, as summarized in Table 4.1. These frames are designed and detailed as "special" moment resisting frames according to present U.S. seismic design codes (ASCE 2005; ACI 2002) to represent the modern low-rise, mid-rise and high-rise building infrastructure of California. These buildings are designed such that all frame lines (interior and exterior) of the building resist lateral loading (space frames). To ensure that brittle failure modes are avoided under earthquake loading, special moment resisting frames are subject to mandatory incorporation of certain design and detailing requirements including: strong-column-weak-beam design, shear capacity design and extensive detailing requirements. Although modern building codes attempt to ensure that newly-designed buildings have less than 1% probability of collapse in 50 years (Luco *et al.* 2007), damage to structural elements of such buildings may occur in moderate to large magnitude earthquake (Ramirez *et al*. 2012), making the structures potentially more vulnerable in an aftershock.

The archetypical buildings are modeled as two dimensional, three bay frames with different heights depending on the number of stories (Figure 4.2). The analytical modeling is carried out in *OpenSees* (2012). In the models used in this study, the flexural behavior of the beams, columns and joints are captured using lumped plasticity beam-column elements and elastic joint shear springs. The plastic hinges are modeled using a hysteretic material capable of capturing strength and stiffness deterioration developed by Ibarra *et al.* (2005). The flexural

modeling properties of the plastic hinge, such as plastic rotation capacity, yield moment capacity, post-peak stiffness are calculated with empirical equations developed by Haselton *et al.* (2008) using the experimental results from more than 250 columns. Figure 4.3(a) illustrates the monotonic behavior of a typical beam-column plastic hinge highlighting the negative stiffness region of the post peak response, which captures the strain softening behavior observed in reinforced concrete columns due to physical damage such as concrete spalling, rebar buckling and fracture, and bond failure. Figure 4.3(b) shows the cyclic behavior of a column modeled using Ibarra *et al.* (2005) material, illustrating the cyclic deterioration based on the energy dissipation capacity. Shear capacity design and extensive detailing requirements in modern design codes prevent shear and axial failure of columns. For this reason, these failure modes are not captured in the analytical models. Buildings are assumed to have flexible foundations, modeled with a semi-rigid rotational spring at the base of each column is calculated based on typical grade beam design and soil stiffness properties. Additional documentation of building design and modeling can be found in Haselton *et al.* (2011).

Table 4.1 Design Information for Archetype Buildings

ID[a]	T_1 [b] (s)	Design Base Shear Coefficient [c]	μ_T [d]
02MS	0.60	0.125	15.9
04MS	0.91	0.092	12.4
08MS	1.81	0.050	7.7
12MS	2.15	0.044	7.3

[a] Building information provided in ID: First two characters indicate the number of stories; third character "M" denotes modern design; last character indicates "S" for space frame and "P" for perimeter frame.
[b] First-mode elastic (fundamental) structural period based on eigenvalue analysis, considering cracked concrete sections.
[c] Ratio of the design base shear to the building weight (V_{design}/W).
[d] Period-based ductility capacity as determined by nonlinear static pushover analysis.

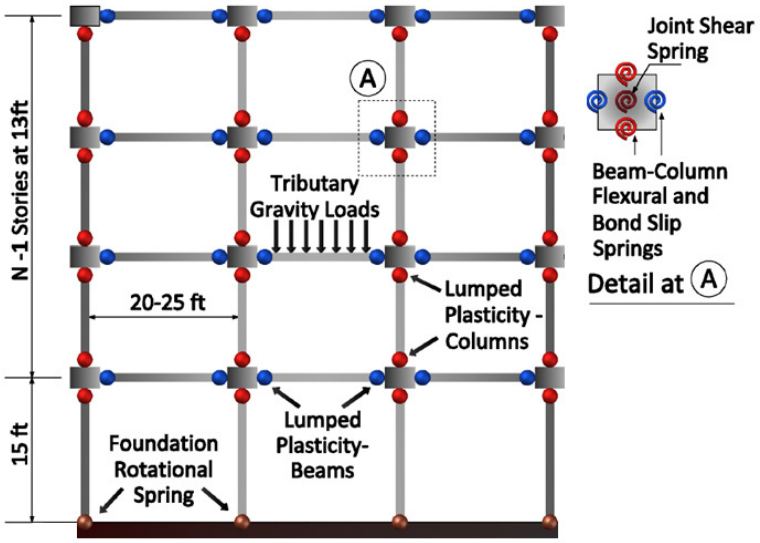

Figure 4.2 Modeling details for N story building model for dynamic analysis (Raghunandan and Liel 2013).

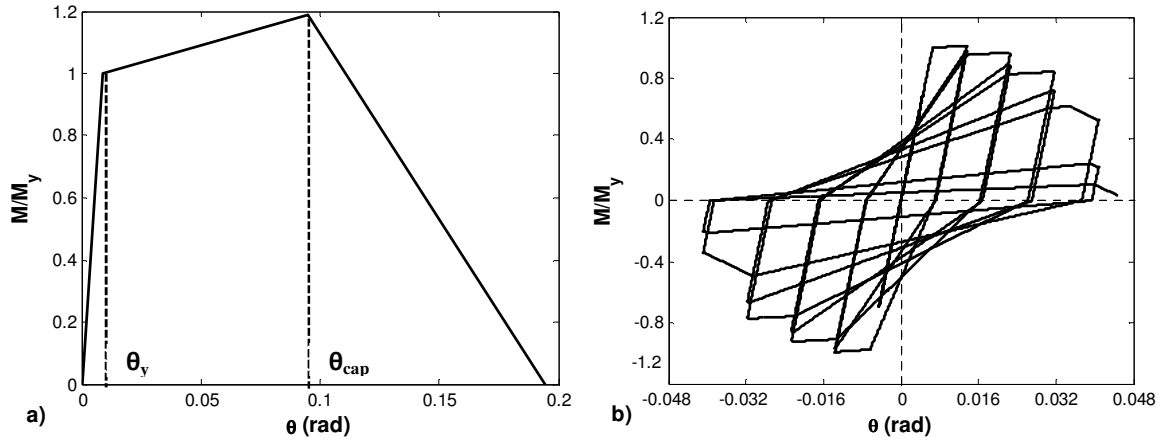

Figure 4.3 Illustration of typical ductile reinforced concrete column behavior under (a) monotonic and (b) cyclic loading (Liel *et al.* 2011).

4.4 Nonlinear Dynamic Analysis

4.4.1 Ground Motions

Mainshock-aftershock sequences for this analysis are generated using a set of 30 ground motions from Vamvatsikos and Cornell (2006) that are applied as both mainshocks and aftershocks, as described in more detail below. These 30 ground motions are recorded from California crustal earthquakes with M_w between 6.5 and 6.9 and at firm sites with closest distance to fault rupture between 15 and 33 km. The unscaled records have peak ground

accelerations from 0.04 to 0.63g. Ground motion intensity is measured using inelastic spectral displacement at the fundamental period of the structure, denoted S_{di} (Tothong and Cornell, 2006). Inelastic spectral displacement is defined as the peak displacement of a single degree of freedom (SDOF) bilinear oscillator when subjected to the ground motion of interest. The SDOF oscillator is assumed to have the same period as the fundamental period of the building of interest, 5% damping, 5% post-yield hardening stiffness and a yield displacement that is estimated based on the nonlinear pushover results of the MDOF building model (FEMA 2009). S_{di} is a simple ground motion intensity measure that accounts not only for the ground motion intensity at the first-mode period, but also ground motion intensities at longer periods, due to the period elongation of the inelastic oscillator. Tothong and Luco (2007) have shown that the use of S_{di} as a measure of ground motion intensity substantially reduces biases associated with record scaling on spectral response.

4.4.2 Mainshock Incremental Dynamic Analysis

To quantify the response of the building in the event of an earthquake or a sequence of earthquakes, incremental dynamic analysis (IDA) is carried out. In IDA, a nonlinear building model is subjected to a ground motion having a particular intensity (quantified in terms of S_{di}), and its response is recorded, including demand parameters such as maximum interstory drifts, maximum residual drifts or roof drifts (Vamvatsikos and Cornell, 2002). In subsequent analyses, the ground motion is scaled to a larger intensity and the nonlinear dynamic response is recorded again. The process of repeated scaling of ground motions and dynamic analysis is continued until the structure collapses, which is indicated by dynamic instability (*i.e.,* very large interstory drifts or sidesway collapse). The incremental dynamic analysis process provides insights about structural behavior under rare, high-intensity ground shaking, for which few recordings are

available. To account for the effect of record-to-record variability on structural response, IDA is repeated for each of the 30 ground motions in the set.

To quantify structural response of intact building, IDA is carried out on the nonlinear model of the undamaged buildings. The IDA results for 4 story modern building is illustrated in Figure 4.4(a) and the bold (black) line highlights IDA results from one (of 30) ground motions. The IDA is run with closely spaced scale factors in order to achieve a good estimate of the ground motion intensity and structural response during the mainshock. For most of the ground motions, IDA shows an increase in structural response (maximum interstory drift) with increase in ground motion intensity (S_{di}). However, in some cases the opposite occurs. These "resurrecting records" cause lower levels of damage at higher intensities due to occurrence of different failure modes at different levels of excitation to a structure (Vamvatsikos and Cornell 2002).

Mainshock incremental dynamic analysis is carried out to determine the scale factor by which each ground motion must be scaled to make building reach any a particular damage state defined in terms of structural damage measure, maximum interstory drift. These damage states are used for determining aftershock building fragility curves conditioned on mainshock damage and are discussed in detail in section 4.5.1. Due to differences in frequency content, duration and other ground motion characteristics, each ground motion needs to be scaled to a different intensity before a particular value of maximum interstory drift occurs in the structure. For example, depending on the ground motion, the 4 building reaches a maximum interstory drift of 0.5% at S_{di} levels between 1.3 and 2 inches. For the same building, the ground motion intensities vary in a larger range (S_{di} of 5.4 to 15.5 inches) to produce a higher maximum interstory drift of 5.5%.

It is also difficult to determine the exact scale factors for each ground motion that will cause the exact maximum interstory drift for each damage state from mainshock analysis. The scale factors for each maximum interstory drift in mainshock for each ground motion were therefore calculated using linear interpolation between the scale factors for closest maximum interstory drift levels. Due to use of estimated scale factors, when the ground motion is scaled to a particular maximum interstory drift, there is slight variation in the values of actual observed maximum interstory drifts as compared to the deterministic target value (Figure 4.4(b)). This variation is less for lower damage states because the response of the structure is more linear at low drift levels. As the structural behavior becomes more nonlinear, the range of drifts increases but the median value from the IDA results closely matches the deterministic drift targets.

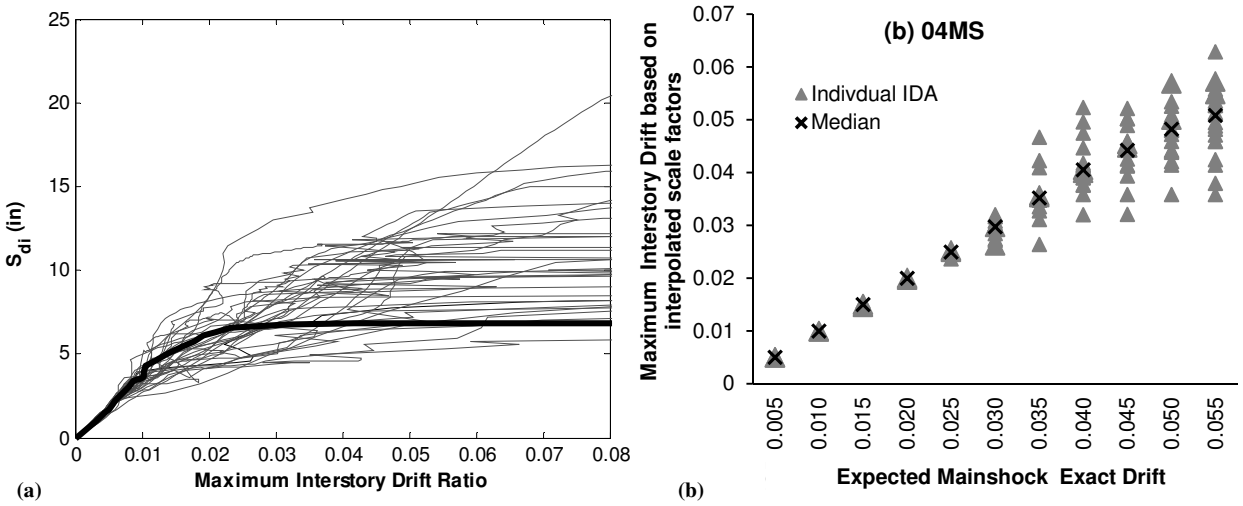

Figure 4.4 (a) Incremental dynamic analysis results of a 4 story intact ductile building (04MS) and, (b) Variation of maximum interstory drift level in dynamic analysis for 04MS for each mainshock damage state, due to interpolated scale factors.

Similarly, for each damage state defined by a particular maximum interstory drift level, the structural response quantified using other damage measures also vary for the particular damage state (*e.g.* Figure 4.5 for the 4 story modern building). In spite of the scatter, on average, there is an increase in the damage measures from least damaged to most damaged for all the buildings (for 04MS building, refer Figure 4.5)

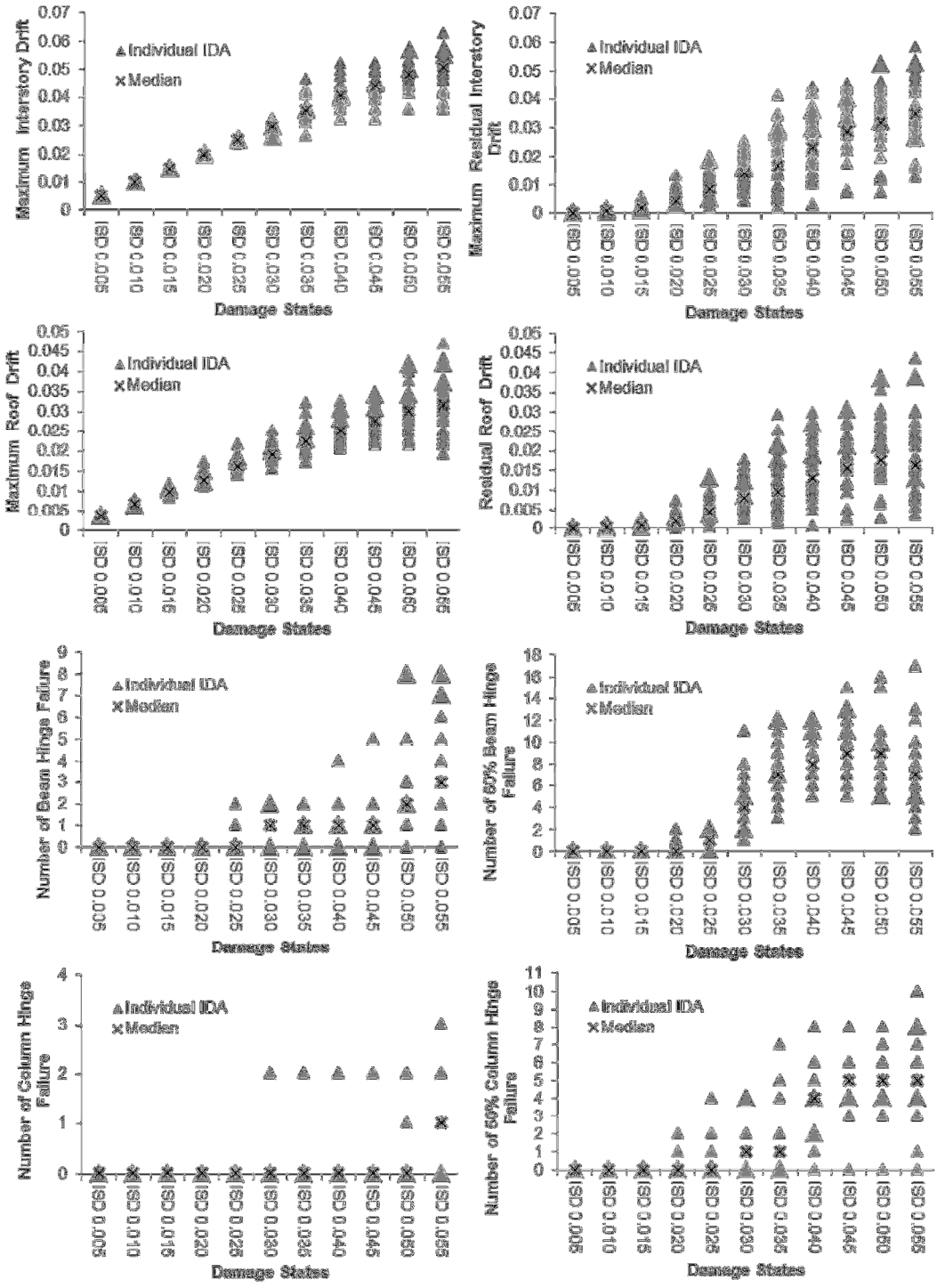

Figure 4.5 Variation of physical damage indicators for mainshock damaged building for different damage states for a 4 story building (04MS).

4.4.3 Aftershock Incremental Dynamic Analysis

In aftershock analysis, the building is subjected to a mainshock-aftershock sequence, as shown in Figure 4.6. The mainshock record is scaled, the level of response in the structure is recorded and, subsequently, an aftershock record is applied to the mainshock-damaged structure. In this study, the mainshock records are scaled by a specific scale factors calculated in section 4.4.2 corresponding to different mainshock damage states. A rest period of four seconds is added between the motions to recreate the realistic situation in which the structure comes to rest, but is not repaired. The aftershock analysis is conducted with increasing scale factors on aftershock ground motion until that aftershock record causes the collapse of the building.

In this study, 900 artificial mainshock-aftershock sequences are created by combining each of the 30 mainshock ground motions with the same 30 ground motions applied as aftershocks. Ruiz-García and Negrete-Manriquez (2011) saw weak correlation in the frequency content of mainshock and aftershock ground motions in 64 sequences recorded from Northridge (M_w 6.7, 1994) and Mammoth Lakes (M_w 6.2, 1980) earthquakes. Therefore,the large number of earthquake sequences consisting of different mainshock and aftershock ground motions is intended to represent the variability in real mainshock and aftershock frequency content and duration.

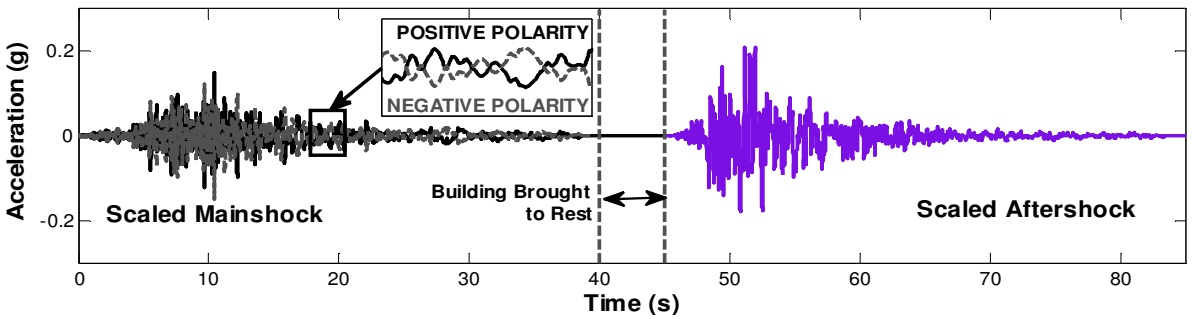

Figure 4.6 A mainshock-aftershock sequence for analysis of damaged building.

During aftershock analysis, the polarity of aftershock with respect to mainshock becomes important for cases where the residual drift after a mainshock is high (*i.e.* the structure is leaning to one side or another). The term "polarity" refers to the directions of the aftershock and mainshock, and specifically whether the aftershock tends to amplify or reduce mainshock residual drift (Luco *et al.* 2004). There are several ways to address this situation: (a) apply the aftershock separately in both polarities to generate two aftershock sequences and quantify the collapse capacity for the sequence based on the aftershock polarity that results in the lower capacity (or is more damaging), and (b) apply a random polarity of the aftershock ground motion. For a conservative estimate of aftershock probability, the best option is (a), but this approach is computationally intensive. Using option (b) for some levels of mainshock damage for the 4 story modern building indicated that the median aftershock collapse capacity is 5-10% higher capacities than using option (a) based on 900 ground motion sequences. In this study, the polarity of the aftershock is treated randomly to represent the realistic scenario in which the polarity of aftershock with respect to mainshock is random and unknown.

4.4.4 Computational Challenges

In total, IDA is carried out on approximately 9900 ground motion sequences per building (900 sequences, with 11 different scale factors applied on mainshock records). This process is computationally intensive, requiring use of the parallel version of *OpenSeesMP* on the Janus supercomputer at University of Colorado at Boulder. Running the analysis on 900 processors in parallel reduces the computational time for each building to about 24 hours as compared to 11 weeks on a desktop computer with 8 processors.

4.5 Assessments of Aftershock Fragility for Mainshock-Damaged Buildings

4.5.1 Definition of Damage States

The aftershock IDA is used to determine the collapse capacity of the mainshock-damaged building, which is quantified by the intensity of the aftershock ground motion (quantified in terms of S_{di}) causing collapse. These results depend on the level of damage the building experienced in the mainshock. For this purpose, building damage can be described by qualitative and quantitative descriptions of discrete damage states. Raghunandan *et al.* (2012) used qualitative definitions of damage states, associating the physical response of the building with certain damage state, wherein, for example, the "slight" damage state corresponds to yielding of beams at one floor and the "extensive" damage state corresponds to failure of at least one beam or column element. In this study, quantitative damage states are defined based on the damage measure maximum interstory drift experienced by the building during the mainshock. Maximum interstory drift ratio is chosen as the damage state definition because the global collapse state of the structure in this study is also defined in terms of the same variable (corresponding to sidesway collapse), although the use of other damage measures is also possible.

Nonlinear static pushover analysis in Figure 4.7 of the analytical building models is used to illustrate the range of mainshock damage examined. 11 damage states corresponding to maximum interstory drift ratios in mainshock of 0.5% (ISD 0.005) to 5.5% (ISD 0.055) that are 0.5% apart are chosen for the 4, 8 and 12 story buildings. Since pushover analysis indicated a higher deformation capacity for the 2 story building, damage states ranging from 1.5% interstory drift (ISD 0.015) to 6.5% interstory drift (ISD 0.065) were examined in order to observe structural response at higher drift levels. The elimination of lower damage states for the 2 story building should not affect the results of this study because it is observed that that for lower

damage states (with lower drift levels), the median collapse capacity of the intact and damaged building stay same (Raghunandan *et al.* 2012).

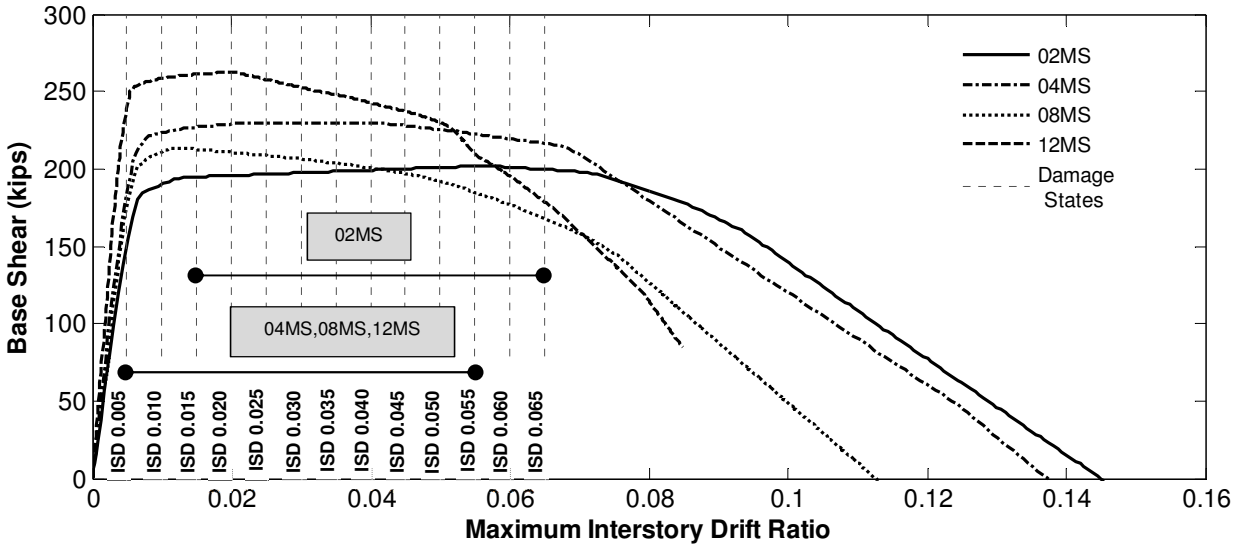

Figure 4.7 Nonlinear pushover analysis results for the four buildings showing differentmainshock damage states defined using maximum interstory drift ratio (ISD).

4.5.2 Aftershock IDA Results for Aftershock Fragility Assessment

The results obtained from IDA of the mainshock-damaged building is shown in Figure 4.8, where the *x*-axis represents the maximum interstory drift ratio experienced by the structure during the aftershock (second ground motion in sequence). Results shown in Figure 4.8 (a,b) are for a building that experienced relatively low damage in the mainshock (mainshock ISD 0.010); in Figure 4.8 (c,d) the building has been more extensively damaged in the mainshock (mainshock ISD 0.030). The thick black line indicates the IDA results from a particular mainshock-aftershock sequence. In the region shaded in grey, the interstory drifts experienced by the structure during the aftershock are smaller than those experienced in the mainshock because of the lower intensity of ground motions. This shaded region essentially indicates the range of aftershock response within which the condition of the already damaged building does not worsen and therefore are not considered in aftershock damage and collapse fragility calculations.

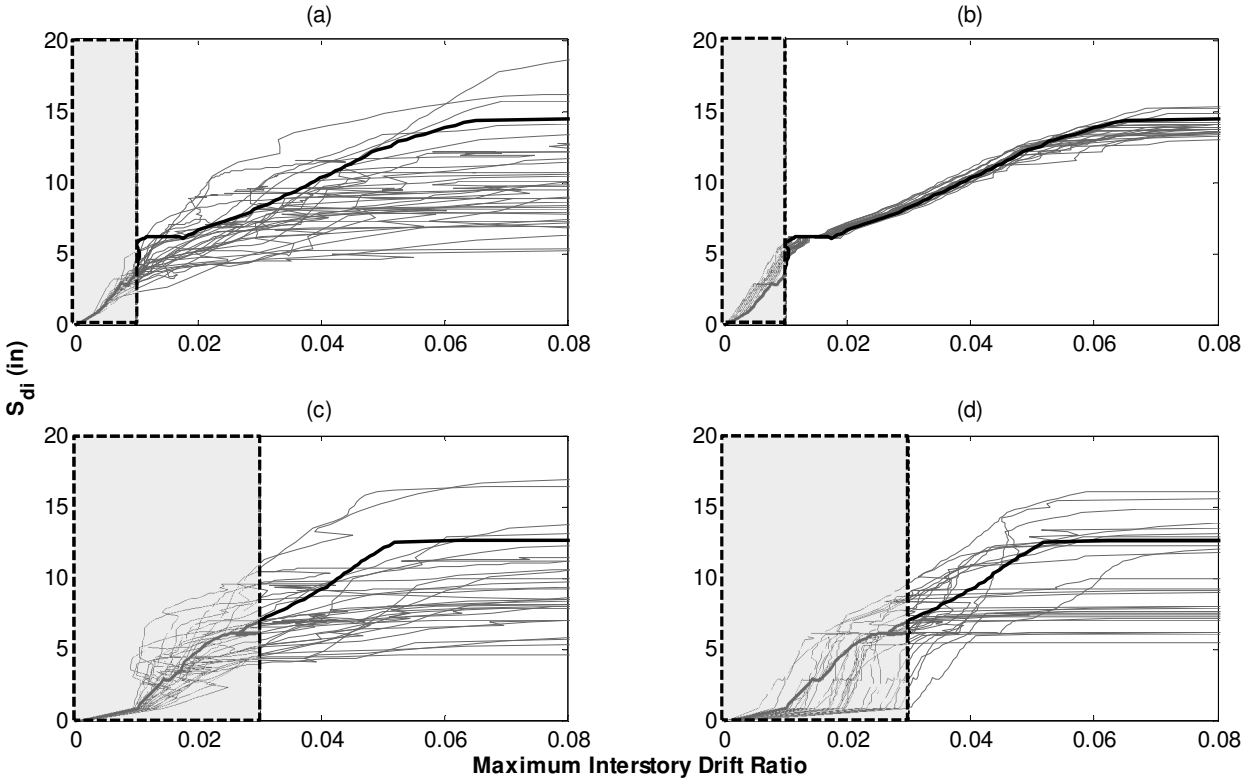

Figure 4.8 Incremental dynamic analysis results for 4 story building (04MS) in which 30 different aftershock records are applied after experiencing either (a) ISD 0.010 or (c) ISD 0.030 damage state in the same mainshock record; (b) and (d) show the behavior of the building in ISD 0.010 and ISD 0.030 damaged states, respectively, when subjected to sequences consisting of 30 different mainshock records, but the same aftershock record.

Figure 4.8 shows that there is significant scatter in the intensity levels at which a particular damage state occurs for different aftershock records after the same mainshock record (Figure 4.8(a,c)). However, when the mainshock records are different, but the aftershock record is same (Figure 4.8(b,d)), the building exhibits similar behavior in the aftershock. This observation indicates that the history of the path to the mainshock state is less important than the level of the building damage. However in Figure 4.8(d), there is a larger variability in building response to the same aftershock after different mainshocks as compared to Figure 4.8(c). This indicates that as mainshock damage becomes more severe, path dependencies become more important, due to the increasing nonlinear behavior.

4.5.3 Aftershock Collapse Fragility Curves

Based on the IDA results obtained for the mainshock-aftershock sequences, the collapse capacities of the mainshock-damaged buildings are computed and represented by a collapse fragility function, which assumes collapse capacities are lognormally distributed. For the intact buildings, the collapse fragility function is evaluated based on IDA of the modeled intact building using 30 ground motions. For the damaged buildings, the collapse fragility function for each damage state is calculated based on lognormal distribution of the 900 aftershock collapse capacities obtained for the mainshock-aftershock sequences in which the mainshock damage corresponds to the damage state of interest. A building's collapse fragility curve can be quantified using two parameters, (1) the median collapse capacity of the building, which is the S_{di} level at which the probability of collapse is 0.50, and (2) the lognormal standard deviation of the collapse fragility curve, which quantifies the dispersion (variability) in the predicted collapse capacity.

Figure 4.9 illustrates the collapse fragility functions for the intact and mainshock-damaged 4 story modern buildings, showing probability of collapse as a function of ground shaking intensity. The intact building (black solid line) is the least fragile building, in that has the least probability of collapse for a given level ground shaking intensity. As the building becomes more and more damaged in mainshock, it is increasingly fragile, as is indicated by the shift of the collapse fragility curves of damaged buildings to the left. The level of shift also indicates the order of reduction of collapse fragility associated with the mainshock damage. For example, the fragility curve for mainshock damage level of ISD 0.005 follows the fragility curve for intact building very closely. On the contrary, the most damaging mainshock state (ISD 0.055) has a

drastic shift from the intact building fragility curve, demonstrating a severe reduction in collapse capacity of the damaged building.

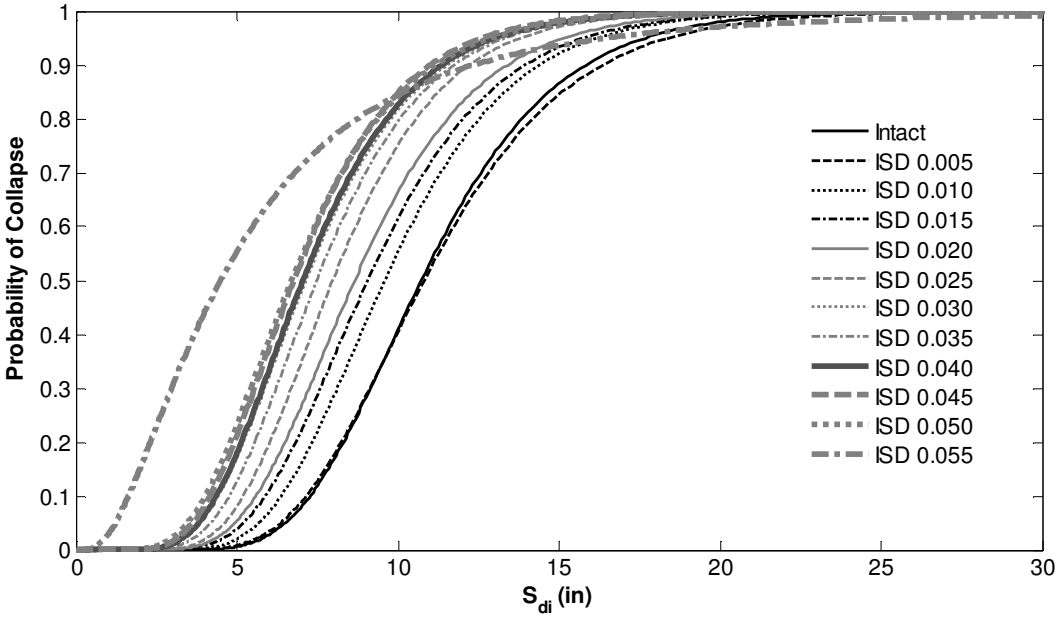

Figure 4.9 Collapse fragility curves for the 4 story modern building, showing shift in collapse fragility as a function of mainshock damage (quantified by ISD 0.005-ISD 0.055).

Figure 4.10 and Figure 4.11 summarize the variation of median collapse capacity and lognormal standard deviation respectively for collapse fragility curves corresponding to intact and damaged buildings. According to Figure 4.10, the (median) collapse capacity of the building to resist an aftershock decreases as the building is increasingly damaged in the mainshock. At lower damage states, there is not much variation in the collapse capacity of damaged building, showing that low levels of mainshock damage do not substantially affect the aftershock collapse risk of the structure. However, as the level of mainshock damage increases, the aftershock collapse capacity becomes more distinct from the intact building. For the 2, 4, 8 and 12 story buildings, there is 54, 58, 55 and 62% decrease in collapse capacity between the intact building and the worst mainshock damage state. Figure 4.11 shows that there is not much variation in the lognormal standard deviation of the collapse fragility functions, except for buildings highly

damaged in mainshock. The increased dispersion for the more damaged buildings can be explained based on higher nonlinear behavior of the damaged building model. The more nonlinear the building response is, the more it is sensitive to the damage path in the sequence, i.e. the mainshock and aftershock combination leading to collapse.

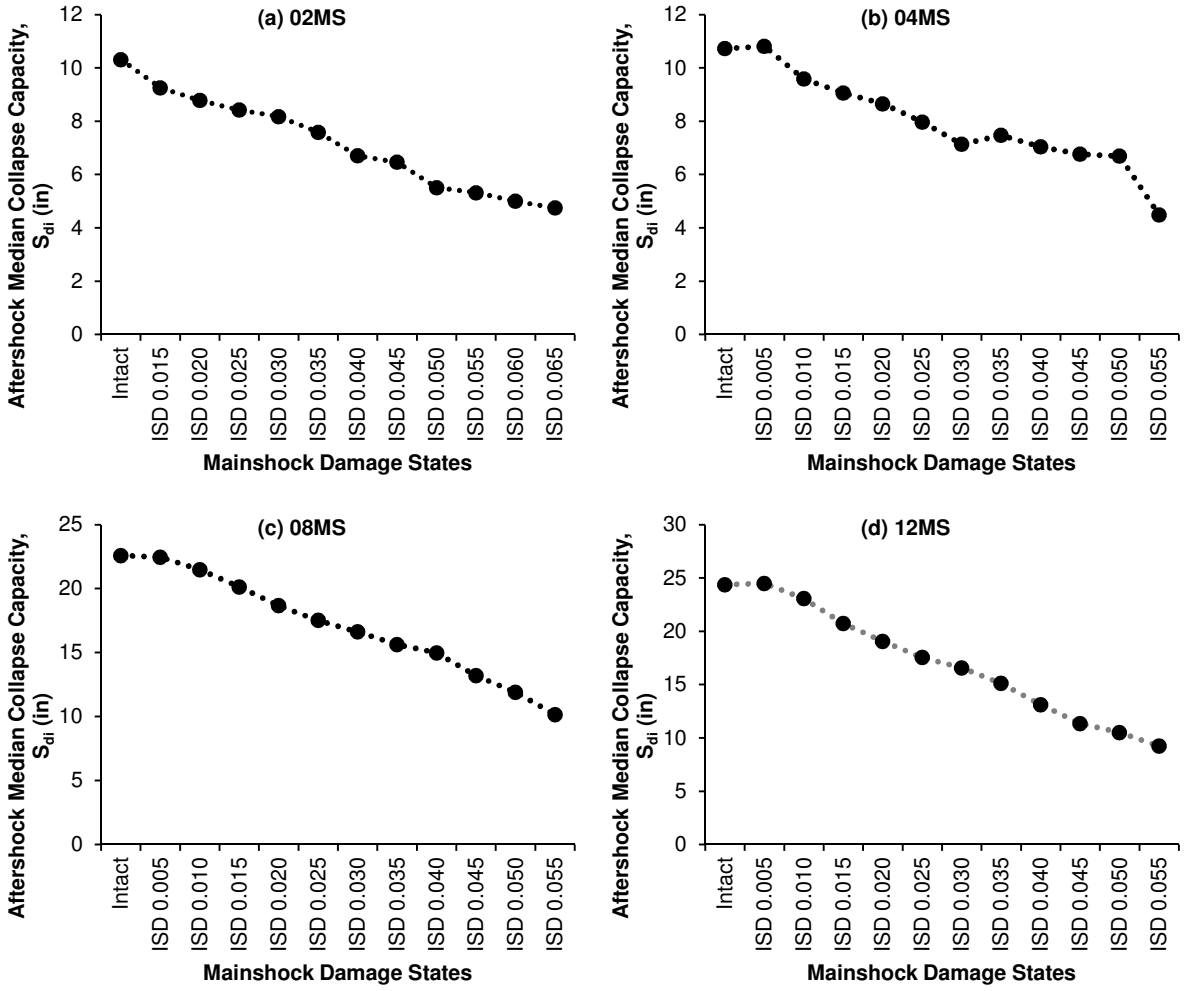

Figure 4.10 Variation in median aftershock collapse capacity (S_{di}, in) for modern 2, 4, 8 and 12 story having experienced varying levels of damage in mainshock.

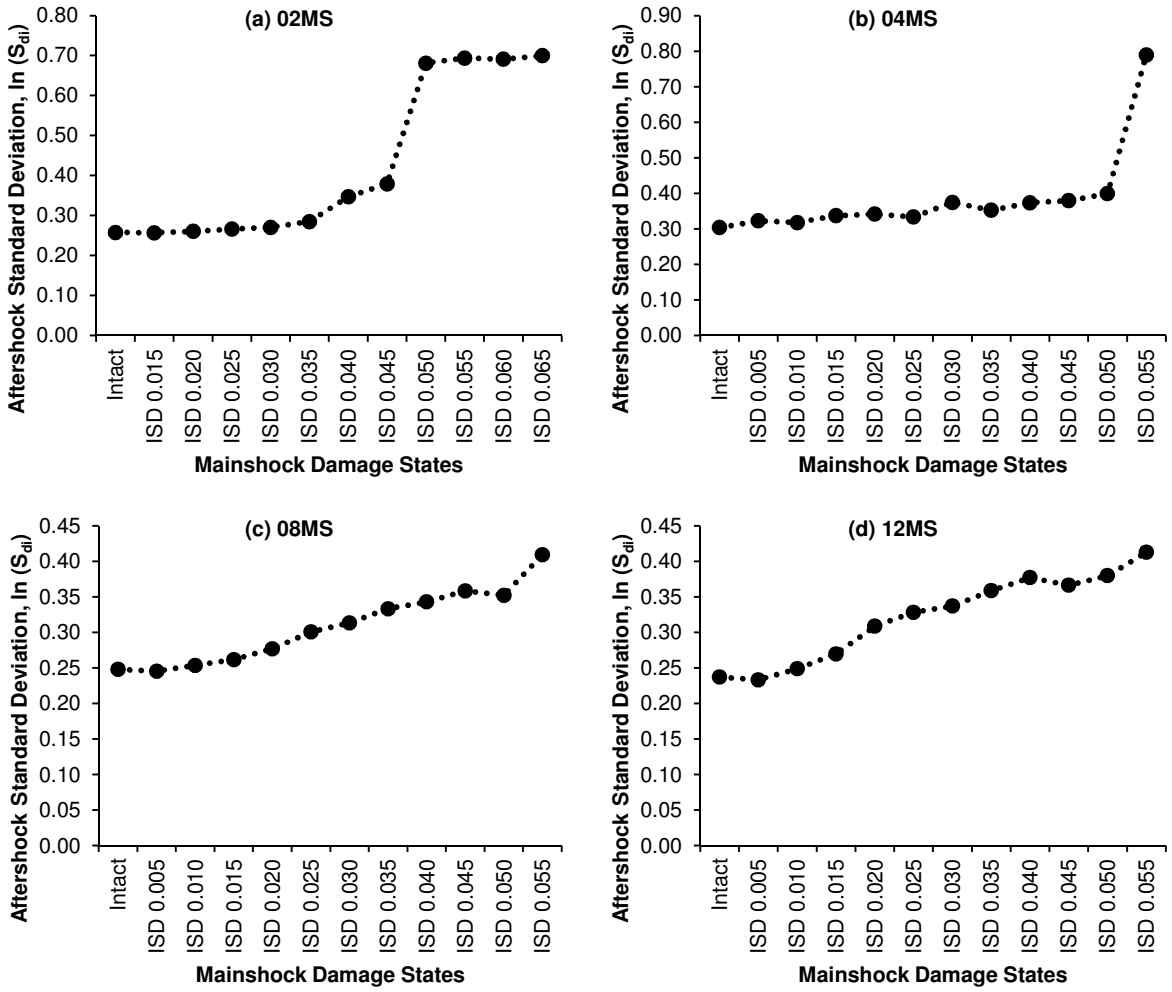

Figure 4.11 Variation in lognormal standard deviation, ln(S_{di}), of collapse fragility function of modern 2, 4, 8 and 12 story intact and damaged buildings with varying levels of damage.

4.5.4 Aftershock Damage Fragility Curves

The dynamic analysis results from mainshock-aftershock sequences are also used to compute the probability that a mainshock-damaged building will be in or exceed a particular damage state as a function of the aftershock shaking intensity (S_{di}). In this sense, the collapse fragility curve can be thought of as a special case of damage fragility curves. After the aftershock record, the building will either remain in the mainshock damage state or transition to a worse damage state. For the purposes of this discussion, as before, the aftershock damage state is defined by the maximum interstory drift, taken over the entire earthquake sequence.

The results of these calculations are summarized in Table 4.2 for the 4 story modern building, reporting the median S_{di} at which each damage state occurs and the standard deviation in the S_{di} at which each damage state occurs. The increasing median S_{di} values moving rightward through the columns in the table indicates that stronger ground motions are needed to incite larger drifts in the building. The decrease in medain S_{di} values moving downward through the rows in the table shows the reduction in ability of the mainshock-damaged buildings to resist damage. The median S_{di} and standard deviation for damage fragilities for all the other buildings is provided in Appendix 4.A.

Table 4.2 Aftershock fragility curve parameters for 4 story modern building (04MS)

	Aftershock Damage State												
Mainshock Damage State	*Median Capacity (S_{di}, in)*												
		ISD 0.005	ISD 0.010	ISD 0.015	ISD 0.020	ISD 0.025	ISD 0.030	ISD 0.035	ISD 0.040	ISD 0.045	ISD 0.050	ISD 0.055	Collapse
	Intact	1.74	3.49	4.78	5.57	6.30	7.04	7.70	8.27	8.68	9.15	9.54	10.72
	ISD 0.005		3.50	4.74	5.55	6.28	7.05	7.68	8.21	8.65	9.05	9.36	10.81
	ISD 0.010			4.56	5.41	6.06	6.61	7.10	7.56	7.94	8.27	8.53	9.58
	ISD 0.015				5.09	5.77	6.29	6.69	7.08	7.44	7.74	7.99	9.06
	ISD 0.020					5.29	5.85	6.29	6.67	6.99	7.28	7.55	8.65
	ISD 0.025						5.20	5.70	6.11	6.45	6.73	6.96	7.97
	ISD 0.030							4.73	5.29	5.67	5.97	6.22	7.13
	ISD 0.035								4.63	5.31	5.78	6.14	7.48
	ISD 0.040									4.46	5.12	5.64	7.04
	ISD 0.045										4.30	5.04	6.76
	ISD 0.050											4.83	6.69
	ISD 0.055												4.49
	Lognormal Standard Deviation												
		ISD 0.005	ISD 0.010	ISD 0.015	ISD 0.020	ISD 0.025	ISD 0.030	ISD 0.035	ISD 0.040	ISD 0.045	ISD 0.050	ISD 0.055	Collapse
	Intact	0.10	0.15	0.23	0.23	0.26	0.26	0.26	0.25	0.25	0.27	0.27	0.30
	ISD 0.005		0.15	0.23	0.23	0.26	0.25	0.25	0.25	0.25	0.26	0.28	0.32
	ISD 0.010			0.23	0.24	0.26	0.27	0.28	0.29	0.29	0.30	0.30	0.32
	ISD 0.015				0.26	0.27	0.28	0.30	0.30	0.32	0.32	0.32	0.34
	ISD 0.020					0.29	0.30	0.30	0.31	0.32	0.32	0.33	0.34
	ISD 0.025						0.31	0.31	0.31	0.31	0.32	0.32	0.33
	ISD 0.030							0.39	0.35	0.35	0.35	0.36	0.37
	ISD 0.035								0.49	0.39	0.36	0.36	0.35
	ISD 0.040									0.57	0.46	0.40	0.37
	ISD 0.045										0.51	0.41	0.38
	ISD 0.050											0.44	0.40
	ISD 0.055												0.79

4.5.5 Aftershock Collapse Capacity: Influence of Duration

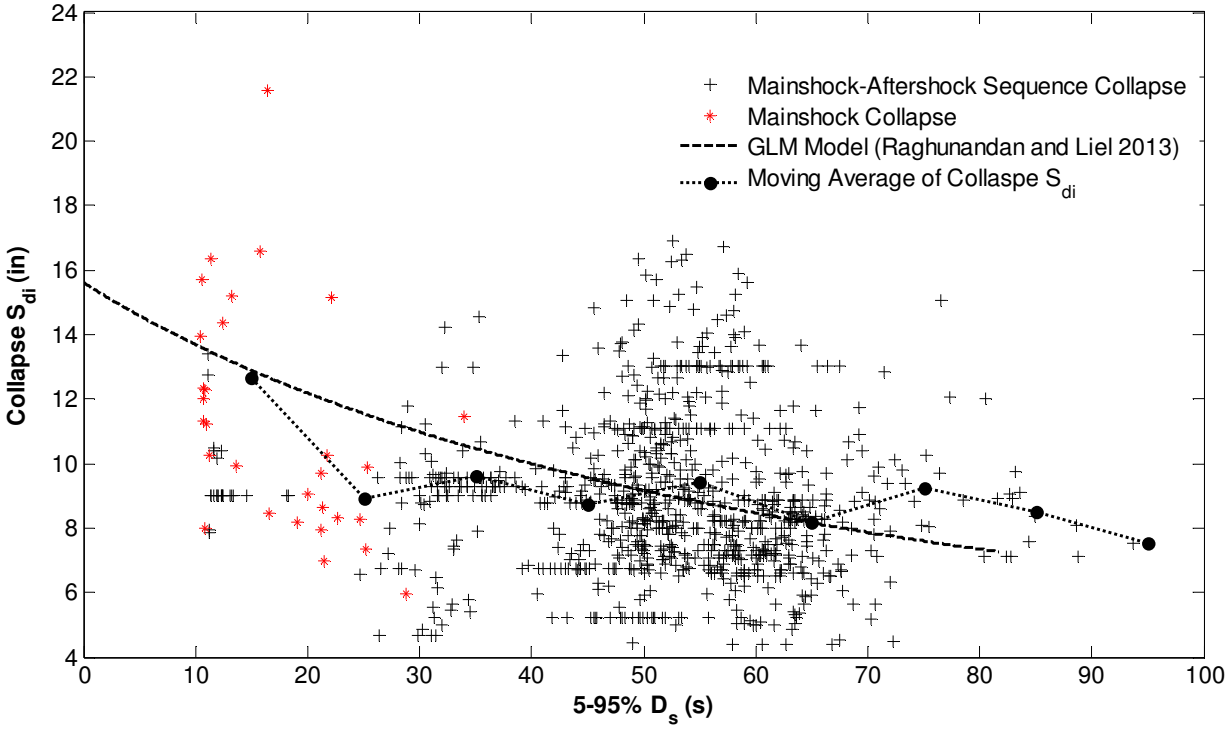

Figure 4.12 Variation of Collapse S_{di} with duration for 4 story intact building subjected to 30 mainshock ground motions causing collapse and 900 mainshock aftershock sequences causing collapse. For reference, the generalized linear model for variation of collapse capacity with duration(Raghunandan and Liel 2013) is provided along with the moving average of collapse S_{di} (10s average bins)

As mentioned before, earthquakes sequences can induce longer duration demand on the structure as compared to a single ground motion in the sequence. Increase in duration of ground motion can result in reduction in collapse capacity of the building and this fact has be quantified using the generalized linear model developed by Raghunandan and Liel (2013). Figure 4.12 illustrates the variation in collapse capacity of the 4 story buildings when subjected to a ground motion with the duration of the ground motion. Two types of ground motions are considered: (a) mainshock alone (quantified in terms of S_{di} for the ground motion scaled to collapse level) or, (b) earthquake sequence (quantified in terms of S_{di} for the scaled ground motion sequence causing collapse). It can be seen that the collapse S_{di} data approximately follows the GLM model line. This is further validate using the moving average of the collapse capacity data (calculated for 10s

bins) that also closely follows the GLM line generally. The moving average deviates from the GLM line where not many collapse data points are available.

4.6 Evaluation of Post-Earthquake Building Tagging Criteria

Building on these observations, the main objective of this study is to evaluate the effectiveness of various damage indicators, for assessing post-earthquake safety of mainshock damaged buildings. The damage indicators selected for evaluation are based on ATC-20 *red* tagging criteria.

4.6.1 Physical Damage Indicators

ATC-20 post-earthquake safety evaluation for building tagging is a three level procedure (ATC 1989, 1995). Here, we focus on the initial rapid evaluation (level 1) and detailed evaluation (level 2), and the visual criteria used to identify buildings that should be *red*-tagged during these evaluations. Although the visual physical damage criteria in ATC-20 are defined qualitatively, they can be quantified and related to physical damage observed in the analytical models in this study. For example, one of the basic rapid evaluation (level 1) criteria for a *red* tag based on overall damage to the structural system is "building or individual story noticeably leaning". This damage can be identified in mainshock damaged buildings in the analytical models quantifying large residual interstory drifts and residual roof drifts.

Table 4.3 summarizes the *red* tagging criteria defined in ATC-20 that are applicable to reinforced concrete moment frames, along with the physical damage indicator that can quantify that criterion in the building model. If any one of the physical conditions indicating *red* tagging in ATC-20 occurs in a structure (Column 2 of Table 4.3), the building should be declared *red*

tagged. Column 3 describes the damage indicators from the nonlinear analytical models that can predict the structural response corresponding to *red* tagging criteria in Column 2.

Table 4.3 Summary of physical visual damage in reinforced concrete frames indicating *red* tagging according to ATC-20 and the corresponding quantifiable criteria in building models used in this study

Evaluation Criteria	Physical condition of structural system indicating *red* tagging in ATC-20 (ATC 1995)	Quantifiable physical damage indicator (DI)
	Basic Rapid Evaluation Criteria	
Overall damage	Building has collapsed, partially collapsed, or moved off its foundation	Collapse of one or more stories
	Building or any story is significantly out of plumb	Residual interstory drift, residual roof drift
	Obvious severe damage to primary structural members, severe cracking of walls or other signs of severe distress present	Interstory drift, roof drift, failure or impending failure of beam and column plastic hinges (large plastic hinge deformations)
	Detailed Evaluation Criteria : General	
Overall damage	Collapse or partial collapse	Collapse of one or more stories
	Building or individual story noticeably leaning	Residual interstory drift, residual roof drift
Vertical load system	Columns noticeably out of plumb	Residual interstory drift, residual interstory drift
	Buckled or failed columns	Failure of column plastic hinges (large plastic hinge deformations)
Lateral load system	Broken, leaning or seriously degraded moment frames	Interstory drift, roof drift, failure or impending failure of beam and column plastic hinges
	Other failure or incipient failure of significant lateral load carrying element or connection	
Degradation of structural system	Seriously degraded structural system (concrete frames that experience cracking, spalling and local crushing of concrete, may still carry some vertical and lateral loads, but their overall strength can be greatly degraded even without the presence of other failure symptoms, e.g. buckled or out of plumb columns)	
	Detailed Evaluation Criteria : Concrete Structures	
Overall damage	Collapse or partial collapse	Collapse of one or more stories
	Building or individual story noticeably leaning	Residual interstory drift, residual roof drift
Slabs and beams	Separation from vertical support	Failure of beam plastic hinges (large plastic hinge deformations)
	Other failure or incipient failure of significant vertical load carrying element or connection	
Columns	Buckled or fractured columns	Failure or impending failure of column plastic hinges(large plastic hinge deformations)
	Massive spalling or exposure of vertical reinforcement	
	Large diagonal cracking extending through column	
Concrete moment frames	Seriously degraded moment frames	Interstory drift, roof drift, failure or impending failure of beam, column and joint plastic hinges
	Severe panel zone cracking	
	Noticeable residual drift in any story	Residual interstory drift, residual roof drift

Table 4.4 Description of quantifiable physical damage indicators

Damage indicator index	Damage indicator description	Observability without building instrumentation
DI 1	Number of beam plastic hinges with flexural rotation demand greater than beam flexural rotation capacity. Flexural rotation capacity quantified by θ_{cap} in Figure 4.3 (a)	Observable[a]
DI 2	Number of beam plastic hinges with flexural rotation demand greater than 50% of beam flexural rotation capacity.	Non-observable
DI 3	Number of column plastic hinges with flexural rotation demand greater than column flexural rotation capacity. Flexural rotation capacity quantified by θ_{cap} in Figure 4.3 (a)	Observable[a]
DI 4	Number of column plastic hinges with flexural rotation demand greater than 50% of column flexural rotation capacity.	Non-observable
DI 5	Maximum interstory drift ratio.	Non-observable
DI 6	Maximum residual interstory drift ratio.	Observable
DI 7	Maximum roof drift ratio.	Non-observable
DI 8	Maximum residual roof drift ratio.	Observable

[a] Observable for the structural model orientation used in this study. For other orientations, structural models need to be run before building inspectors arrive. So with more building analysis data, it will be an better observable physical damage indicator.

In this study, nonlinear dynamic analysis is carried out on the model representing the intact building and the physical state of the building (representing mainshock damage) is quantified using different physical damage indicators (DI) that are summarized in Table 4.4. The physical damage indicators are chosen such that most of the possible reinforced concrete damage from visual inspection can be quantified. Note that some physical damage indicators for *red* tagging that are not visually observable in a post-earthquake assessment (DI-5 and DI-7) are retained in the discussion because the findings may be applicable to instrumented buildings.

As summarized in Table 4.5, there is a strong correlation observed between different physical damage indicators based on drift (DI5-DI8) and this is observed uniformly for all the buildings. The high correlation in different drift measures is due to their combined response in defining the global response of the structure.

Table 4.5 Coefficient of correlation between physical damage indicators for mainshock damaged buildings

02MS									04MS							
	DI1	DI2	DI3	DI4	DI5	DI6	DI7	DI8	DI1	DI2	DI3	DI4	DI5	DI6	DI7	DI8
DI1	1.00	0.22	0.44	0.34	0.29	0.39	0.28	0.35	1.00	0.40	0.35	0.67	0.65	0.67	0.68	0.66
DI2		1.00	0.20	0.80	0.80	0.58	0.84	0.60		1.00	0.32	0.70	0.81	0.79	0.85	0.77
DI3			1.00	0.07	0.32	0.28	0.26	0.19			1.00	0.29	0.34	0.39	0.32	0.30
DI4				1.00	0.85	0.64	0.88	0.63				1.00	0.81	0.76	0.79	0.70
DI5					1.00	0.75	0.99	0.72					1.00	0.88	0.97	0.82
DI6						1.00	0.72	0.99						1.00	0.86	0.94
DI7							1.00	0.71							1.00	0.85
DI8								1.00								1.00
08MS									12MS							
	DI1	DI2	DI3	DI4	DI5	DI6	DI7	DI8	DI1	DI2	DI3	DI4	DI5	DI6	DI7	DI8
DI1	1.00	0.39	0.21	0.62	0.53	0.61	0.45	0.52	1.00	0.23	0.46	0.43	0.47	0.54	0.38	0.50
DI2		1.00	0.12	0.79	0.83	0.75	0.88	0.77		1.00	0.28	0.67	0.85	0.81	0.85	0.81
DI3			1.00	0.20	0.12	0.03	0.13	0.03			1.00	0.25	0.46	0.50	0.36	0.45
DI4				1.00	0.84	0.78	0.76	0.70				1.00	0.68	0.70	0.64	0.65
DI5					1.00	0.87	0.94	0.81					1.00	0.92	0.96	0.90
DI6						1.00	0.83	0.95						1.00	0.85	0.98
DI7							1.00	0.84							1.00	0.87
DI8								1.00								1.00

4.6.2 Relationship between Aftershock Collapse Capacity and Damage Indicators

The variation in collapse capacity of the mainshock-damaged building with respect to various physical damage indicators is used to determine the how well each damage indicator predicts the reduced capacity of the building to resist aftershocks. The change in the collapse capacity is quantified by the percent reduction in the collapse capacity of the damaged building as compared to the intact building. The reduction in collapse capacity is calculated by comparing the collapse capacity of the intact building on being subjected to an arbitrary record with the collapse capacity of the damaged building being subjected to the same arbitrary record. In this discussion, all the 900 sequences for 11 damage states are used as a combined set for analysis for all levels of damage of a building.

Figure 4.13 illustrates how the reduction in collapse capacity of damaged building is calculated. The solid line represents the IDA curve for the intact 4 story building (i.e. no damage) when subjected to a selected mainshock record. The flat region of the curve at large

drifts (representing failure by sidesway collapse) indicates a collapse capacity of S_{di} = 6.8in. The dotted line is the IDA curve of aftershock analysis of the same building, whose mainshock damage is quantified by a peak interstory drift of 0.035 inches (ISD 0.035), and where the aftershock is the same record as the mainshock applied to the intact building. The collapse capacity of the damaged building is reduced by 29% to S_{di} = 5 in., due to accumulation of damage in the already damaged building.

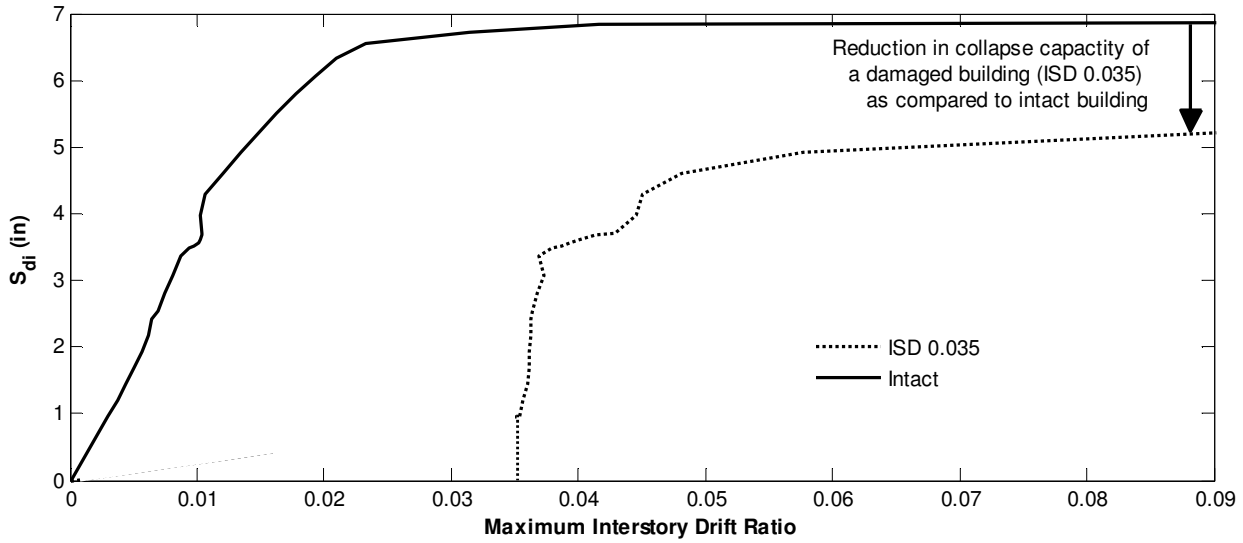

Figure 4.13 Illustration of reduction in collapse capacity of building damaged in mainshock (ISD 0.035) from the intact building for the 4 story modern building (04MS).

The physical damage indicator that best predicts the reduction in collapse capacity provides an ideal damage indicator. Figure 4.14 illustrates the variation of the aftershock capacity (quantified in terms of percentage reduction in collapse capacity of the damaged building in an aftershock) with the damage observed in the mainshock damaged building (quantified in terms of the physical damage indicators) for the 4 story building. The data are highly scattered, but there is a strong trend of more reduction in damage capacity with increasing values of the various damage indicators.

For each of the damage indicators, a linear regression line is fitted between dependent response variable Y, percentage reduction in collapse capacity of damaged building in aftershock and explanatory variable X, physical damage indicator at each damage state. Table 4.6 summarizes the results from this linear regression for all the four buildings. The results from the analysis can be also used to predict a range for possible reduction in collapse capacity of the mainshock damaged building given a particular value of the damage indicator such as maximum interstory drift during post-earthquake assessment of building. For e.g., a maximum interstory drift ratio of 2% (similar to ASCE 7-10 building code seismic design drift limit for risk category I buildings) during a mainshock can result in an expected reduction of 16,17, 15and 19 % in collapse capacity of a 2,4,8 and 12 story building respectively in aftershock.

Similarly, Table 4.7 summarizes the results for linear regression fitted with dependent response variable Y, physical damage indicator at each damage and explanatory variable X percentage reduction in collapse capacity of damaged building in aftershock, for all the four buildings. This regression helps in answering the other question, " For a particular reduction in collapse capacity of damaged building in an aftershock, what are values of the physical damage indicators observed for that building during post-earthquake evaluation?" For e.g., for a 40% reduction in the collapse capacity of the damaged building in aftershock, the 2,4,8 and 12 story buildings will have expected maximum interstory drift of 4.2, 3.5, 3.6 and 3.4% respective. Results in Table 4.6 and Table 4.7 will help in estimating the structural safety in a post-earthquake visual assessment scenario based on the damage indicators. These results will also help in assessing the post-earthquake safety for buildings with drift monitoring with sensors. Since there is a lot of scatter in the data, the standard deviation values are also provided for the

response variable in both the tables to determine the range along with the expected value of the response variable.

Table 4.6 Linear regression results for model fitted between percentage reduction in collapse capacity of damage building due to aftershock.and mainshock physical damage indicators and

X : Physical Damage Indicators									
Y : % Reduction in Collapse Capacity from of Damaged Building									
Y : Intercept + Slope * X									
	02MS					**04MS**			
X	**Slope**	**Intercept**	**R^2**	**σ**	**X**	**Slope**	**Intercept**	**R^2**	**σ**
DI1	39.8	26.1	0.19	24.4	DI1	6.7	19.0	0.16	21.8
DI2	3.1	22.9	0.11	25.6	DI2	2.3	14.4	0.18	21.5
DI3	12.5	27.7	0.12	25.6	DI3	15.6	21.0	0.15	21.9
DI4	3.7	19.3	0.15	25.0	DI4	3.9	16.8	0.16	21.8
DI5	729.3	1.1	0.18	24.6	DI5	802.1	0.5	0.27	20.3
DI6	691.6	19.2	0.13	25.3	DI6	902.9	9.2	0.34	19.3
DI7	848.4	1.6	0.17	24.7	DI7	1199.1	1.8	0.24	20.7
DI8	729.3	20.7	0.11	25.7	DI8	1239.2	12.5	0.24	20.7
	08MS					**12MS**			
X	**Slope**	**Intercept**	**R^2**	**σ**	**X**	**Slope**	**Intercept**	**R^2**	**σ**
DI1	17.8	20.8	0.19	21.0	DI1	6.2	27.5	0.12	22.8
DI2	2.2	13.6	0.30	19.5	DI2	2.1	15.5	0.45	18.1
DI3	13.1	24.3	0.02	23.2	DI3	14.2	27.3	0.12	22.8
DI4	6.2	14.6	0.33	19.1	DI4	5.9	20.8	0.30	20.3
DI5	1002.1	-5.0	0.44	17.4	DI5	1186.1	-4.9	0.59	15.5
DI6	956.8	10.3	0.35	18.7	DI6	1075.8	10.2	0.59	15.6
DI7	2059.7	-4.6	0.38	18.3	DI7	3491.8	-8.8	0.52	16.8
DI8	2253.8	11.9	0.31	19.4	DI8	3493.5	10.6	0.55	16.3

Table 4.7 Linear regression results for model fitted between mainshock physical damage indicators and percentage reduction in collapse capacity of damage building due to aftershock.

X : % Reduction in Collapse Capacity from of Damaged Building; **Y** : Physical Damage Indicators									
Y : Intercept + Slope * X									
	02MS					**04MS**			
X	**Slope**	**Intercept**	**R^2**	**σ**	**X**	**Slope**	**Intercept**	**R^2**	**σ**
DI1	4.9E-03	-4.6E-02	0.19	0.270	DI1	2.3E-02	1.8E-01	0.16	1.282
DI2	3.7E-02	1.2E+00	0.11	2.795	DI2	7.6E-02	2.3E+00	0.18	3.914
DI3	9.3E-03	-9.4E-02	0.12	0.695	DI3	9.4E-03	-3.6E-02	0.15	0.538
DI4	4.1E-02	1.7E+00	0.15	2.647	DI4	4.1E-02	8.6E-01	0.16	2.235
DI5	2.4E-04	3.2E-02	0.18	0.014	DI5	3.3E-04	2.1E-02	0.27	0.013
DI6	1.9E-04	9.8E-03	0.13	0.013	DI6	3.7E-04	7.3E-03	0.34	0.012
DI7	2.0E-04	2.7E-02	0.17	0.012	DI7	2.0E-04	1.4E-02	0.24	0.008
DI8	1.5E-04	8.3E-03	0.11	0.012	DI8	2.0E-04	4.5E-03	0.24	0.008
	08MS					**12MS**			
X	**Slope**	**Intercept**	**R^2**	**σ**	**X**	**Slope**	**Intercept**	**R^2**	**σ**
DI1	1.1E-02	-4.4E-02	0.19	0.510	DI1	2.0E-02	-2.2E-01	0.12	1.281
DI2	1.4E-01	1.6E+00	0.30	4.784	DI2	2.1E-01	4.8E-01	0.45	5.808
DI3	1.2E-03	-4.4E-03	0.02	0.222	DI3	8.6E-03	-7.7E-02	0.12	0.560
DI4	5.3E-02	3.2E-01	0.33	1.768	DI4	5.1E-02	1.9E-02	0.30	1.874
DI5	4.4E-04	1.9E-02	0.44	0.012	DI5	5.0E-04	1.4E-02	0.59	0.010
DI6	3.7E-04	5.8E-03	0.35	0.012	DI6	5.5E-04	1.9E-03	0.59	0.011
DI7	1.9E-04	9.6E-03	0.38	0.005	DI7	1.5E-04	6.6E-03	0.52	0.003
DI8	1.4E-04	2.2E-03	0.31	0.005	DI8	1.6E-04	8.1E-04	0.55	0.003

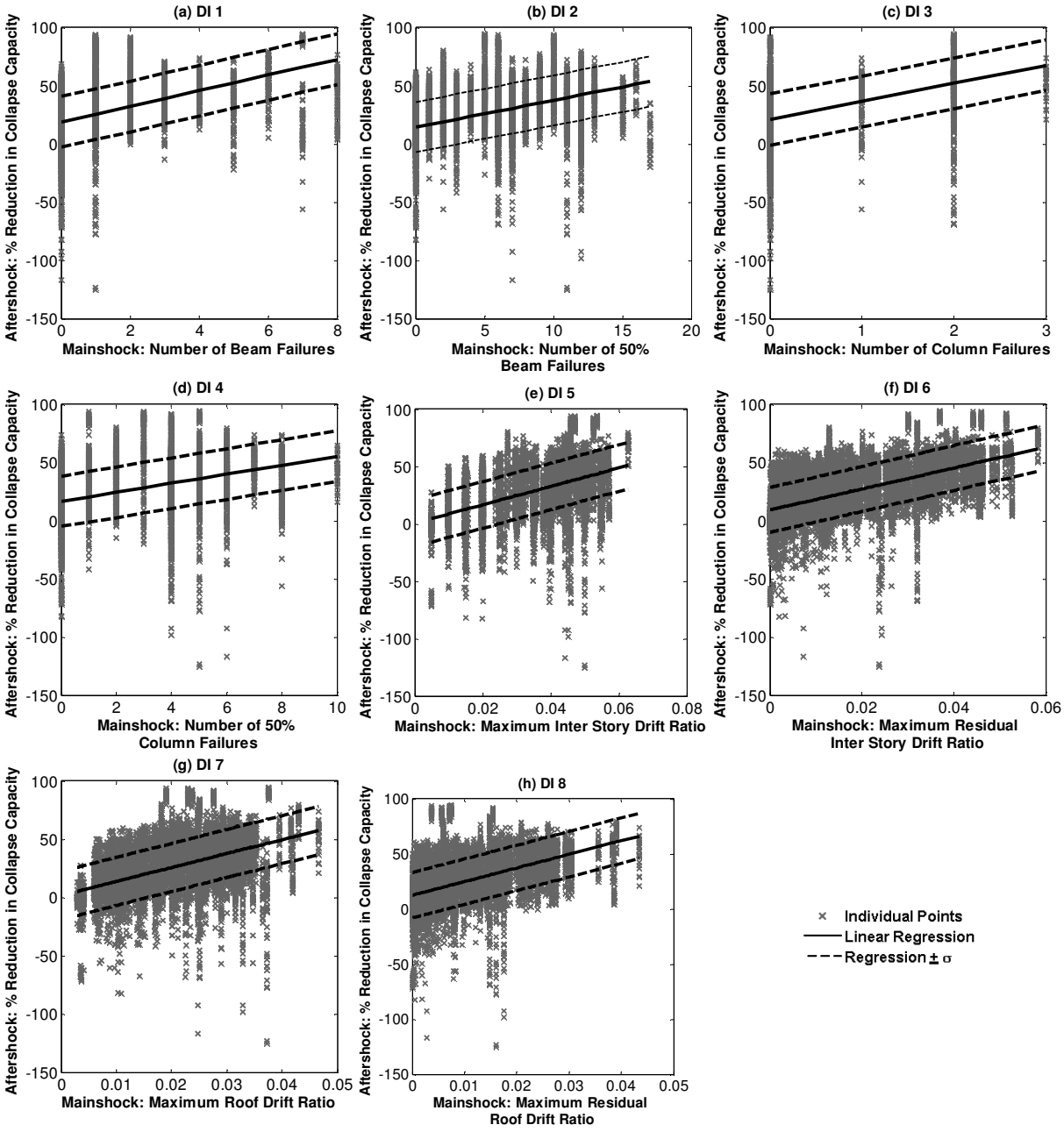

Figure 4.14 Variation of reduction in collapse capacity of the damaged building with different physical damage indicators of mainshock damage.

Note, however, that Figure 4.14 shows some cases (corresponding to 10-13% of the earthquake sequences) in which the collapse capacity of the damaged structure is actually greater than the collapse capacity of the intact structure. Although this number may seem a little high, around 80% of these aftershock strengthened records belong to first 3 least damaging mainshock

damage states (see Figure 4.15). For these damage states, the building is practically undamaged in mainshock and therefore the aftershock collapse capacity can go higher or lower reflecting the same record to record variability found in IDA analysis of an intact building. For other damage states, the increase in aftershock capacity can be explained based on the presence of "resurrecting records" in IDA which cause lower levels of damage at higher intensities (Vamvatsikos and Cornell 2002). For multiple story buildings, this can occur usually due to yielding of structural components at a particular story or floor at the higher intensity of ground shaking, and thereby relieving the forces on other floor. The lower number of sequences having increased capacity in aftershock (10%) for the 2 story building as compared to higher number of sequences having increased capacity in aftershock (13%) for the 12 story buildings can be explained based on the fact that a 12 story frame has more number of failure modes possible for collapse as compared to a 2 story building.

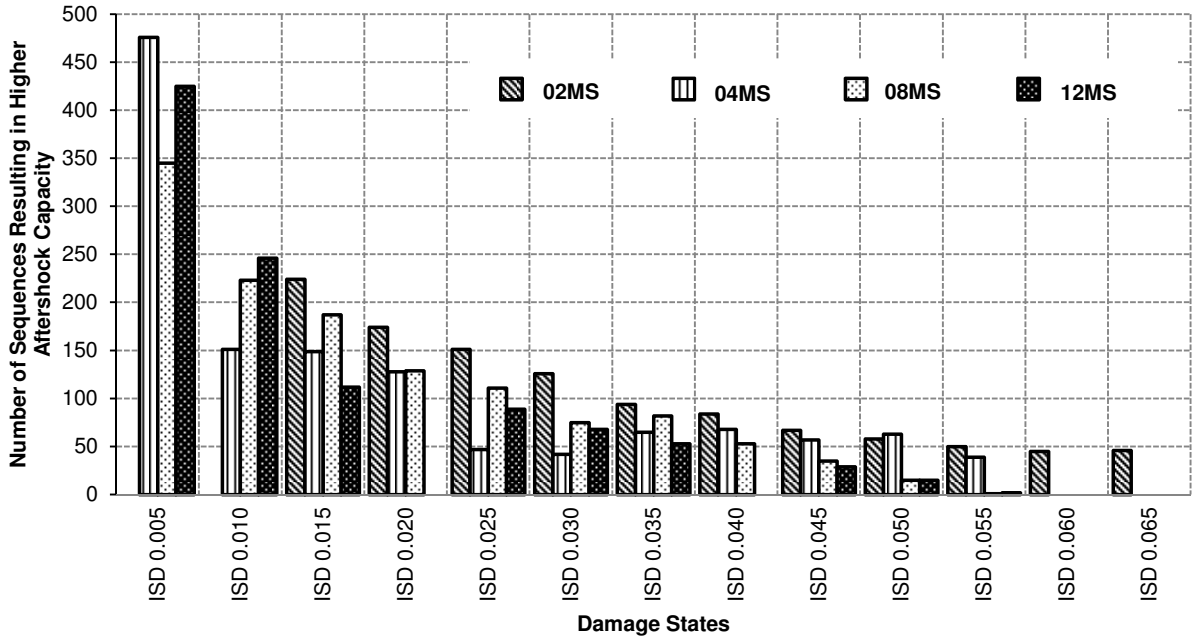

Figure 4.15 Distribution of earthquake sequences for which collapse capacity of damaged building was found to be higher than intact building.

4.6.3 Ranking of Physical Damage Indicators

To identify the effectiveness of different mainshock physical damage indicators (Table 4.4) as predictors of aftershock fragility, the physical damage indicators are ranked based on the analysis results obtained for the four different buildings. A ranking system is developed based on three ranking indicators, (a) slope angle and (b) correlation coefficient calculated from regression equations between explanatory variables X, the physical damage indicators, and Y, the percent reduction in collapse capacity, and, (c) general visual observability of physical damage indicator in a post-earthquake scenario. The first two ranking indicators are selected because they quantify the ability of damage indicators to predict variations in collapse capacity or, equivalently, the sensitivity of the variation in collapse capacity to the various damage indicators. The slope angle is calculated as the angle that the linear regression line makes with the x axis. The coefficient of correlation represents the goodness-of-fit of the linear regression between the reduction in collapse capacity and damage indicators. Since the scale of damage indicators vary substantially, the x-axis is normalized by subtracting mean and dividing by standard deviation before calculations of slope angle and coefficient of correlation are carried out.

Table 4.8 summarizes the rankings for slope angle and coefficient of correlation. The best ranking, denoted (1), is assigned to that physical damage indicator that provides the highest values of slope angle and coefficient of correlation. Therefore, the best damage indicator will have the smallest rank number. Overall, the physical damage indicators are ranked based on 3 criteria:

- **Ranking 1**: Rankings assigned based on slope angle relating reduction in collapse capacity of damaged building to physical damage indicator.

- **Ranking 2**: Rankings assigned based on correlation coefficient between reduction in collapse capacity of damaged building and physical damage indicator.

- **Ranking 3**: Observability of physical damage indicators in post-earthquake visual inspection. Damage indicators that are readily observable are assigned a ranking of 1 (best) and those that are not observable are ranked 8 (worst).

- **Total Ranking**: Sum of rankings 1-3.

Table 4.8 Rankings based on linear regression between mainshock physical damage indicators and percentage reduction in collapse capacity due to aftershock.

X : Physical Damage Indicators									
Y : % Reduction in Collapse Capacity of Damaged Building									
	02MS					**04MS**			
X	**Correlation Coefficient**	**Rank Correlation**	**Slope Angle**	**Rank Slope Angle**	**X**	**Correlation Coefficient**	**Rank Correlation**	**Slope Angle**	**Rank Slope Angle**
DI1	0.44	1	85.2	1	DI1	0.40	7	83.9	7
DI2	0.33	7	83.7	7	DI2	0.42	5	84.3	5
DI3	0.34	6	83.8	6	DI3	0.38	8	83.7	8
DI4	0.39	4	84.6	4	DI4	0.40	6	84.0	6
DI5	0.42	2	85.0	2	DI5	0.52	2	85.3	2
DI6	0.37	5	84.2	5	DI6	0.58	1	85.9	1
DI7	0.41	3	84.9	3	DI7	0.49	4	85.1	4
DI8	0.33	8	83.6	8	DI8	0.49	3	85.1	3
	08MS					**12MS**			
X	**Correlation Coefficient**	**Rank Correlation**	**Slope Angle**	**Rank Slope Angle**	**X**	**Correlation Coefficient**	**Rank Correlation**	**Slope Angle**	**Rank Slope Angle**
DI1	0.43	7	84.3	7	DI1	0.35	7	83.3	7
DI2	0.55	6	85.5	6	DI2	0.67	5	86.5	5
DI3	0.13	8	71.1	8	DI3	0.35	8	83.3	8
DI4	0.57	4	85.7	4	DI4	0.55	6	85.7	6
DI5	0.66	1	86.3	1	DI5	0.77	1	86.9	1
DI6	0.60	3	85.9	3	DI6	0.77	2	86.9	2
DI7	0.62	2	86.0	2	DI7	0.72	4	86.7	4
DI8	0.56	5	85.6	5	DI8	0.74	3	86.8	3

In each case, the lowest ranking indicates the superior damage indicator.

Figure 4.16 illustrates ranking outcomes for all the buildings. According to the total rank criteria, maximum and residual maximum interstory drift ratio (DI5-DI6) are the best physical damage indicators. These indicators are followed closely by maximum and residual roof drift ratio. The residual drift ratios can be measured more easily in a post-earthquake assessment in the absence of structural health monitoring or instrumentation. The number of beam and column failures predict the variation in collapse capacity, but they are not as effective as predicting the loss in capacity as the drift measures. However, depending on the state of the structure, and the measurable physical damage indicator at site, any of the measures can be used because they all predict the reduction in collapse capacity during aftershock effectively.

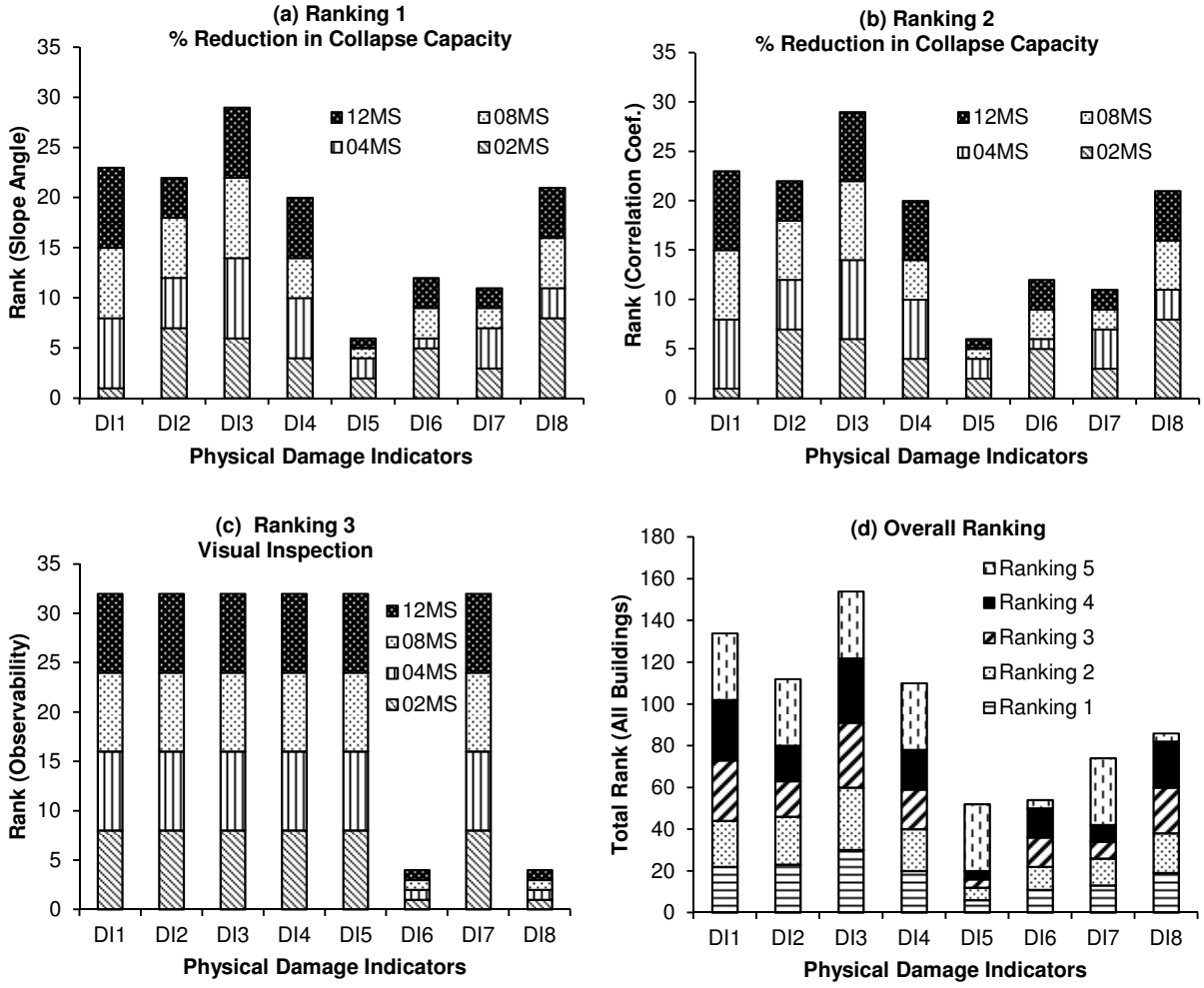

Figure 4.16 Rankings of physical damage indicators for all of the buildings.

4.6.4 Application to Building Tagging

This section illustrates and example for how the results from this study can be used to assess the post-earthquake safety of reinforced concrete frame buildings based on the physical damage indicators observed for the damaged building. Depending on whether the building is instrumented or not instrumented, a physical damage indicator should be chosen by the building inspector. Mostly the buildings are non-instrumented, so physical damage indicators such as residual maximum interstory drift and residual roof drift will serve as best indicators for post-earthquake visual safety assessment of buildings. Next step would be to associate percentage reduction in collapse capacity with *red* tagging and *yellow* tagging. For illustration purposes, it is assumed that 40% and 20% reduction in collapse capacity of mainshock damaged building in aftershock will result in building being *red* tagged and *yellow* tagged and the physical damage indicator that is observed during visual inspection is residual maximum interstory drift. Based on the regression coefficients provided in Table 4.7, average residual maximum interstory drifts that will cause buildings to be *red* tagged are: (a) 1.8% for 2 story, (b) 2.2% for 4 story, (c) 2.1% for 8 story, and (d) 2.4% for 12 story. Similarly, average residual maximum interstory drifts that will cause buildings to be *yellow* tagged are: (a) 1.4% for 2 story, (b) 1.5% for 4 story, (c) 1.3% for 8 story, and (d) 1.3% for 12 story.

4.7 Conclusions

Buildings in seismically active region may be exposed to multiple earthquakes in quick succession (such as aftershocks following mainshocks) and there is often no time for repair between these events. If a building is damaged in the mainshock, there is possibility earthquake shaking. Therefore, the probability of structural damage or collapse from a mainshock-aftershock

sequence may be higher than the risk of structural damage or collapse from a single event and it becomes important to quantify and assess this probable increase in damage risk for better public safety, especially in the context of post-earthquake rapid visual inspections. Post-earthquake safety assessments following a major earthqauke are important for evacuation of people from damaged structures and identifying buildings requiring repair. ATC-20 provides specific qualitative guidelines used to classify the post-earthquake safety of buildings in three categories based on visual inspections: UNSAFE or *red* tagged, RESTRICTED USE or *yellow* tagged and SAFE or *green* tagged.

In this study, analytical models of modern reinforced concrete buildings representative of current design and construction in high seismic zones are subjected to earthquake sequences comprising of two ground motions. These earthquake sequences are generated such that structural response and damage in the mainshock is recorded, and the scaling of second record in the sequence results in multiple levels of damage in aftershock, leading to collapse. The aftershock collapse fragility of the damaged buildings is significantly reduced if it is severely damage in mainshock; however, if the damage sustained by the structure in mainshock is less, the aftershock building fragility is not much affected.

There are eight physical damage indicators identified for the building based on ATC-20 *red* tagging criteria to quantify the physical damage of the building following a mainshock. The results from the analysis indicate correlation between the value of the damage indicators and the percentage change in the collapse capacity of the damaged building in aftershock as compared to the intact building. Based on relations between change in collapse capacity of damaged building in aftershock and physical indicators, a ranking criteria to assess physical damage indicators is developed based on its sensitivity to change in collapse capacity in aftershock. It is found that

maximum interstory drift and maximum residual interstory drift are the best damage measures, closely followed by maximum and residual roof drifts. Other physical damage measures may have lower rankings but they still predict reduction in collapse capacity quite effectively and can be used when it is difficult to measure drifts in a post-earthquake assessment scenario. The results from this study can help in quantifying the physical damage for *red* tagging criteria for modern reinforced concrete frame buildings in ATC-20 by providing a range of physical damage values for a certain percentage reduction in collapse capacity in aftershock (corresponding to red tagging). It is also helpful in predicting the expected percentage reduction in collapse capacity for observed damage in the structure.

For complete evaluation of the infrastructure of reinforced concrete buildings in California, it is also necessary to assess aftershock damage fragilities of older non-ductile frames. This analysis is not carried out as part of the current research work.

Appendix 4.A Aftershock Damage Fragility Parameters

Table 4.9 Aftershock fragility curve parameters for 2 story modern building (02MS)

		Aftershock Damage State											
Mainshock Damage State		*Median Capacity (S_{di}, in)*											
		ISD 0.005	ISD 0.010	ISD 0.015	ISD 0.020	ISD 0.025	ISD 0.030	ISD 0.035	ISD 0.040	ISD 0.045	ISD 0.050	ISD 0.055	Collapse
	Intact	3.34	4.49	5.28	5.91	6.56	7.12	7.69	8.08	8.40	8.70	9.03	10.31
	ISD 0.015		1.92	3.09	4.26	5.14	5.80	6.35	6.82	7.26	7.59	7.90	9.26
	ISD 0.020			2.69	3.90	4.91	5.61	6.12	6.56	6.94	7.27	7.57	8.78
	ISD 0.025				3.38	4.51	5.29	5.86	6.30	6.67	6.99	7.28	8.42
	ISD 0.030					3.84	4.84	5.48	6.00	6.40	6.73	7.03	8.18
	ISD 0.035						3.61	4.67	5.34	5.83	6.20	6.50	7.59
	ISD 0.040							5.30	5.65	5.90	6.07	6.23	6.70
	ISD 0.045								5.04	5.43	5.70	5.89	6.46
	ISD 0.050									4.46	4.71	4.88	5.51
	ISD 0.055										3.02	3.77	5.32
	ISD 0.060											2.67	5.00
	ISD 0.065												4.75
		Lognormal Standard Deviation											
		ISD 0.005	ISD 0.010	ISD 0.015	ISD 0.020	ISD 0.025	ISD 0.030	ISD 0.035	ISD 0.040	ISD 0.045	ISD 0.050	ISD 0.055	Collapse
	Intact	0.22	0.22	0.22	0.21	0.22	0.22	0.23	0.23	0.23	0.24	0.24	0.26
	ISD 0.015		0.24	0.27	0.27	0.25	0.24	0.24	0.23	0.22	0.22	0.22	0.26
	ISD 0.020			0.31	0.29	0.27	0.26	0.25	0.24	0.22	0.22	0.22	0.26
	ISD 0.025				0.34	0.31	0.29	0.27	0.25	0.24	0.24	0.24	0.27
	ISD 0.030					0.36	0.32	0.30	0.28	0.27	0.26	0.26	0.27
	ISD 0.035						0.64	0.42	0.35	0.32	0.30	0.29	0.28
	ISD 0.040							0.34	0.34	0.33	0.33	0.34	0.35
	ISD 0.045								0.42	0.39	0.38	0.38	0.38
	ISD 0.050									0.79	0.78	0.78	0.68
	ISD 0.055										1.00	0.90	0.69
	ISD 0.060											1.01	0.69
	ISD 0.065												0.70

Table 4.10 Aftershock fragility curve parameters for 8 story modern building (08MS)

	Aftershock Damage State											
Mainshock Damage State	*Median Capacity (S_{di}, in)*											
		ISD 0.005	ISD 0.010	ISD 0.015	ISD 0.020	ISD 0.025	ISD 0.030	ISD 0.035	ISD 0.040	ISD 0.045	ISD 0.050	ISD 0.055	Collapse
	Intact	3.17	5.96	8.36	10.34	12.18	14.18	15.73	17.06	18.20	19.00	19.68	22.58
	ISD 0.005		5.95	8.35	10.33	12.14	14.15	15.67	17.00	18.08	18.95	19.64	22.46
	ISD 0.010			8.26	10.04	12.03	13.90	15.34	16.56	17.52	18.30	18.91	21.48
	ISD 0.015				9.88	11.79	13.41	14.75	15.81	16.64	17.35	17.91	20.13
	ISD 0.020					11.26	12.76	14.00	14.99	15.71	16.29	16.74	18.67
	ISD 0.025						11.86	13.13	14.05	14.72	15.26	15.70	17.51
	ISD 0.030							11.85	12.85	13.63	14.22	14.68	16.62
	ISD 0.035								11.55	12.50	13.19	13.69	15.63
	ISD 0.040									11.27	12.22	12.90	14.98
	ISD 0.045										9.94	10.90	13.19
	ISD 0.050											9.10	11.90
	ISD 0.055												10.15
	Lognormal Standard Deviation												
		ISD 0.005	ISD 0.010	ISD 0.015	ISD 0.020	ISD 0.025	ISD 0.030	ISD 0.035	ISD 0.040	ISD 0.045	ISD 0.050	ISD 0.055	Collapse
	Intact	0.19	0.20	0.18	0.17	0.20	0.23	0.23	0.21	0.22	0.23	0.23	0.25
	ISD 0.005		0.19	0.18	0.17	0.19	0.23	0.23	0.21	0.21	0.23	0.23	0.25
	ISD 0.010			0.19	0.19	0.21	0.24	0.23	0.22	0.23	0.23	0.24	0.25
	ISD 0.015				0.22	0.23	0.24	0.24	0.24	0.25	0.25	0.26	0.26
	ISD 0.020					0.24	0.25	0.25	0.26	0.27	0.27	0.28	0.28
	ISD 0.025						0.28	0.28	0.29	0.29	0.30	0.30	0.30
	ISD 0.030							0.32	0.32	0.32	0.33	0.32	0.31
	ISD 0.035								0.35	0.34	0.34	0.34	0.33
	ISD 0.040									0.36	0.35	0.35	0.34
	ISD 0.045										0.43	0.39	0.36
	ISD 0.050											0.43	0.35
	ISD 0.055												0.41

Table 4.11 Aftershock fragility curve parameters for 12 story modern building (12MS)

	Aftershock Damage State												
Mainshock Damage State	*Median Capacity (S_{di}, in)*												
		ISD 0.005	ISD 0.010	ISD 0.015	ISD 0.020	ISD 0.025	ISD 0.030	ISD 0.035	ISD 0.040	ISD 0.045	ISD 0.050	ISD 0.055	Collapse
	Intact	4.13	7.22	10.10	12.77	15.20	17.51	19.07	20.34	21.31	22.30	22.72	24.37
	ISD 0.005		7.24	10.09	12.75	15.17	17.36	18.97	20.23	21.18	22.04	22.57	24.49
	ISD 0.010			9.90	12.45	14.63	16.48	17.97	19.15	19.99	20.59	21.08	23.06
	ISD 0.015				11.95	13.74	15.08	16.21	17.16	17.87	18.39	18.78	20.72
	ISD 0.020					12.63	13.90	14.91	15.69	16.30	16.82	17.23	19.05
	ISD 0.025						12.50	13.58	14.36	14.98	15.45	15.82	17.54
	ISD 0.030							12.18	13.21	13.92	14.45	14.83	16.57
	ISD 0.035								11.21	12.14	12.82	13.31	15.11
	ISD 0.040									9.58	10.47	11.09	13.12
	ISD 0.045										8.30	9.09	11.34
	ISD 0.050											7.87	10.50
	ISD 0.055												9.23
	Lognormal Standard Deviation												
		ISD 0.005	ISD 0.010	ISD 0.015	ISD 0.020	ISD 0.025	ISD 0.030	ISD 0.035	ISD 0.040	ISD 0.045	ISD 0.050	ISD 0.055	Collapse
	Intact	0.30	0.22	0.21	0.21	0.19	0.19	0.19	0.20	0.22	0.24	0.24	0.24
	ISD 0.005		0.22	0.20	0.21	0.19	0.18	0.19	0.20	0.22	0.24	0.24	0.23
	ISD 0.010			0.23	0.22	0.19	0.20	0.21	0.23	0.24	0.25	0.25	0.25
	ISD 0.015				0.23	0.23	0.24	0.26	0.27	0.28	0.28	0.28	0.27
	ISD 0.020					0.29	0.29	0.30	0.31	0.31	0.32	0.32	0.31
	ISD 0.025						0.33	0.33	0.34	0.34	0.34	0.34	0.33
	ISD 0.030							0.36	0.35	0.35	0.35	0.35	0.34
	ISD 0.035								0.45	0.43	0.41	0.40	0.36
	ISD 0.040									0.48	0.46	0.45	0.38
	ISD 0.045										0.49	0.48	0.37
	ISD 0.050											0.50	0.38
	ISD 0.055												0.41

CHAPTER 5 CONCLUSIONS

5.1 General Conclusions

The ground motion recorded at any site can be characterized based on its intensity, frequency content and duration. The influence of ground motion intensity and frequency content on the seismic response of structures is widely accepted in the research community. These two ground motion parameters are explicitly accounted for in seismic design spectra for a site that is used for seismic design of buildings. However, the influence of ground motion duration on structural damage is a source of disagreement in the engineering community. In previous studies, variation in research study aspects, such as the damage measure used to capture structural damage, the complexity of the building model, and the definition of ground motion duration, resulted in the different observations of relationship between ground motion duration and structural damage. Seismic design codes implicitly account for ground motion duration through the expected intensity of ground motion at the site, which depends on the magnitude of expected earthquake. The higher magnitude of earthquake results in longer duration of ground shaking because of the longer time taken for fault rupture. However, at any site, there several other factors that can result in longer duration of ground shaking, which are not considered in design. A building located at a site can be subjected to long duration ground shaking when it is located at far distances from epicenter, is located on soft soil site, is located a site susceptible to subduction earthquakes and is located at a site subjected to multiple earthquake sequences.

The main objective of this thesis was to understand if the duration parameter of a ground motion, along with ground motion intensity and frequency content, is significant in predicting collapse of structures. Since the duration parameter was found to be significant, the thesis proceeds to

quantify how it influences the collapse of structures exposed to long duration seismic hazards, such as subduction earthquakes and mainshock-aftershock sequences.

Based on the analysis carried out in this thesis, following general conclusions can be made:

- Ground motion duration is significant for structural collapse and should be considered along with the ground motion intensity and frequency content for evaluating structural collapse risk. For a building subjected to same intensity long and short duration ground motions, the seismic collapse risk is of the building is significantly higher on being subjected to long duration ground motions as compared to short duration ground motions. Therefore, it is important to consider the influence of duration at sites susceptible to long duration shaking, because accumulation of damage over a large number of loading cycles can significantly reduce the collapse capacity of the buildings. Results are not thought to be sensitive to the definition of ground motion duration employed.
- Ductile buildings are more sensitive to the influence of ground motion duration as compared to non-ductile buildings due to their higher deformation and energy dissipation capacity.
- For buildings located at sites exposed to both crustal and subduction earthquakes, the collapse capacity of a building is lesser when subjected to long duration subduction ground motions as compared to shorter duration crustal ground motions. On the basis of this observation, the thesis proposes to separately convolve fragility and hazard curves for subduction and crustal earthquakes. In fact, for sites in Pacific Northwest of the U.S., the seismic collapse risk of building is underestimated by around 40% if only crustal building fragility curves are used instead of separate building fragility curves, because subduction earthquakes contribute largely to the seismic collapse risk. This also indicates the need of

modifying the MCE_R values for sites in Seattle and Portland to ensure uniform probability of collapse of 1% in 50 years.

- The risk of accumulating damage in a structure due to a sequence of earthquakes can be viewed as analogous to long duration shaking. Based on the analysis carried out in the thesis, if the building is not severely damaged in mainshock, its aftershock collapse capacity is not significantly changed as compared to an intact building. However, if there is significant damage to the structure in mainshock, the aftershock collapse capacity of the damaged building is significantly reduced as compared to intact building. This observation holds true for modern and older structures.
- The physical state of the building damaged in mainshock (as measured by number of structural member failures and drifts experienced by the structure) is related to the reduction in collapse capacity of the structure in aftershock. These damage indicators can be quantified for the analytical models to predict the post-earthquake safety of the building in terms of the reduced capacity of the building to resist subsequent ground shaking.

5.2 Research Limitations and Future Work

- The role of duration is widely accepted as contributing to geotechnical failures in earthquakes, such as liquefaction and slope instability. To account for duration, a magnitude scaling factor calculated based on field performance data during actual earthquakes is used adjust the resistance of soil to softening (Youd et al. 2001). The magnitude scaling factor provides a way to correlate the duration of ground motion in the field to the number of equivalent uniform cycles in the laboratory. Currently, the building codes do not have any such adjustments to the design values for expected long duration shaking at site. Investigations need to be carried out to assess ways to adjust the building seismic design

intensities for building located at sites exposed to long duration ground shaking. The results in this study suggest that artificially increasing the design intensity could achieve this goal.

- In this thesis, the observed trends of higher collapse vulnerability of buildings subjected to long duration shaking are validated for reinforced concrete moment frame buildings. The models used in this study are fairly complex as compared to many the models used in previous studies. Specifically, this study employs multiple degree of freedom nonlinear two-dimensional models for concrete frames, capable of capturing strength and stiffness deterioration of the frame under dynamic loading up to the point of collapse. The models used in this study were successful in capturing the primary modes of failure of the structures, such as flexural for ductile buildings and brittle axial and shear for non-ductile buildings. Use of models capable of capturing structural collapse in a successful manner also ensures that similar trends can be observed for ductile and non-ductile steel frames and irregular reinforced concrete frames when subjected to long duration shaking. However, collapse capacities needs to be validated for other lateral load resisting systems for a complete building portfolio assessment in a seismically active region.
- The response of the structure is during dynamic loading is influenced by the interaction between the structure, its foundation and the soil underlying the foundation (NIST 2012). The effects of soil structure foundation interaction on the building response are not considered in this study. The properties of soil can have a significant impact on the response of the structure, in particular by (a) inertial interaction between soil and foundation during earthquake shaking that influences the overall flexibility and damping of the structure, and (b) kinematic interaction between soil and foundation during earthquake shaking that results in different foundation ground motions as compared to free field ground motions. This study

does not explicitly account for soil structure interaction effects, however for flexible moment frames, they should be negligible. These types of structures will correspond to all ductile moment frames and some of the taller non-ductile frames.

CHAPTER 6 REFERENCES

Abrahamson, N. A., and Silva, W. J. (1996). "Empirical ground motion models." *Report to Brookhaven National Laboratory*.

ACI. (2002). *Building code requirements for structural concrete (ACI 318-02)*. American Concrete Institute.

ACI. (2008). *Building code requirements for structural concrete (ACI 318-08)*. American Concrete Institute.

Amadio, C., Fragiacomo, M., and Rajgelj, S. (2003). "The effects of repeated earthquake ground motions on the non-linear response of SDOF systems." *Earthquake engineering & structural dynamics*, 32(2), 291–308.

ASCE. (2005). *Minimum Design Loads for Buildings and Other Structures (7-05)*.

ASCE. (2010). *Minimum Design Loads for Buildings and Other Structures (7-10)*.

ATC. (1989). *ATC-20 Procedures for Postearthquake Safety Evaluation of Buildings*.

ATC. (1995). *ATC-20-2, Addendum to the ATC-20 Postearthquake Building Safety Evaluation Procedures*.

Atkinson, G. M., and Boore, D. M. (2003). "Empirical ground-motion relations for subduction-zone earthquakes and their application to Cascadia and other regions." *Bulletin of the Seismological Society of America*, 93(4), 1703–1729.

Atkinson, G. M., and Macias, M. (2009). "Predicted ground motions for great interface earthquakes in the Cascadia subduction zone." *Bulletin of the Seismological Society of America*, 99(3), 1552–1578.

Baker, J. W. (2007). "Quantitative classification of near-fault ground motions using wavelet analysis." *Bulletin of the Seismological Society of America*, 97(5), 1486.

Baker, J. W., and Allin Cornell, C. (2005). "A vector-valued ground motion intensity measure consisting of spectral acceleration and epsilon." *Earthquake Engineering & Structural Dynamics*, 34(10), 1193–1217.

Baker, J. W., and Cornell, C. A. (2006). "Spectral shape, epsilon and record selection." *Earthquake engineering & structural dynamics*, 35(9), 1077–1095.

Baradaran Shoraka, M. (2013). "Collapse assessment of concrete buildings : an application to non-ductile reinforced concrete moment frames."

Baradaran Shoraka, M., and Elwood, K. J. (2013). "Mechanical Model for Non Ductile Reinforced Concrete Columns." *Journal of Earthquake Engineering*, 17(7), 937–957.

Beck, J. L., and Hall, J. F. (1986). "Factors contributing to the catastrophe in Mexico City during the earthquake of September 19, 1985." *Geophysical Research Letters*, 13(6), 593–596.

Bommer, J. J., and Martínez-Pereira, A. (1999). "The effective duration of earthquake strong motion." *Journal of Earthquake Engineering*, 3(2), 127–172.

Bommer, J. J., Stafford, P. J., and Alarcón, J. E. (2009). "Empirical equations for the prediction of the significant, bracketed, and uniform duration of earthquake ground motion." *Bulletin of the Seismological Society of America*, 99(6), 3217–3233.

Bommer, J., Magenes, G., Hancock, J., and Penazzo, P. (2004). "The Influence of Strong-Motion Duration on the Seismic Response of Masonry Structures." *Bulletin of Earthquake Engineering*, 2(1), 1–26.

Boore, D. M., and Bommer, J. J. (2005). "Processing of strong-motion accelerograms: needs, options and consequences." *Soil Dynamics and Earthquake Engineering*, 25(2), 93–115.

Bradley, B. A. (2011). “Correlation of Significant Duration with Amplitude and Cumulative Intensity Measures and Its Use in Ground Motion Selection.” *Journal of Earthquake Engineering*, 15(6), 809–832.

Bray, J. (2007). “Simplified seismic slope displacement procedures.” *Earthquake Geotechnical Engineering*, Geotechnical, Geological and Earthquake Engineering, 327–353.

Caltech. (2011). “Caltech Virtual Shaker.” <https://virtualshaker.caltech.edu/> (Oct. 6, 2011).

CESMD. (2012). “Center for Engineering Strong Motion Data.” <http://www.strongmotioncenter.org/> (Nov. 2, 2012). Selected strong motion records of the M8.8 Chile earthquake of Feb 27, 2010, being served by the Center for Engineering Strong Motion Data (CESMD) were provided by Professor Ruben Boroschek, Engr. Pedro Soto, and Mr. Ricardo Leon of Red de Cobertura Nacional de Acelerografos (RENADIC) of the Department of Civil Engineering, University of Chile. Also, some records were provided by the Department of Geophysics, University of Chile.

Champion, C., and Liel, A. (2012). “The effect of near-fault directivity on building seismic collapse risk.” *Earthquake Engineering & Structural Dynamics*, 1391–1409.

Chopra, A. K., and Goel, R. K. (2000). “Building Period Formulas for Estimating Seismic Displacements.” Earthquake Spectra, 16(2), 533–536.

Chock, G., Kindred, T., Robertson, I., Iinuma, G., Nicholson, P., Lau, E., Brandes, H., Sarwar, A., Medley, E., and Dal Pino, J. (2006). “Compilation of Observations of the October 15, 2006 KiholoBay (Mw 6. 7) and Mahukona (Mw 6.0) Earthquakes, Hawai ‘i.” *Earthquake Engineering Research Institute*.

COSMOS. (2011). “COSMOS Virtual Data Center.” <http://db.cosmos-eq.org/scripts/default.plx> (Oct. 6, 2011).

Don, L. (2007). “State of Oregon Open-File Report O-07-02 -Statewide seismic needs assessment: implementation of Oregon 2005 senate bill 2 relating to public safety, earthquakes, and seismic rehabilitation of public buildings” (Nov. 6, 2012).

EERI, W. M. D. E. M. D. (2005). *Scenario for a Magnitude 6.7 Earthquake on the Seattle Fault Earthquake Engineering Research Institute and the Washington Military Department Emergency Management Division June*. 162.

Elnashai, A., and Sarno, L. D. (2008). *Fundamentals of Earthquake Engineering*. Wiley.

Elwood, K. J. (2004). “Modelling failures in existing reinforced concrete columns.” *Canadian Journal of Civil Engineering*, 31(5), 846–859.

EQE International. (1994). “The January 17, 1994 Northridge, California earthquake: an EQE summary report.” EQE International.

FEMA. (2009). “Quantification of Building Seismic Performance Factors FEMA P695.”

Foschaar, J. C., Baker, J. W., and Deierlein, G. G. (2012). “Preliminary Assessment of Ground Motion Duration Effects on Structural Collapse.” *Proceedings of the 15th World Conference on Earthquake Engineering*.

Fox, J. (2008). *Applied regression analysis and generalized linear models*. SAGE.

Fragiacomo, M., Amadio, C., and Macorini, L. (2004). “Seismic response of steel frames under repeated earthquake ground motions.” *Engineering structures*, 26(13), 2021–2035.

Ghannoum, W. M., Moehle, J. P., and Bozorgnia, Y. (2008). “Analytical Collapse Study of Lightly Confined Reinforced Concrete Frames Subjected to Northridge Earthquake Ground Motions.” *Journal of Earthquake Engineering*, 12(7), 1105–1119.

Government of Canada. (2001). “Census of Canada.” <http://www12.statcan.gc.ca/census-recensement/index-eng.cfm> (Jun. 14, 2013).

Green, R. A., and Terri, G. A. (2005). "Number of equivalent cycles concept for liquefaction evaluations—revisited." *Journal of geotechnical and geoenvironmental engineering*, 131, 477.

Hancock, J., and Bommer, J. J. (2006). "A State-of-Knowledge Review of the Influence of Strong-Motion Duration on Structural Damage." *Earthquake Spectra*, 22(3), 827.

Haselton, C. B., Baker, J. W., Liel, A. B., and Deierlein, G. G. (2009). "Accounting for Ground Motion Spectral Shape Characteristics in Structural Collapse Assessment through an Adjustment for Epsilon." *Journal of Structural Engineering*, 137(3), 332–344.

Haselton, C. B., Liel, A. B., Deierlein, G. G., Dean, B. S., and Chou, J. H. (2011). "Seismic Collapse Safety of Reinforced Concrete Buildings. I: Assessment of Ductile Moment Frames." *Journal of Structural Engineering*, 137, 481.

Haselton, C. B., Liel, A. B., Lange, S. T., and Deierlein, G. G. (2008). *PEER Report 2007/03 Beam-Column Element Model Calibrated for Predicting Flexural Response Leading to Global Collapse of RC Frame Buildings*. 134.

Hatzigeorgiou, G. D. (2010). "Ductility demand spectra for multiple near-and far-fault earthquakes." *Soil Dynamics and Earthquake Engineering*, 30(4), 170–183.

Hatzigeorgiou, G. D., and Beskos, D. E. (2009). "Inelastic displacement ratios for SDOF structures subjected to repeated earthquakes." *Engineering Structures*, 31(11), 2744–2755.

Hatzigeorgiou, G. D., and Liolios, A. A. (2010). "Nonlinear behaviour of RC frames under repeated strong ground motions." *Soil Dynamics and Earthquake Engineering*, 30(10), 1010–1025.

Hayes, G., and Wald, D. (2011). "The 03/11/2011 Mw9.0 Tohoku, Japan Earthquake." Educational Slides, U.S. Geological Survey, National Earthquake Information Center.

Heaton, T. H., and Kanamori, H. (1984). "Seismic potential associated with subduction in the northwestern United States." *Bulletin of the Seismological Society of America*, 74(3), 933–941.

Ibarra, L. F., and Krawinkler, H. (2003). "Global collapse of frame structures under seismic excitations." PhD Dissertation, Department of CEE, Stanford University.

Ibarra, L. F., Medina, R. A., and Krawinkler, H. (2005). "Hysteretic models that incorporate strength and stiffness deterioration." *Earthquake engineering & structural dynamics*, 34(12), 1489–1511.

ICBO. (1967). *Uniform Building Code*.

ICBO. (1994). *Uniform Building Code*.

ICC. (2003). *International building code 2003*. International Code Council.

ICC. (2012). *International Building Code*. International Code Council.

Iervolino, I., Manfredi, G., and Cosenza, E. (2006). "Ground motion duration effects on nonlinear seismic response." *Earthquake engineering & structural dynamics*, 35(1), 21–38.

Katsanos, E. I., Sextos, A. G., and Manolis, G. D. (2010). "Selection of earthquake ground motion records: A state-of-the-art review from a structural engineering perspective." *Soil Dynamics and Earthquake Engineering*, 30(4), 157–169.

Kempton, J. J., and Stewart, J. P. (2006). "Prediction equations for significant duration of earthquake ground motions considering site and near-source effects." *Earthquake spectra*, 22, 985.

K-NET. (2012). “Kyoshin Network K-NET, Strong-Motion Seismigraph Network.” <http://www.k-net.bosai.go.jp/> (Jun. 17, 2012).

Kramer, S. L. (1996). *Geotechnical earthquake engineering*. Prentice Hall.

Krishnan, S., and Muto, M. (2008). “SHAKEOUT 2008: Tall Steel Moment Frame Building Response.” Report or Paper, , <http://resolver.caltech.edu/CaltechAUTHORS:20130305-134018243> (Nov. 25, 2013).

Lee, K., and Foutch, D. A. (2004). “Performance evaluation of damaged steel frame buildings subjected to seismic loads.” *Journal of Structural Engineering*, 130, 588.

Li, Q., and Ellingwood, B. R. (2007). “Performance evaluation and damage assessment of steel frame buildings under main shock–aftershock earthquake sequences.” *Earthquake engineering & structural dynamics*, 36(3), 405–427.

Liel, A. B., and Deierlein, G. G. (2012). “Using Collapse Risk Assessments to Inform Seismic Safety Policy for Older Concrete Buildings.” *Earthquake Spectra*, 28(4), 1495–1521.

Liel, A. B., Haselton, C. B., and Deierlein, G. G. (2011). “Seismic Collapse Safety of Reinforced Concrete Buildings. II: Comparative Assessment of Nonductile and Ductile Moment Frames.” *Journal of Structural Engineering*, 137, 492.

Luca, F. D., Chioccarelli, E., and Iervolino, I. (2011). *Preliminary study of the 2011 Japan earthquake ground motion record V1.01*.

Luco, N., Bazzurro, P., and Cornell, C. A. (2004). “Dynamic versus static computation of the residual capacity of a mainshock-damaged building to withstand an aftershock.” *Proceedings of the 13th World Conference on Earthquake Engineering*.

Luco, N., Ellingwood, B. R., Hamburger, R. O., Hooper, J. D., Kimball, J. K., and Kircher, C. A. (2007). “Risk-targeted versus current seismic design maps for the conterminous United States.” *Structural Engineers Association of California*, 163–175.

Mahin, S. A. (1980). “Effects of duration and aftershocks on inelastic design earthquakes.” *Proceedings of the Seventh World Conference on Earthquake Engineering, Istanbul*, 677–80.

Mahsuli, M., and Haukaas, T. (2013). “Seismic risk analysis with reliability methods, part II: Analysis.” *Structural Safety*, 42, 63–74.

Malhotra, P. K. (2003). “Strong-motion records for site-specific analysis.” *Earthquake Spectra*, 19, 557.

Matsumura, K. (1992). “On the intensity measure of strong motions related to structural failures.” *Proceedings of the 10th World Conference on Earthquake Engineering*, 375–380.

Mavroeidis, G. P., Zhang, B., Dong, G., Papageorgiou, A. S., Dutta, U., and Biswas, N. N. (2008). “Estimation of Strong Ground Motion from the Great 1964 Mw 9.2 Prince William Sound, Alaska, Earthquake.” *Bulletin of the Seismological Society of America*, 98(5), 2303–2324.

McDonald, B., Bozorgnia, Y., and John Osteraas, J. (2000). “Structural Damage Claims Attributed to Aftershocks.” *Forensic Engineering*, American Society of Civil Engineers, 123–131.

McGuire, R. K. (2004). *Seismic hazard and risk analysis*. Earthquake Engineering Research Institute, Oakland, Calif.

Moehle, J. (1998). “Existing Reinforced Concrete Building Construction.” *SEAONC Fall Seminar*.

Myers, R. H., Montgomery, D. C., Vining, G. G., and Robinson, T. J. (2010). *Generalized Linear Models: With Applications in Engineering and the Sciences*. John Wiley & Sons.

Nazari, N., van de Lindt, J., and Li, Y. (2013). "Effect of Mainshock-Aftershock Sequences on Woodframe Building Damage Fragilities (Accepted)." Journal of Performance of Constructed Facilities.

NIST. (2012). "Soil-structure interaction for building structures, Report No. NIST GCR 12-917-21, National Institute of Standards and Technology, U.S. Department of Commerce, Washington D.C."

NOAA. (2012). "Earthquake Strong Motion Database | National Geophysical Data Center." <http://www.ngdc.noaa.gov/hazard/strong.shtml> (Jun. 17, 2012).

OpenSees. (2012). "Open System for Earthquake Engineering Simulation - Home Page." <http://opensees.berkeley.edu/> (Oct. 6, 2011).

Pacific Northwest Seismic Network. (2012). "Cascadia Subduction Zone | Pacific Northwest Seismic Network." <http://www.pnsn.org/outreach/earthquakesources/csz> (Jun. 19, 2012).

PEER. (2012). "PEER NGA Database." <http://peer.berkeley.edu/nga/> (Oct. 6, 2011).

R. (2011). "The R Project for Statistical Computing." <http://www.r-project.org/> (Oct. 17, 2011).

Raghunandan, M., and Liel, A. B. (2013). "Effect of ground motion duration on earthquake-induced structural collapse." *Structural Safety*, 41, 119–133.

Raghunandan, M., Liel, A. B., Ryu, H., and Luco, N. (2012). "Aftershock Fragility Curves and Tagging Assessments for a Mainshock-Damaged Building." *15 WCEE, Lisbon*.

Ramirez, C. M., Liel, A. B., Mitrani-Reiser, J., Haselton, C. B., Spear, A. D., Steiner, J., Deierlein, G. G., and Miranda, E. (2012). "Expected earthquake damage and repair costs in reinforced concrete frame buildings." *Earthquake Engineering & Structural Dynamics*, 41(11), 1455–1475.

Reasenberg, P. A., and Jones, L. M. (1989). "Earthquake hazard after a mainshock in California." *Science*, 243(4895), 1173–1176.

Reasenberg, P. A., and Jones, L. M. (1994). "Earthquake Aftershocks: Update." *Science*, 265(5176), 1251–1252.

Ruiz-Garcia, J. (2010). "On the influence of strong-ground motion duration on residual displacement demands." *Earthquake and Structures*, 1(4), 327–344.

Ruiz-García, J., Moreno, J. Y., and Maldonado, I. A. (2008). "Evaluation of existing Mexican highway bridges under mainshock-aftershock seismic sequences." *The 14 th World Conference on Earthquake Engineering*.

Ruiz-García, J., and Negrete-Manriquez, J. C. (2011). "Evaluation of drift demands in existing steel frames under as-recorded far-field and near-fault mainshock–aftershock seismic sequences." *Engineering Structures*, 33(2), 621–634.

Ryu, H., Luco, N., Uma, S. R., and Liel, A. B. (2011). "Developing fragilities for mainshock-damaged structures through incremental dynamic analysis." *9PCEE Paper No*, 225.

SeismoSoft. (2012). "SeismoSoft - SeismoSignal." <http://www.seismosoft.com/en/SeismoSignal.aspx> (Nov. 4, 2012).

Sezen, H. (2002). "Seismic Behavior and Modeling of Reinforced Concrete Building Columns." Ph.D Dissertation, University of California, Berkeley, .

Sørensen, M. B., Atakan, K., and Pulido, N. (2007). "Simulated Strong Ground Motions for the Great M 9.3 Sumatra–Andaman Earthquake of 26 December 2004." *Bulletin of the Seismological Society of America*, 97(1A), S139–S151.

Sunasaka, Y., and Kiremidjian, A. S. (1993). *A method for structural safety evaluation under mainshock-aftershock earthquake sequences*. The John A. Blume Earthquake Engineering Center.

Thatcher, W. (2001). "Silent Slip on the Cascadia Subduction Interface." *Science*, 292(5521), 1495–1496.

Tothong, P., and Cornell, C. A. (2006). "An empirical ground-motion attenuation relation for inelastic spectral displacement." *Bulletin of the Seismological Society of America*, 96(6), 2146–2164.

Tothong, P., and Luco, N. (2007). "Probabilistic seismic demand analysis using advanced ground motion intensity measures." *Earthquake Engineering & Structural Dynamics*, 36(13), 1837–1860.

Tremblay, R. (1998). "Development of design spectra for long-duration ground motions from Cascadia subduction earthquakes." *Canadian Journal of Civil Engineering*, 25(6), 1078–1090.

Trifunac, M. D., and Brady, A. G. (1975). "A study on the duration of strong earthquake ground motion." *Bulletin of the Seismological Society of America*, 65(3), 581.

Uma, S. R., Ryu, H., Luco, N., Liel, A. B., and Raghunandan, M. (2011). "Comparison of main-shock and aftershock fragility curves developed for New Zealand and US buildings." Ninth Pacific Conference on Earthquake Engineering Building an Earthquake-Resilient Society.

US Census. (2012). "Census Bureau Homepage." <http://www.census.gov/#> (Nov. 7, 2012).

USGS. (2012a). "United States Geological Survey." <http://www.usgs.gov/> (Apr. 27, 2012).

USGS. (2012b). "United States Geological Survey - National Strong-Motion Project." <http://nsmp.wr.usgs.gov/> (Oct. 6, 2011).

Vamvatsikos, D., and Allin Cornell, C. (2006). "Direct estimation of the seismic demand and capacity of oscillators with multi-linear static pushovers through IDA." *Earthquake Engineering & Structural Dynamics*, 35(9), 1097–1117.

Vamvatsikos, D., and Cornell, C. A. (2002). "Incremental dynamic analysis." *Earthquake Engineering & Structural Dynamics*, 31(3), 491–514.

Weisberg, S. (2005). *Applied Linear Regression*. John Wiley & Sons.

White, T., and Ventura, C. E. (2004). "Ground motion sensitivity of a Vancouver-style high rise." *Canadian Journal of Civil Engineering*, 31(2), 292–307.

Yang, J. (2009). "Nonlinear Responses of High-Rise Buildings in Giant Subduction Earthquakes." Ph.D Thesis, California Instituteof Technology.

Youd, T. L., Arango, I., Castro, G., Christian, J. T., Dobry, R., Finn, W. D. L., Harder Jr, L. F., Hynes, M. E., Ishihara, K., Koester, J. P., and Foutch, D. A. (2001). "Liquefaction Resistance of Soils: Summary Report from the 1996 NCEER and 1998 NCEER/ NSF Workshops on Evaluation of Liquefaction Resistance of Soils." Journal of Geotechnical and Geoenvironmental Engineering, 127, 817.

Youngs, R. R., Chiou, S. J., Silva, W. J., and Humphrey, J. R. (1997). "Strong ground motion attenuation relationships for subduction zone earthquakes." *Seismological Research Letters*, 68(1), 58–73.

Zareian, F., and Krawinkler, H. (2007). “Assessment of probability of collapse and design for collapse safety.” *Earthquake Engineering & Structural Dynamics*, 36(13), 1901–1914.